MAGNETIC AND THERMAL PROPERTIES OF METALLIC ANTIFERROMAGNETIC MATERIALS

BY

KEXIN YANG

DISSERTATION

Submitted in partial fulfillment of the requirements
for the degree of Doctor of Philosophy in Physics
in the Graduate College of the
University of Illinois at Urbana-Champaign, 2020

Urbana, Illinois

Doctoral Committee:

Professor Nadya Mason, Chair
Professor David G. Cahill, Director of Research
Assistant Professor André Schleife
Associate Professor Virginia O. Lorenz

Abstract

Metallic antiferromagnetic materials are of great potential in spintronics due to their insensitivity to external fields and faster dynamics compared to typical ferromagnetic materials. Although they have these advantages, studies of their order parameter is difficult to perform because of the lack of net magnetization.

The linear magneto-optic Kerr effect (MOKE) is often used to probe magnetism of ferromagnetic materials, but MOKE cannot be applied to collinear antiferromagnets due to the cancellation of sublattice magnetization. Magneto-optic constants that are quadratic in magnetization, however, provide an approach for studying antiferromagnets on picosecond timescales.

I combined transient measurements of linear birefringence and optical reflectivity to study the optical response of Fe_2As to small ultrafast temperature excursions. We performed temperature-dependent pump-probe measurements on crystallographically isotropic (001) and anisotropic (010) faces of Fe_2As bulk crystals and found that the largest optical signals arise from changes in the index of refraction along the z-axis, perpendicular to the Néel vector. Both real and imaginary parts of the transient optical birefringence signal approximately follow the temperature dependence of the magnetic heat capacity, as expected if the changes in dielectric function are dominated by contributions of exchange interactions to the dielectric function.

In spintronic devices, it is essential to determine the dynamics of magnetic precession, the frequency of spin waves, the thermal stability of magnetic domains, and the efficiency. Thus magnetocrystalline anisotropy is a fundamental property of antiferromagnetic materials.

Torque magnetometry measurements of Fe_2As were performed. We reported that the four-fold magnetocrystalline anisotropy K_{22} in the (001)-plane of Fe_2As is $K_{22} = -150$ kJ/m^3 at T = 4 K, much smaller than the perpendicular magnetic anisotropy of ferromagnetic materials structure widely used in spintronics device. K_{22} is strongly temperature dependent and close to zero at T > 150 K. The anisotropy K_1 in the (010) plane is too large to be measured by torque magnetometry and we determine $K_1 = -830$ kJ/m^3 using first-principles density functional theory. Our simulations show that the contribution to the anisotropy from classical magnetic dipole-dipole interactions is comparable to the contribution from spin-orbit coupling. The calculated four-fold anisotropy in the (001) plane K_{22} ranges from -290 to 280 kJ/m^3, the same order of magnitude as the measured value. We used K_1 from theory to predict the frequency and polarization of the lowest frequency antiferromagnetic resonance mode and find that the mode is linearly polarized in the (001)-plane with frequency 670 GHz.

As we observed The field-dependent domain distribution and quadratic magnetization can potentially be measured with optical technique. We set up a static system for imaging in-plane magnetic domains. To test this system, I measured the quadratic MOKE coefficient of ferromagnetic cobalt and YIG thin films, and the field-dependent quadratic magneto-optical signal of $\mathrm{Fe_2As}$. The noise floor of the mapping system is determined to be $\sim 10^{-5}$.

Acknowledgments

I can still remember the midnight five years ago when I received the offer letter from Physics Department, University of Illinois at Urbana-Champaign. I was so excited that I stayed up until next morning. I really appreciate my five-year experience to work and live in University of Illinois. In past five years, I met so many excellent people and I got involved in a very meaningful research project.

I appreciate support and advice from my Ph.D. advisor, Prof. David Cahill. David is the most talent and diligent person I have ever worked with. As a professor with high reputation, he impressed me with his physical intuition and communication ability every time we have one-to-one meeting. The philosophy he does research and the kindness he gives to students make him the role model of almost every group member.

I acknowledge my MRSEC collaborators, Prof. Nadya Mason, Prof. André Schleife, Prof. Virginia Lorenz, Prof. Daniel Shoemaker, Kisung Kang, Manohar Karigerasi, Arun Ramanathan, Renee Harton, Joe Sklenar for their professional assists. Their are knowledgeable researchers in their research area and very reliable collaborators for me. I appreciate their contribution to my papers and my thesis work.

I specially thank our group alumni, Zhu Diao, Xu Xie for their hands-on guidance and patience. I cannot finish my Ph.D. thesis so smoothly without their help.

I also want to thank the members of Cahill group: Dongyao, Johannes, Judith, Qiye, Jungwoo, Sushant, Akash, Guangxin, Xiaoyang, Darshan, Max, Zhe, Tao, Junyi, Kisung, Wenrui, Kathleen, and Renee. Many thanks for their help in experiments and in my life. In addition, special thanks to Julio for his help in Laser Lab.

I want to thank my parents, my sister for their emotional and financial support from ten thousands miles away. I'd like to thank my husband, Qiye for his love and companion. I felt my luck was doubled as I worked with David and met my lover in David's group.

I want to thank my friends from Physics Department, Jialu, Tianhe, Yuhan, Xiaoyu. They are the most interesting and smartest people I have ever met. My Ph.D. life is less tough and less lonely with our friendship.

Table of Contents

Chapter 1

Introduction

1.1 Magnetic Materials and Spintronics

Conventionally, the term magnetic materials refers to "ferromagnetic materials" because of their observable net magnetization. Due to the earth's magnetic field, the magnetic needle was used for navigating for centuries. In ferromagnetic materials (FMs), spins are parallel to each other and coupled through positive exchange interaction. An external field can align spins of FMs to be parallel to external field, and when all spins are parallel to the field, we call the net magnetization "saturation magnetization". Due to the hysteresis of magnetization in a magnetic field, the magnetization of a FM can be nonzero without an external field.

The FMs are widely used in magnetic recording media and memory device. Besides opposite magnetic domains can be used to store binary information, spin valve structures are mainstream devices in spintronics. In spin valve structures, two FM layers are separated by a non-magnetic layer. The resistance of the spin valve is at low (high) state when two FM layers are parallel (antiparallel) to each other due to spin-dependent electron scattering [1, 2].

In an antiferromagnetic (AF) crystal, a magnetic unit cell can be divided into two or more atomic sublattices which order in such a way that their net magnetization is zero. Louis Néel first discussed this possibility in 1936 for two equal and oppositely aligned sublattices. The antiferromagnetic ordering transition, known as the Néel point, is marked by a small peak in the magnetic susceptibility, and a substantial specific heat anomaly, similar to that found at the Curie point of a ferromagnet.

For the AFs studied in this thesis, two equal but oppositely directed sublattices are coupled with negative exchange interaction. The long-range order parameters disappears above the Néel temperature T_N. AFs are considerably more common than FMs. They can be insulators, metals, semimetals or semiconductors, whereas FMs are primarily metals.

The potential of AFs is significant, as envisioned in the recent concept of AF spintronics where AF materials serve as active elements of spintronic devices. In particular, antiparallel spin sublattices in AFs, produce zero stray fields. Some AFs are insensitive to external field; for example, Mn_2Au [3] domains can be switched with external field more than 7 T. However, AF domains are sensitive to external field in some materials. The spin-flop field of CuMnAs is 2 T [4], moreover, we will show in a later chapter that the domains of Fe_2As start switching at approximately 0.5 T.

The speed of a processional switching of a spin is determined by the magnetic resonance frequency of the material. AFs have advantage that the spin dynamics are orders of magnitude faster than in FMs. The antiferromagnetic resonance (AFMR) frequency depends on anisotropy and the strength of exchange interactions, and usually ranges from hundreds of GHz to several THz; and the typical ferromagnetic (FMR) resonance frequency, on the other hand, depends on external field and demagnetization field, typically several GHz.

The domain structure of CuMnAs[5] and Mn_2Au [6] can be switched with electrical currents due to Néel spin-orbit torques (NSOT). Recently, electrical switching in Pt/AF insulator bilayers, e.g., Pt/Fe_2O_3 [7] and Pt/NiO [8] have been extensively studied. However, references [7] and [9] pointed out in electrical switching experiment, the reorientation process in AFs can be captured by with thermal activation or grain boundary migration.

1.2 Manipulation of Antiferromagnetic Order

Energetically degenerated states or magnetic domains of AFs can be used to store binary information. In spintronics, readability, writability and retention are three basic requirements for materials. In the writing procedure, the domains of AF should be manipulated and switched effectively, and those states should be easily distinguished in the reading procedure. Retention of data for long time periods requires that the magnetic state is thermally stable.

In experimental studies of AFs, AF states can be manipulated by field, light or electrical current. The change in domain structure can be observed optically and electrically.

1.2.1 Field Manipulation

When an external field is applied to a FM, the induced magnetization comes from the alignment of spins. When all spins of the material are aligned parallel to the field, the magnetization is called "saturation magnetization". FMs have spontaneous magnetization even at zero field due to the aligned magnetic domains.

The field-induced magnetization of AF comes from tilting of spins. When the external field is small, due to the small angle of tilting, the induced magnetization is linear in the external field, $M = \chi H$, where the coefficient χ is the susceptibility. The symbols $\chi_\perp$, $\chi_\parallel$ represent susceptibilities when spins are perpendicular

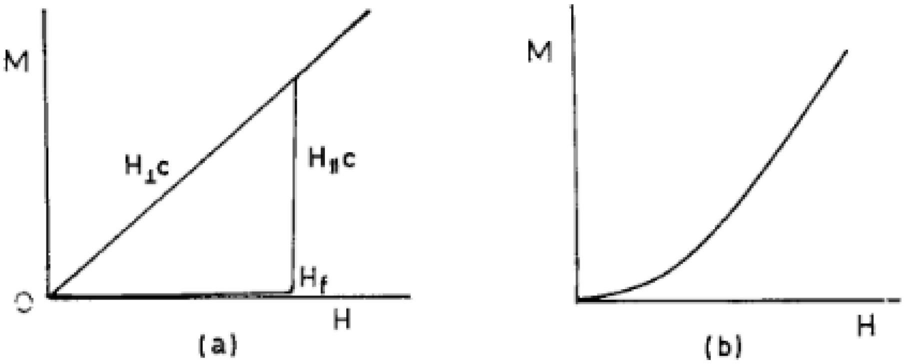

Figure 1.1: Magnetization versus field of (a) an uniaxial AF and (b) a cubic AF. The figure is from reference [10]

and parallel to the external field, respectively. In molecular field theory, $\chi_\perp > \chi_\parallel$ below the Néel temperature (the critical temperature where long-range order of AFs vanish above this temperature).

Although the induced magnetization in AFs is smaller than FMs, it does not mean AF orders are insensitive to magnetic fields. The magnetic energy of AF can be written as $E_m = -\frac{1}{2}\chi H^2$. The magnetic energy is lower when spins are perpendicular to the external field because $\chi_\perp > \chi_\parallel$.

In an antiferromagnetic crystal, the alignment of spins with external field applied depends on the interplay of field, magnetocrystalline anisotropy and exchange interaction. While the external fields prefer perpendicular spin alignment, magnetocrystalline anisotropy tends to keep spins along certain crystal axis, and exchange interaction prefers collinearity of spins.

When external fields applied along the easy axis of uniaxial AF, there are two types of metastable transitions depends on the magnitude of anisotropy of the material.

In small anisotropy system, the spin-flop transition happens when magnetic energy compensates the anisotropy energy. As shown in Fig. 1.1, the spin-flop transition is the transition where spins suddenly becomes perpendicular to the field [11, 12]. If the field is applied perpendicular to the spins, the magnetization builds up gradually; thus, there is no spin-flop transition. The different magnetization perpendicular and parallel to the easy-axis is shown in Fig. 1.1, where the slope of $M_\parallel$ dramatically changes at spin-flop field H_f while the slope of $M_\perp$ remains constant. Figure 1.1 shows that $\chi_\perp > \chi_\parallel$ at low field. By equating anisotropy energy and magnetic energy, the spin-flop field H_f is

$$H_f = \left(\frac{2K}{\mu_0(\chi_\perp - \chi_\parallel)}\right)^{\frac{1}{2}} \tag{1.1}$$

The anisotropy of the uniaxial AFs can be measured by characterzing the spin-flop field and susceptibility.

In large anisotropy system, the spin-flip transition occurs. Due to the large anisotropy, the magnetic energy compensates exchange energy first. As a result, the spins are transitioning from antiparallel to parallel along the crystal axis.

In an easy-plan AF magnetic structure, with the external field applied in the easy-plane, it can be treated as a small ansiotropy system because the anisotropy of the easy-plane is generally small. Instead of a spin-flop transition, gradual domain movement can happen as domain walls can displace at a field smaller than the spin-flop field.

The spin-flop transitions of MnF_2 [13] and $FeCl_2$ [14] were observed with the field applied along the easy-axis. Note that a (spin-flop) field of 9–10 T in MnF_2 is enough to rotate the magnetic moments by 90°. In easy-plane antiferromagnets, the magnetic domain can start to displace at field smaller than the spin flop field [15].

1.2.2 Optical Manipulation

Light manipulates magnetism of materials by transferring angular momentum and heat through the polarization and intensity of the light.

Circularly polarized light has +1 or -1 angular momentum depending on the polarity of the photon. The angular momentum of the photons can be treated as effective fields, and they can trigger the coherent magnetic resonance in both ferromagnetic or antiferromagnetic materials due to the inverse Faraday effect (IFE). The mechanism of circularly polarized light driven ferromagnetic resonance (FMR) was measured with Fe, Ni, Co and discussed in reference [16]. However, the thermal-induced effects are not fully discussed in [16]. The anisotropies of both Co and Fe are temperature-dependent and change rapidly at room temperature [17]. The ultrafast change in anisotropy as temperature increases perturbs the equilibrium state of magnetization and can trigger coherent spin oscillations [18].

Circularly polarized light induced antiferromagnetic resonance frequnecy was observed in the AF insulators NiO [19] and $DyFeO_3$ [20]. Here, the ultrafast circularly polarized light is equivalent to an instantaneous magnetic field. The 30 mJ cm^{-2} pump fluence with 200 fs pulse duration is equivalent to a 0.3 T effective field [20]. Compared to insulating AF, the stimulation and observation of AFMR in metallic AFs are more difficult to achieve, because of the optimal absorption and short penetration depth of metallic AFs.

As a heat source, light can trigger a series of thermally-related effects in magnetic materials, including demagnetization, coherent magnetic resonance, and spin Seebeck effect.

At 0 K, the spins of magnetic materials are perfectly ordered along certain direction. Spins start fluctuating incoherently at finite temperature. As a result, magnetization of ferromagnets macroscopically decreases with increasing temperature. The demagnetization can be studied in the time-domain with pump-probe measurement techniques.

The demagnetization process can be described with a three-temperature model, where the temperature of electrons, phonons and magnons are measures of the thermal energy in the each reservoir. After absorption of the femtosecond laser pulse, the electron system is excited and thermalized within 100 fs. The excess heat is then transferred to the phonons via electron-phonon coupling (g_{ep}), causing electron-phonon equilibration within $\approx$ 0.5 to 2 ps. In parallel, part of the excess energy in the electron and lattice subsystems flows into the spin subsystem through electron-spin coupling (g_{es}) and phonon-spin coupling (g_{ps}), causing spin excitations such as magnons, lowering the magnetization, and increasing the associated spin temperature. Finally the three temperatures converge once the system has achieved a new thermal equilibrium [21, 22]. In metallic materials, g_{ps} can often be neglected because it is small in comparison to g_{ep} and g_{es} [21]. In insulators, g_{ps} is large and the three-temperature model can be reduced to a two-temperature model [23].

In addition to the effect of demagnetization, the temperature increase of the lattice subsystem sometimes introduces ferromagnetic resonance because the magnetocrystalline anisotropy is also temperature-dependent. The sudden change of anisotropy drives spins out of balance along certain direction and can trigger coherent spin oscillations [18].

With heat-induced demagnetization or magnetic resonance, the angular momentum can transport inside the sample by a process called spin current or spin transfer torque. Spin transfer torque is widely used in non-volatile memory devices like magnetic random access memory (MRAM) because the spin transfer torque can be used to switch the state of spin valves.

Typically, the sample structure used to study spin transfer torque is composed of three layers: source layer, spacer and drain layer. In reference [24], the spin current is generated in a source layer of Co/Pt multilayer with perpendicular magnetic anisotropy through demagnetization. Spin is then transferred into the spacer. The spacer is usually a relatively thick metal film with with long spin diffusion length and used to suppress exchange interaction between the source and drain layers. Cu and Au are common spacers. The drain layer is used to detect the existence of spin current. In reference [24], CoFeB with in-plane magnetization is used, and the FMR of CoFeB layers proves the spin transfer torque reaches the CoFeB layer.

Inspired by this experiment, I attempted to excite magnon modes of antiferromagnetic materials (Fe_2As) with this three layer structure. I encountered several difficulties: a) the Fe_2As samples are bulk samples. Unlike thin film samples can be detected on both front and back side, once a thick spacer layer and source layer as deposited on the bulk sample, the probe light cannot penetrate through the spacer to see the AF layer. b) The transmission rate of spin current through the interface is very low, usually several percents. As our bulk Fe_2As surface is manually polished, the spin transmission rate can be even lower. (c) The AFMR modes are more complex than FMR modes in ferromagnetic materials as there are two sublattice magnetization. The zone center AFMR mode of easy plane antiferromagnets will be discussed in Chapter 4. (d) The AFMR frequency ranges from hundreds of GHz to THz. Without pulse compression, our pump-probe system does not have sufficient time resolution to measure terahertz oscillation. For materials such as Fe_2As or CuMnAs with Néel temperature close to room temperature, one can do the measurement near Néel temperature because AFMR frequency drops fast as temperature approaches Néel temperature. However, the sublattice magnetization and the amplitude of AFMR reduces with temperature as well.

A thermal gradient in insulating magnetic materials can drive the flow of electrons and magnons, the Seebeck effect and spin Seebeck effect, respectively. In ferromagnetic materials, a spin current can be generated from different Seebeck coefficients for spin-up and spin-down electrons. In paramagnetic materials [25] and antiferromagnetic materials [11], the spin Seebeck effect were observed with a strong magnetic field applied to create a net magnetization.

1.2.3 Electric current manipulation

When electrical current passes through a material, electrons with spins up and down will be separated by the spin-orbit interaction and start accumulating at sample boundary transverse to the electric current direction. We call this effect the spin Hall effect (SHE) and refer to the transverse polarized electrical current as spin current. Because the spin Hall effect arises from spin-orbit interactions, it can happen in a nonmagnetic material. The spin current due to the SHE can be written as

$$\mathbf{Q}_\sigma = \frac{\hbar}{2e}\theta_{SH}\mathbf{j_c} \times \sigma \tag{1.2}$$

where $\mathbf{Q}_\sigma$ is the spin current density, $\hbar$ is reduced Planck's constant, θ_{SH} is spin Hall angle, which represents the charge-to-spin-current conversion efficiency. $\mathbf{j}_c$ is electrical current density and σ is the spin polarization unit vector.

The inverse process of SHE, electric current generated in a material by the injection of spin current, is called the inverse spin Hall effect. The geometry of SHE and inverse SHE are illustrated in Fig. 1.2.

SHE and inverse SHE are prominent in materials with large θ_{SH}, e.g., Pt, β-Ta and β-W. In experimental studies of spin transfer, SHE provides a new way to generate spin current while inverse SHE makes it possible to observe spin current by measuring electric voltage of the sample. Both SHE [27] and inverse SHE [28] are

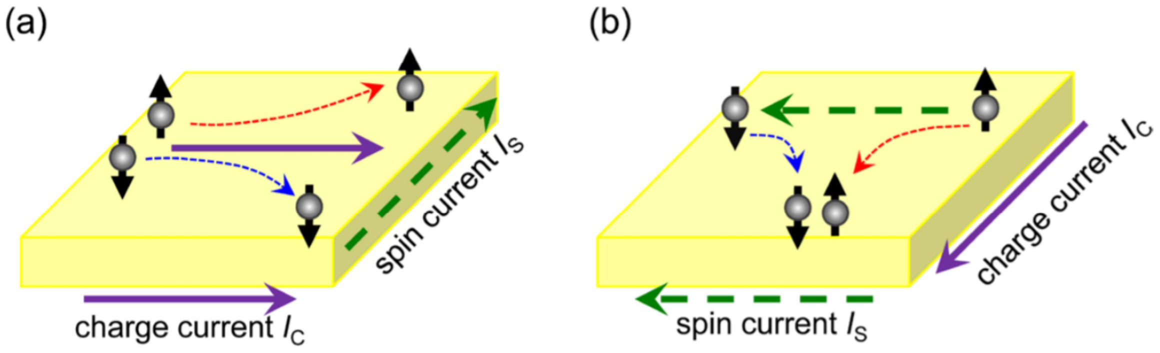

Figure 1.2: Schematic demonstration of (a) spin Hall effect and (b) inverse spin Hall effect. The figure is from reference[26].

observed in antiferromagnetic heavy metal-Mn alloys, like MnPt. These materials are ideal samples to study spin-orbitronics because they have both heavy elements (possessing large spin-orbit coupling) and magnetic atoms (possessing spin magnetic moment).

1.3 Observation of Antiferromagnetic Order

For antiferromagnetic materials with zero net magnetization, the detection of the order parameter is achieved by measuring effects that are second order in the sublattice magnetization. Optical techniques can measure the local order parameter of magnetic materials, while global magnetic properties can be measured electrically.

1.3.1 Anisotropic Magnetoresistance

Originating from the anisotropy of electronic structure induced by spin-orbit coupling, anisotropic magnetoresistance (AMR) is even in the magnetization. AMR refers to the fact that the resistance with electric current parallel $\rho_{||}$ and perpendicular $\rho_{||}$ to the magnetization is different.

Due to the difference between $\rho_{\perp}$ and $\rho_{||}$, AMR can be used to observe switching of magnetic domains, e.g., field induced switching in FePt [29] and electrical switching in CuMnAs [5]. The spin-flop transition of antiferromagnetic materials can also be observed with AMR. Field larger than the spin-flop field triggers dramatic domain movement and change in resistance [30].

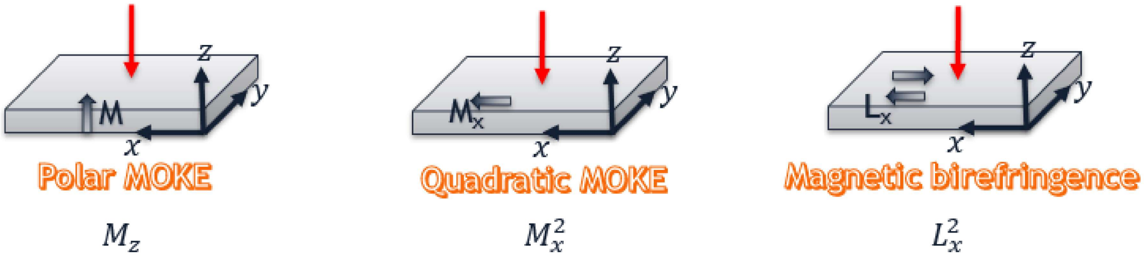

Figure 1.3: Three magneto-optic measurement geometries with perpendicular incident light: (a) polar magneto-optic Kerr effect (MOKE), (b) quadratic MOKE, (c) magnetic birefringence.

1.3.2 Optical Measurements

While AMR measures global properties, optical techniques can measure the local magnetism. The optical properties are determined by the dielectric constant. By expanding the dielectric constant as a function of the magnetization, the dielectric constant element ij can be written as

$$\varepsilon_{ij} = \varepsilon_{ij}^0 + K_{ijk}M_k + G_{ijkl}^{MM}M_kM_l + G_{ijkl}^{ML}M_kL_l + G_{ijkl}^{LL}L_kL_l + ... \tag{1.3}$$

where ε_{ij}^0 is the nonmagnetic term, M is net magentization and L is the Néel order of AFs, i.e., the difference of the two sublattice magnetizations $M_1 - M_2$. K and G are magneto-optic (MO) coefficients. According to Onsager's relation, linear (quadratic) terms appears in off-diagonal (diagonal) elements of the dielectric constant.

For in-plane and out-of-plane net magnetization, the magneto-optic Kerr effect (MOKE) with perpendicular incident light can be classified into polar MOKE and quadratic MOKE as shown in Fig. 1.3. For the measurement with AF, the in-plane Néel vector L_x will create differences between ε_{xx} and ε_{zz}, and the corresponding refractive index along x and z direction. In magnetic birefringence measurement, the difference of refractive index $\Delta n = n_x - n_y$ is measured. Therefore, Δn will show opposite signs for L_x and L_y.

Another name of quadratic MOKE and magnetic birefringence measurement is linear birefringence or linear dichroism. The word "linear" here refers to linear polarized light rather than linear magnetization; linearly polarized light is sensitive to in-plane magnetization. The MO signal depends on the angle between light polarization and the magnetization. Thus, the magnetic birefringence measurement can distinguish magnetic domains of an easy-plane AF.

Synchrotron X-rays and lasers are common light sources used to study MO effects. With pump-probe and microscopy techniques, the dynamics of magnetism and magnetic domains can be studied.

A widely used technique used to image AF magnetic domains is X-ray linear dichroism (XMLD), where the difference of absorption of horizontally and vertically polarized light at absorption edge of magnetic element is measured. Images of magnetic domains can be obtained with photoemission electron miscroscopy (PEEM). The imaging of antiferromagnetic domains revealed the order parameter change of antiferromagnetic materials with electrical current [31] and applied field [3]. A laser can be used as optical source to image an AF material [32]. But the imaging of AFs with laser is usually limited by the optical resolution and the small signals of generated by second order magnetization.

1.4 Outline of Thesis

In this thesis, I first introduce common techniques used in houseto characterize physical and magnetic properties of single crystal AF materials and then discuss several topics I did to explore thermal and magnetic properties of metallic AFs.

As the samples I studied mostly are single crystals, in chapter 2, I introduce how to use X-ray to determine crystal structures of a single crystal, especially how to find orientation of an unknown specimen. Once the crystal axes are known, I cut the polished the crystal along crystal orientations of interests. The basic magnetic properties about the materials, like the magnetic structure and Néel temperature, can be found in literature or database. I typically measure magnetic moment in a small field with Magnetic Properties Measurement System (MPMS) along easy and hard axis of the sample to confirm the magnetic structure, as the magnetic susceptibility is smaller along easy axis than along hard axis. Since the MPMS can go only up to 400 K, we can observe phase change if the T_N of sample is below 400 K. Rutherford backscatering spectroscopy (RBS) can be used to measure the stochiometry of materials. The thermal properties charaterization including heat capacity and thermal conductivity measurements techniques are introduced in this chapter.

In chapter 3, thermal birefringence of tetragonal crystal $\mathrm{Fe_2As}$ in response to ultrafast laser heating is studied with pump-probe system in the time domain. These measurements make use of the contribution of second order of magnetization to the refractive index. We do measurement along crystalline anisotropic (010) plane of easy-plane AF material $\mathrm{Fe_2As}$ across the Néel temperature ($T_N = 350$ K). The slower dynamics near the Néel temperature is due to the substantial heat capacity T_N that slows down the demagnetization process, as the thermal birefringence can be treated as spin temperature in a three-temperature model. Combined with thermoreflectance measurement with polarization along different direction, we showed that the largest MO response comes from changes in the dielectric constant along the z-axis. The microscopic origin of MO effect is dominated by exchange interaction, and independent of the orientation of Néel vector.

In chapter 4, I discuss torque magnetometry that can be used to study the magnetic symmetry and anisotropy of AFs. The interplay between magnetocrystalline anisotropy and magnetic energy causes non-collinearity of the induced moment of a magnetic single crystal and the external field. The torque $\tau = \mathbf{m} \times \mathbf{B}$ appears as a results of this non-collinearity. One can get magnetocrystalline anisotropy by analyzing torque data. The magnetic torque of Fe_2As is measured with the field rotating in both ac and ab-planes. The measurement results with the field rotating in the ac-plane is in the low field regime, and it can be fitted with a model of anisotropic susceptibility and field-dependent domain distribution. The measurement with the field rotating in the crystalline isotropic ab-plane is in the intermediate field regime where magnetic energy is comparable to anisotropy. The torque data can be modeled by minimizing the total energy, and the in-plane anisotropy can be derived.

In chapter 5, I describe the polarization modulating microscopy setup to do static magneto-optical effect measurements and AF domain imaging. The difficulties we encountered are described in detail, including the birefringence from optics, and fluctuations of the laser source. The quadratic magneto-optical effects of ferromagnets cobalt and YIG thin films with in-plane anisotropy are measured with external field rotating in the plane of the sample. We observed field dependent birefringence signal of Fe_2As. However, the mapping of Fe_2As domains was not completed because of small signal-to-noise ratio.

Chapter 2

Physical Properties Characterization of Antiferromagnetic Materials

In this chapter, the characterization of magnetic materials, including crystal structure, stochiometry, magnetic and thermal properties are discussed. Bulk AFs are used as example to explain the techniques, and most of these measurements can be extended to FM and AF thin films.

For single crystal samples and epitaxial thin films, measurements of crystal structure provide insight about possible magnetic structure of the materials. We use X-ray diffraction to characterise crystal structure. Moreover, the stochiometry and resisitivity measurements are helpful to understand the quality of the samples.

For magnetic properties characterization, we perform field-dependent and temperature dependent magnetic moment measurements with a Magnetic Properties Measurement System (MPMS). For FM materials, M vs H curve will show a hysteresis loop. For antiferromagnetic materials, the M vs H curve is almost linear. The linear coefficient is the susceptibility. M vs T measurements at small field are crucial to confirm the easy axis of AF crystals because the susceptibility along the hard axis is larger than the susceptibility along the easy axis.

Measurements of thermal properties, like thermal conductivity and heat capacity, are important to understand heat transfer inside a spintronics device. In addition, the specific heat is sensitive to phase transitions as it is derivative of the exchange energy with repect to temperature. Temperature-dependent specific heat can accurately indicate T_N.

2.1 Crystal Structure and Stochiometry Characterization

2.1.1 X-ray Diffraction

The crystal structure of antiferromagnetic single crystals can be determined with X-ray techiniques, X-ray diffraction (XRD) and Laue diffraction.

XRD measurements are based on Bragg's diffraction law where the constructive interference of reflected

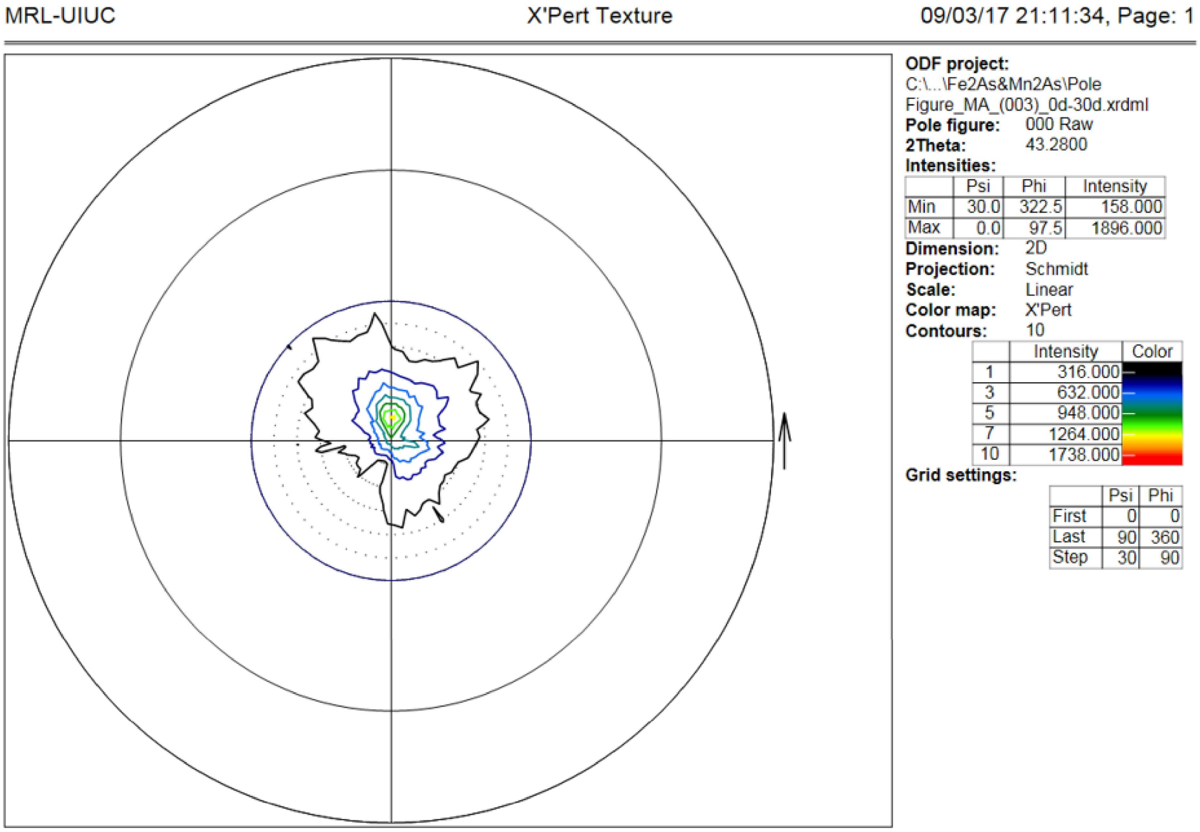

MRL-UIUC X'Pert Texture 09/03/17 21:11:34, Page: 1

ODF project:
C:\...\Fe2As&Mn2As\Pole Figure_MA_(003)_0d-30d.xrdml
Pole figure: 000 Raw
2Theta: 43.2800
Intensities:

	Psi	Phi	Intensity
Min	30.0	322.5	158.000
Max	0.0	97.5	1896.000

Dimension: 2D
Projection: Schmidt
Scale: Linear
Color map: X'Pert
Contours: 10

	Intensity	Color
1	316.000	⬛
3	632.000	🟦
5	948.000	🟩
7	1264.000	🟨
10	1738.000	🟥

Grid settings:

	Psi	Phi
First	0	0
Last	90	360
Step	30	90

Figure 2.1: The pole figure of Mn_2As with 2Θ and ω values are fixed at (003) plane. The ψ was scanned from 0° to 30°, and the ϕ was scanned from 0° to 360°.

x-rays occurs when diffraction angle 2Θ satisfies

$$\lambda = 2d_{hkl}\sin\theta \tag{2.1}$$

where λ is the wavelength of X-ray, d_{hkl} is the distance between atomic planes of (hkl) orientation. The 2Θ-ω scan is commonly used in XRD measurements to find the orientation of a crystal. In a 2Θ-ω scan, the 2Θ is scanning in some range and the diffracted beam intensity will show peaks once the Bragg's diffraction relation is satisfies. The ω is the incident angle which can be slightly adjusted for alignment. With the a 2Θ-ω diffraction pattern, the orientation of the crystal parallel to the sample stage can be determined.

For thin film samples, 2Θ-ω scan can be easily performed because the substrate are cleaved along certain crystal orientation and the substrate can easily be mounted parallel to the sample stage. For most of bulk crystals with unknown surfaces orientations, it is not easy to directly observe any peak in a 2Θ-ω scan. One way to measure the orientation is called a "Pole Figure".

Pole figures are used to study the texture of a sample. During the measurement, the sample is mounted on sample stage parallel to orientation B, 2Θ and ω values are fixed with orientation A, and a scan is carried out by varying the sample stage angles ϕ and ψ. The diffraction intensity will show a peak if the orientation A is detected at ϕ_A and ψ_A. The orientation B is at $\phi = 0$ and $\psi = 0$. Once the diffraction intensity is plotted in a polar figure with ψ as radius and ϕ as angle, the surface we targeted A is at the point where the intensity is at a maximum, and the surface we mounted on B is at the origin. Based on the angle difference between ϕ_A and 0° and ψ_A and 0°, the orientation B can be derived.

Figure 2.1 shows the pole figure measurement performed with a Mn_2As sample. The sample was mounted on a glass slide, and 2Θ and ω values are fixed to the value of (003)-plane (orientation A) of Mn_2As. In Fig. 2.1, every minor scale plotted as a dotted line is an increment of 5° in ψ, and each circle is a ϕ-scan at a given ψ value. In this measurement, ϕ is varied from 0° to 360°, and ψ is varied from 0° to 30°. The intensity is shown as contours and the peak intensity is the (003) face. The origin (orientation B), where both ψ and ϕ are zero, is the same surface as I mounted on glass slide, is about 5° away from the (003) face.

2.1.2 Rutherford Backscattering Spectrometry

Rutherford backscattering spectrometry (RBS) is an ion scattering technique used in material science to determine the composition and thickness (thin films) of a sample. ^{4}He particles are accelerated and backscattered by the sample with incident angle α, exit angle β and scattering angle θ. The energy distribution and yield of the backscattered particles are measured.

The RBS spectrum of Fe_2As is shown in Fig. 2.2. The measurement was performed with $\alpha = 22.5°$, $\beta = 52.5°$ and $\theta = 150°$. By defining a model and experimental setup in SIMNRA software, we can then adjust parameters in the model and obtain a fit between the model and data. The model consists of Fe and As, with an atomic ratio around 2:1, and to be adjusted to minimize the χ^2 value. The only adjustable parameter in the experimental setup is particles *sr. This quantity is related to the beam current, data acquisition time, and solid angle at the detector. All other parameters are calibrated by fitting data collected from a Pt/Mn/Si sample.

In experimental data from Fe_2As as shown in Fig. 2.2, the two steps between 600 to 700 channels are from Fe and As elements, respectively. When the data are plotted on a log-scale, the small signal above 700 channels is from pile-up. The pile-up signal comes from pulses overlapping. It can be simulated with SIMNRA software. With the SIMNRA software, I set the the pulse rise time as 1 μs, and the green solid line in Fig. 2.2 depicts the contribution of the pile-up to the data collection. The addition of pile-up to the model minimizes its effect on the stochiometry fitting.

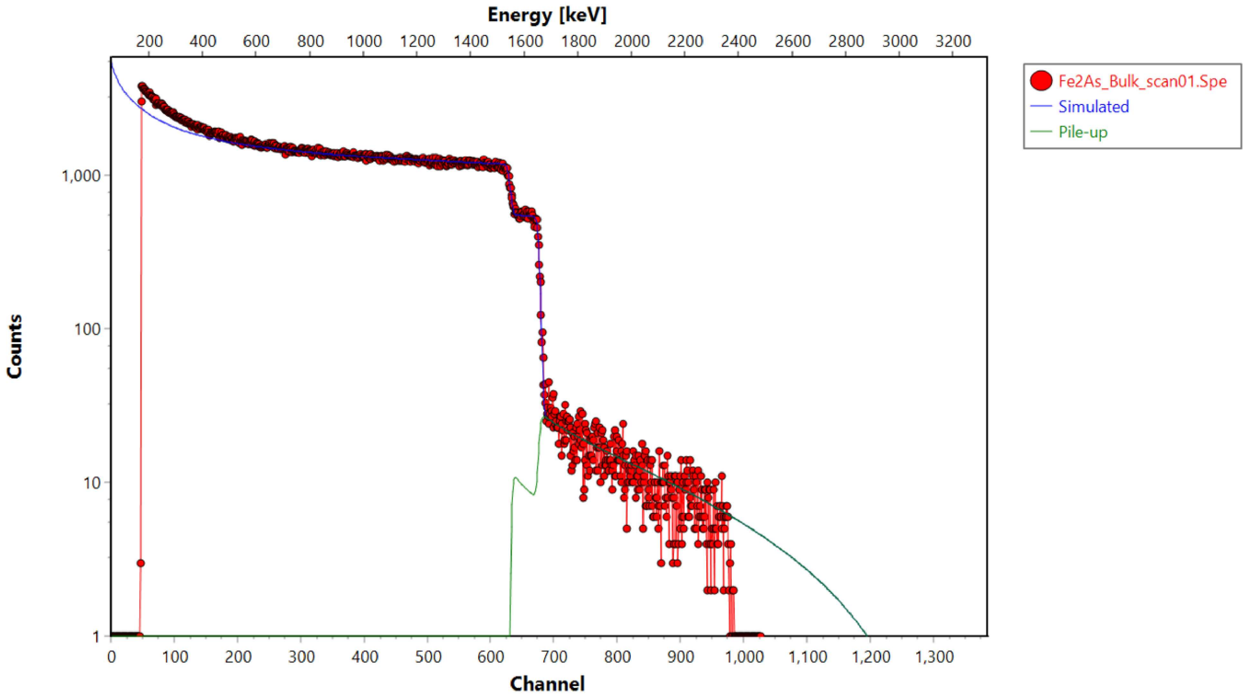

Figure 2.2: The RBS measurement of bulk Fe_2As and the model fit results

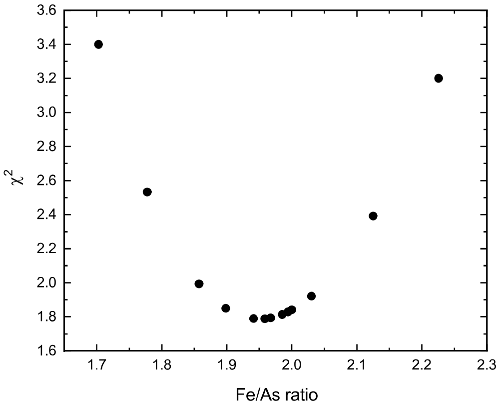

Figure 2.3: The χ^2 value when fitting Fe-to-As ratio to RBS data

During the stochiometry fitting, I adjusted the Fe-to-As atomic ratio to minimize the χ^2, which is the quadratic deviation of the simulated data from the experimental data. The Fe-to-As ratio is 1.96 when χ^2 is minimized as shown in Fig. 2.3. The error is determined by varying Fe/As ratio until χ^2 changes by 1. The fitting gives Fe/As ratio as 1.96±0.26.

2.2 Magnetic and Physical Properties Characterization

2.2.1 Magnetic Moment and Magnetic Susceptibility

The magnetic moment with changing magnetic field and temperature of the magnetic sample can be measured with a Quantum Design Magnetic Properties Measurement System (MPMS). The MPMS system contains a Superconducting Quantum Interference Device (SQUID) magnetometer. The external field is applied by a superconducting magnet and the signal is picked up by detection coils as shown in Fig. 2.5a. There are two modes one can use to measure the magnetic moment, one is Vibrating Sample Magnetometry (VSM) and the other is DC mode.

Before the measurement, the sample is centered between the detector coils with a scan of the sample position. The scanned data is the same as shown in Fig. 2.5a. In VSM mode, the sample is oscillating between the pick-up coils. The movement of the sample disturbs the local magnetic field and induces electrical current in detection coils. The magnetic moment is measured by picking up induced current at the same frequency as oscillation with a lock-in.

In DC mode, the sample is slowly moving up and down inside the chamber. The raw data curves are like signal versus sample position curve shown in Fig. 2.5a, and the fitting of the raw data can derive magnetic moment. So the DC mode measurement is more accurate than VSM if the sample is not centered well or the center position changes during measurement. However, DC mode measurements are slower than VSM. For temperature dependent magnetic moment measurement, a DC measurement can take a few hours longer than a VSM measurement.

For ferromagnetic materials, field-dependent magnetization measurement (hysteresis loop) is important to determine magnetic anisotropy, coercivity and saturation magnetization.

For AF materials, in most cases, the M vs H curves are straight lines when the external field is smaller than the spin-flop field. The linear coefficient, magnetic susceptibility, is an important quantity for studying AF materials because it can tell us how easy it is for an external field to modify the magnetization. From the magnitude of the susceptibility along different crystallographic directions, we can tell the easy axis of AF materials.

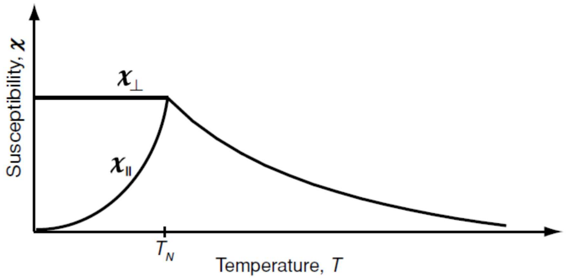

Figure 2.4: The susceptibility of the antiferromagnetic materials calculated from molecular field theory with external field parallel and perpendicular to spin aixs.

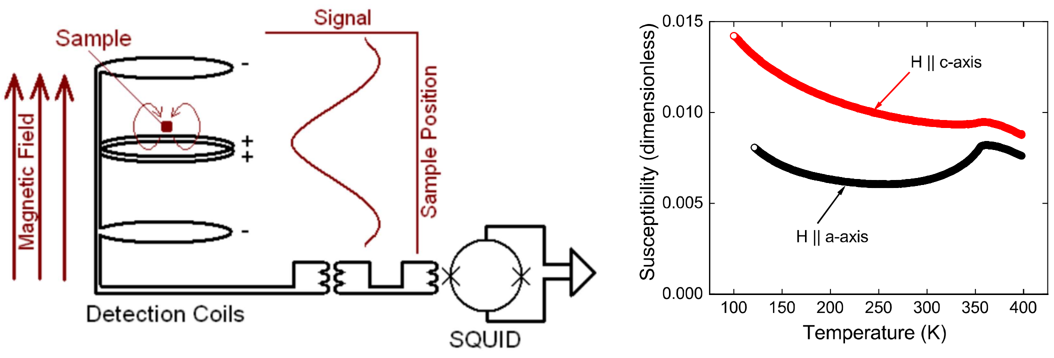

(a)

(b)

Figure 2.5: (a) SQUID detection schematic (b) Temperature-dependent susceptibility of Fe_2As measured with 100 Oe external field along a-and c-axis.

A typical temperature dependent susceptibility in a small field is shown in Fig. 2.4. Below the Néel temperature, $\chi_\perp$ is constant, and $\chi_{||}$ goes approach zero. In molecular field theory, $\chi_\perp$ is inversely proportional to nearest neighbor exchange coupling in small field limit. In other words, the antiferromagnetic materials with smaller $\chi_\perp$ has stronger exchange coupling.

For antiferromagnetic sample Fe_2As, we performed temperature-dependent magnetic moment measurement with external field at 100 Oe along *a*-and *c*-axis, where *a*-axis is one of easy axis in the easy plane, and *c*-axis is hard axis. We choose 100 Oe rather than 10 kOe because 100 Oe field does not induce domain wall motion. More details will be provided in Chapter 4. The suscepitbility in Fig. 2.5b is the ratio of magnetization and external field $\chi = M/H$ in SI units.

2.2.2 Thermal Conductivity

The thermal conductivity measurement is conducted with time-domian thermoreflectance (TDTR) setup. In this setup, a mode-locked Ti:sapphire laser produces a train of pulses (wavelength centered at 785 nm, repetition rate is 80 MHz) that is separated into a pump beam and a probe beam. An electro-optic modulator (EOM) modulates the pump beam with a frequency of 10.7 MHz before the beam passes through a delay stage to change the optical path relative to that of the probe beam. Without modulating probe beam, we can collect in-phase (V_{in}) and out-of-phase (V_{out}) signals of the reflected probe beam recorded by an radio frequency (RF) lock-in amplifier with the reference frequency set at around 10 MHz.

To remove background signals created by coherent rf pickup, we use double modulation or heterodyne detection. With double modulation approach, we modulate the pump-beam at radio frequency range because we can reject low-frequency noise and the measurement sensitivity is typically maximized a 1/8 of the laser repetition rate. The probe beam is modulated at AF frequency range. In our system, the probe beam is chopped by a mechanical chopper, and the signal will be demodulated by a RF lock-in at 10 MHz and an AF lock-in at 200 Hz sequentially.

The pump beam heats up the sample, and the probe beam functions as a thermometer by detecting the changes in sample reflectivity due to the temperature rise. An objective lens focuses both the pump and probe beam on the sample surface. The beam size as measured by the $1/e^2$ intensity radius depends on the objective lens, and typically ranges from 2 um to 10 um.

Prior to the measurement, an approximately 80 nm thick Al optical transducer film is deposited via magnetron sputtering onto the sample. Because the measurement depends on the linear relation of dR and dT, a small temperature excursion is needed to ensure the linearity of the measurement.

To extract thermal conductivity from the TDTR data, we use a heat diffusion model to fit the ratio of V_{in} and V_{out} curves [33]. When we do the fitting of the ratio signal, the absolute value of ΔT is not important because the dR/dT term is cancelled out. So the measurement does not require characterization of dR/dT. To calculate the absolute value of ΔT, we need to know the value of dR/dT. The way to calculate dR/dT will be explained in Chapter 3.

The thermal conductivity of Fe_2As was measured normal to the (001) and (010) faces of the crystal using conventional TDTR measurements and modeling [34] as shown in Fig. 3.5b. An 80 nm thick Al film was sputtered on the sample to serve as the optical transducer in the thermal conductivity measurement. The electrical contribution to the thermal conductivity was estimated using the combination of the Wiedemann-Franz law and the measured electrical resistivity. The thermal conductivity shows a small anisotropy at $T > 300$ K (see Fig. 3.5b). Contributions to the thermal conductivity from phonons and electronic excitations are comparable. The phonon contribution, i.e. the difference between the measurement and the electronic contribution, is approximately 3.6 $\mathrm{W\,K^{-1}\,m^{-1}}$ and independent of temperature.

2.2.3 Specific Heat

The measurement of the heat capacity of solids can provide considerable information about the lattice, electronic, and magnetic properties of materials. The specific heat of bulk materials can be measured with the heat capacity option of the Physical Properties Measurement System (PPMS).

The puck (or sample stage) of the caloritometer in the PPMS is comprised of three important parts: a resistive platform heater, a platform thermometer and a puck thermometer. During each measurement, the heater applies a heat pulse to the sample, then the platform thermometer measures the platform temperature T_p, the puck thermometer measures the ambient temperature T_b. To analyze the raw measurement, a simple model [35] can be used with the assumption that the sample and sample platform are in good thermal contact with each other and are at the same temperature during the measurement. In the simple model, the temperature T_p of the platform as a function of time t obeys the equation

$$C_{\text{total}}\frac{dT_p}{dt} = P(t) - K_w(T_p - T_b) \tag{2.2}$$

where C_{total} is the total heat capacity of the sample and platform, K_w is the thermal conductance of the supporting wires that connect the thermal bath and the platform.

If the thermal contact between the sample and sample platform is poor ($T_s \neq T_p$), a model called two-tau model [35] describes heat flow between the platform and sample, and platform and puck can be used to fit the data.

$$\begin{aligned} C_{\text{platform}}\frac{dT_p}{dt} &= P(t) - K_w(T_p(t) - T_b) + K_g(T_s(t) - T_p(t)) \\ C_{\text{sample}}\frac{dT_s}{dt} &= -K_g(T_s(t) - T_p(t)) \end{aligned} \tag{2.3}$$

where C_{platform} and C_{sample} are heat capacities of platform and sample, K_g is the thermal conductance between the two due to the grease that is used to attach the sample.

As the magnetic specific heat c_m is related to disorder of atomic moments, c_m is an indirect probe of exchange interactions. The magnetic specific heat can be derived by subtracting the phonon and electron heat capacity from the total heat capacity, $C_m = C_{tot} - C_{ph} - C_e$. We measured the total heat capacity of a 35.5 mg sample of Fe_2As with a Quantum Design Physical Property Measurement System (PPMS), see Fig. 3.5a in the next chapter. The ways to separate C_{ph} and C_e from C_{tot} will also be discussed in next chapter.

2.2.4 Electrical Resistivity Measurement

The electrical resistivity is one of the physical properties that can help determine the chemical purity and mechanical state of materials. Resistivity measurements provide detailed information on the electronic structure and other aspects of the fundamental physics of metals. Because electrons are the major carriers of heat in metals, the thermal conductivity of a metal can be estimated from the electrical conductivity using the Wiedemann-Franz law:

$$\kappa = \sigma L T \tag{2.4}$$

where κ is thermal conductivity, σ is electrical conductivity, L is the Lorenz number, T is temperature.

We performed resistance measurement with PPMS, and the determined shape factor of the sample with Van der Pauw method at room temperature. Silver wires were bonded to four corners of a $\mathrm{Fe_2As}$ thin plate (4mm * 7 mm * 0.65 mm) and connected to a resistivity puck of the PPMS. Because the resistance is affected by the shape of the sample, we determined the shape factor with a home-built user bridge. We measured the resistance R_{1234}, R_{3412}, R_{2413} and R_{1324} (1,2,3,4 are four points clockwisely bonded to the sample surface), and the shape factor was calculated based on reference [36]. Similar to PPMS, the resistance was measured by applying an ac current and collecting voltage at the same frequency. The Van der Pauw measurement was done with 47 Hz frequency and 9.8 mA current applied by a lock-in amplifier to the sample at room temperature. Then the puck was placed into the PPMS chamber and the performed the resistance measurement from 7 K to 400 K. Because the shape factor does not change with temperature, we scale the measured resistance to the resistivity value at room temperature.

The electrical resistivity of a polycrystalline sample of $\mathrm{Fe_2As}$ was reported previously as $\rho \approx 220\ \mu\Omega\,\mathrm{cm}$ at $T = 300$ K [37]. The electrical resistivity has a shallow maximum near room temperature and decreases to $\approx 125\ \mu\Omega\,\mathrm{cm}$ at $T = 1$ K. The electrical resistivity of our samples near room temperature is $\rho = 240\ \mu\Omega\,\mathrm{cm}$; the residual resistivity ratio (RRR), the resistivity at 300 K divided by the resistivity at 7 K, is 1.7, about one order of magnitude smaller than most metals.

We attribute the small RRR to Fe vacancies. The stoichiometry of $\mathrm{Fe_2As}$ was evaluated using Rutherford backscattering spectrometry and Rietveld refinements to synchrotron X-ray and neutron diffraction data. These measurements converge on a Fe deficiency of 0.05 to 0.08 out of 2. This value also agrees with the nominal Fe:As ratio used during synthesis (1.95:1). (Nominally 2.00:1 samples exhibit metallic Fe impurities.)

Chapter 3

Thermal Birefringence Measurement

3.1 Introduction

Antiferromagnetic materials are under intense investigation as a new generation of spintronic materials because of their robustness to external magnetic fields and ultrafast dynamics, as it manifests itself, for instance, in a higher resonance frequency, compared to ferromagnets [38, 39, 40, 41, 42]. Characterization of the structure and dynamics of the magnetic order parameter is essential for spintronics research but is difficult to achieve in antiferromagnets (AFs). Magneto-optical effects are often a valuable tool for probing magnetic order; for example, much of what is known about the dynamics of ferromagnetic and ferrimagnetic materials comes from studies that make use of the linear magneto-optical Kerr effect (MOKE) [21, 43]. Linear MOKE is also an essential tool for imaging the structure of magnetic domains [21, 44]. For typical AFs, however, linear MOKE is absent. Application of linear MOKE in the study of AFs is mostly limited to AFs with weak ferromagnetism due to canted magnetic moments, e.g., in orthoferrites [45]. More recently, relatively large linear magneto-optic effects were observed in the *non-collinear* AF Mn_3Sn[46, 47].

The structure and dynamics of the order parameter of AFs is typically probed using interactions that are quadratic in the magnetization. For example, anisotropic magnetoresistance (AMR) depends on contributions to electronic relaxation times that are quadratic in magnetization; AMR is sensitive to the domain structure of antiferromagnetic materials[48]. More recently, AMR was used to read the spin configuration of antiferromagnetic CuMnAs[49] and Mn_2Au[6]. At x-ray wavelengths, magnetic linear dichroism (XMLD) probes the anisotropy of charge distributions that are quadratic in the magnetization [50].

Magnetic birefringence refers to anisotropies in the optical frequency dielectric function that are generated by terms that are second order in the magnetization. Since the dielectric function and the second order terms of magnetization are both second rank tensors, the quadratic magneto-optic coefficients are a fourth rank tensor. Magnetic birefringence has been widely used in studies in optically transparent AFs [51] and ferromagnetic garnets.

In 2017, Saidl *et al.*[5] reported their studies of the time-resolved magneto-optic response of AF CuMnAs to a large temperature excursion, $\Delta T \sim$100 K. CuMnAs films were grown epitaxially on GaP(001) substrates with the z-axis, which is the hard magnetic axis of CuMnAs, parallel to the surface normal. The magnetic structure of tetragonal CuMnAs has two degenerate magnetic domains with perpendicular Néel vectors in the x-y plane. For a 10 nm thick CuMnAs layer, the authors observed a rotation of the polarization of the optical probe beam that is consistent with an optical response that is quadratic in magnetization, $\Delta\theta \propto \sin 2\alpha$, where α is the angle between the Néel vector and the light polarization.

In our work, we studied transient changes in the optical frequency dielectric function of the metallic AF Fe_2As, produced by a small temperature excursion, $\Delta T \sim$3 K. We acquire data for changes in birefringence and reflectivity using techniques that we refer to as time-domain thermo-birefringence (TDTB) and time-domain thermo-reflectance (TDTR). TDTB and TDTR signals are acquired using a pump-probe apparatus based on a high repetition rate Ti:sapphire laser oscillator operating at a wavelength near 785 nm.

Fe_2As crystallizes in the Cu_2Sb tetragonal crystal structure with spins stay along x- and y-axis as shown in Fig. 3.3a [52]. Based on the corresponding magnetic symmetry (mmm1' magnetic point group), the Néel vector of Fe_2As has two degenerate orientations in the $\langle 100 \rangle$ and $\langle 010 \rangle$ directions. Hence, on length scales large compared to the domain size, the dielectric function in the x-y plane is isotropic. We indeed do not observe a significant TDTB signal for the (001) surface of Fe_2As; however, on the crystallographically anisotropic (010) surface of the tetragonal crystal, we observed a strong TDTB signal for light polarized at an angle of 45° between the x and z axis of the crystal. We gain complementary insight by measuring the TDTR signals for light polarized along the x and z axes.

Typically, the dominant contribution to the magnetic birefringence of ferromagnetic materials is the Voigt effect, where only the components of the dielectric tensor *parallel* to the magnetization are affected [53, 54]. However, as we discuss below, our data implies $\Delta\varepsilon_\perp \gg \Delta\varepsilon_\parallel$ and the dependence of the TDTB signal on the sample temperature closely resembles the temperature dependence of the magnetic heat capacity, supporting a direct connection between exchange energy and dielectric function. Hence, if we assume that magnetization is the only contribution for a temperature dependence of the dielectric function, we conclude that, in Fe_2As, the quadratic magnetization term contributes most strongly to the dielectric function *perpendicular* to the Néel vector, implying that the Voigt effect is not the major contribution to the TDTB signal of Fe_2As.

Our experiments also provide insight into the ultrafast magnetization dynamics of Fe_2As. Furthermore, by comparing changes in the magneto-optical response at short and long time-scales, we evaluate the importance of magnetostriction to magnetic birefringence in this material.

3.2 Experimental Details

3.2.1 Synthesis of Fe_2As, Sample Preparation

Single crystals of Fe_2As were synthesized from the melt. Stoichiometric amounts of elemental Fe and As (99.8% and 99.999%, Alfa Aesar) were ground inside an argon filled glove box in an agate mortar and pestle. The powder mixture was loaded in a 6 mm-diameter fused silica tube and sealed under vacuum. The tube was heated to 700 °C and held for 24 h, then 1000 °C for 2 h, with 5 °C/min ramp rate. The tube was cooled to 900 °C in 20 h, then cooled at 5 °C/min to obtain shiny gray crystals of Fe_2As. The phase purity of the sample was confirmed using powder X-ray diffraction on a Bruker D8 diffractometer with Mo $K\alpha$ source and LYNXEYE XE detector in the transmission geometry. Rietveld refinements were performed using TOPAS 5. The lattice constants at room temperature are $a = 3.63$ Å, $c = 5.98$ Å.

Before optical measurements, the chunk Fe_2As sample was polished along the (001) and (010) orientation with an Allied Multiprep automatic polisher with diamond lapping films down to 0.3 μm. The orientation was observed via X-ray diffraction pole figures. The miscut of the surfaces is within 10°. After polishing, the sample was ion milled for 5 min by an ion miller with Ar source of 250 V beam voltage and 60 mA beam current.

3.2.2 Experimental Setup for Measuring Time-domain Thermoreflectance and Thermal Birefringence

The optical measurement of TDTB and TDTR was shown in Fig. 3.1. The measurements were performed with a pump-probe system that employs a Ti:sapphire laser with a 80 MHz repetition rate and 783 nm center wavelength. The spectral linewidth is 10 nm. The pump beam is modulated at 10.8 MHz with electro-optic modulator (EOM) while the probe beam is modulated at 200 Hz with a mechanical chopper. During time-resolved measurements, the length of the optical path of pump beam is changed by the delay stage, which introduces a time delay between the arriving time of pump pulse and the corresponding probe pulse at the sample surface. This time window is limited by the length of the delay stage and is about 4 ns in our current setup.

A half-wave plate was placed on the probe beam path to rotate the polarization of probe beam. The polarizing beam splitter used in front of objective lens in normal TDTR measurement to separate pump and probe beam was replaced with a non-polarizing beam splitter. For TDTB experiment, the changes of the light polarization and ellipticity were captured by a balanced photodetector, while in TDTR experiment, the transient reflection was measured by a Si photodetector. Both TDTB and TDTR signals were double

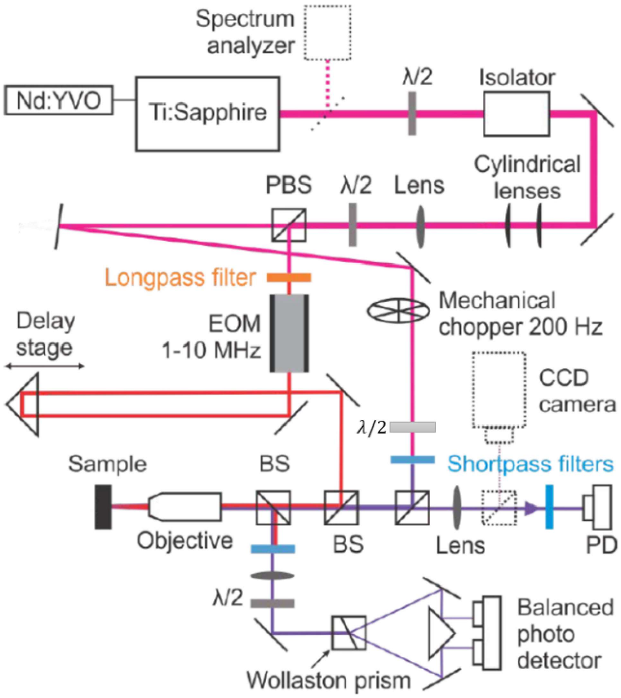

Figure 3.1: The optical setup for TDTB and TDTR measurements. The TDTB is measured with balanced photo detector and TDTR is measured with photodetector.

modulated to reduce the background created by diffusively scattered pump and coherent pickup of electronics. The in-phase and out-of-phase signal from the physical lock-in amplifier are next processed by a computer lock-in amplifier with the reference frequency same as the chopper frequency.

In our setup the pump and probe pulses are at normal incidence and their paths are overlapped with each other. This is very convenient for the setup and alignment. But in this geometry the pump pulse can be leaked into the photodiode. This part of pump pulse is the noise that cannot be removed by the lock-in amplifier. There are three designs in the system to remove the reflected pump pulse from final signal. The first one is using polarizing beam splitter. Because the polarization of pump and probe beams are perpendicular, the polarizing beam-splitter blocks majority of reflected pump beam. The second one is two-tint feature of pump-probe system[55]. It means that pump and probe pulses are spectrally separated with two edge filter on pump and probe beam paths. An ultrasharp edge filter to remove part of the reflected pump beam. The third one is double modulation [56].

In these experiments, the $1/e$ laser spot size of both pump and probe is 5.5 μm, and the laser fluence of pump is 0.22 J/m^2, which created a steady-state heating of 13 K on the sample surface. The steady state heating is calculated with TDTR model, and the laser fluence is calculated with equation:

$$\frac{2A_{pump}(1-R)T_{obj}\tau_{rep}}{\pi r^2} \tag{3.1}$$

where A_{pump} is power of pump beam, R is reflectance of sample, T_{obj} is transmission of objective lens, τ_{rep} is repetition rate of laser, r is radius of focused beam spot.

3.2.3 Temporal Resolution and Zero Time Delay

For analysis of ultrafast phonemona like ultrafast demagnetization at short-time delay, precise measurement of exact temporal resolution and time zero, when both pump pulse and probe pulse arrives simultaneously, is important.

The full-width half maximum (FWHM) of correlation of pump and probe beam is 1.1 ps, it is also the time resolution of our system. We characterized zero time delay and time resolution with GaP detector works at 150 to 500 nm. When two 785 nm photons from pump and probe beam arrive at photodetector, they will combine and create a photon at 393 nm. The GaP detector was placed at the sample position during the measurement, and connected to the pre-amplifier the same way as we connect Si detector. The signal was collected with the same Labview program as TDTR measurement. In Fig. 3.2, the time resolved light intensity is measured with GaP. We treat the time delay when pump-probe correlation reaches maximum as zero time, and the FWHM as time resolution of our measurement system. For our TDTB measurement, the time and the full-width-half-maximum of the pump-probe correlation is 1.1 ps

Due to the uncertainty relation ($\Delta E \Delta t = \text{const}$), the group velocity dispersion (GVD), or group delay dispersion (GDD), is the major limiting factor of pulse duration. The laser pulse comes out of Ti:Sapphire laser is 600 fs. The thick optical elements (EOM) and optics with sharp cutoff wavelength (ultrasteep edge filters) have large GDD values. After laser beam passes through these optics, the GDD values add up and cause the delay of laser pulse.

A short pulse duration is preferred in magnetic resonance measurement. The magnetic resonance frequency of antiferromangetic materials ranges from hundreds of GHz to THz [57, 58, 59]. If we need ten data points for one oscillation period, 1.1 ps resolution can measure spin oscillation no more than 91 GHz, far away from the AFMR frequency range.

To further improve the temporal resolution, one can replace the high GDD optics to low GDD optics or add optics with negative GDD to the system to lower overall GDD. We replaced ultrasteep edge filters to steep edge filters, and use an ultrasteep edge filter in front of photo detector to reduce the total GDD

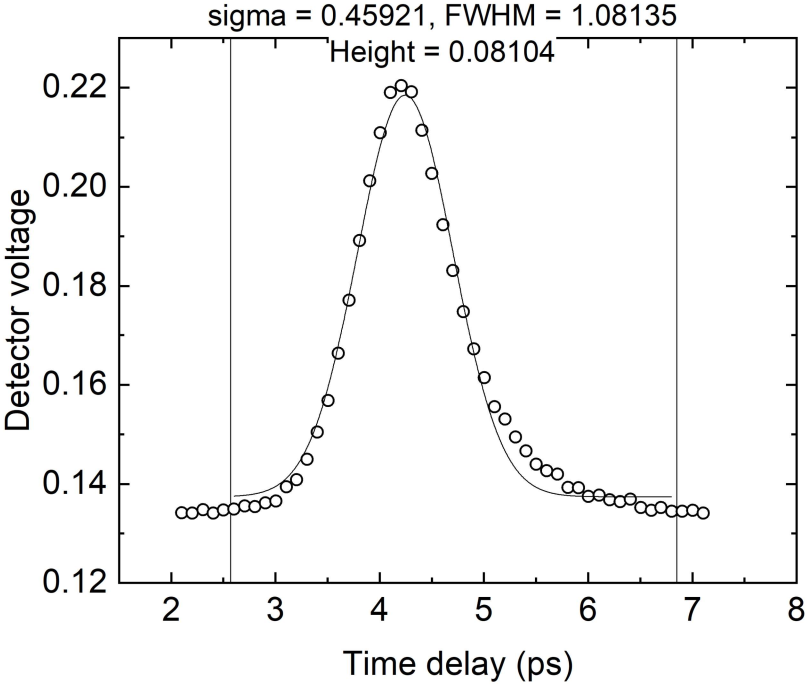

Figure 3.2: The pump-probe correlation of OPO.

value of the system. Now we have ultrasteep short-pass filters (Semrock SP01-785RU-25, 785 nm) in pump beam path, shallower long-pass filter (Semrock FF01-776/LP-25, 776 nm) in probe beam path, ultrasteep long-pass filter (Semrock LP02-785RE-25, 785 nm) in front of Si detector. The FWHM of cross-correlation of pump and probe lowered from 1.2 ps to 0.8 ps. In our new pump-probe system used OPO for laser source, we used acoustic optic modulator (AOM) instead of EOM for a smaller GDD because the crystal of AOM is thinner.

3.2.4 Density Functional Theory Calculation Methods

The first-principles calculations performed by collaborator using density functional theory (DFT) as implemented in the Vienna *Ab-Initio* Simulation Package [60, 61, 62] (VASP). The generalized-gradient approximation (GGA) formulated by Perdew, Burke, and Ernzerhof [63] (PBE) is used to describe exchange and correlation. The projector-augmented wave [64] (PAW) scheme is used to describe the electron-ion interaction. To sample the Brillouin zone a 15 × 15 × 5 Monkhorst-Pack [65] (MP) **k**-point grid is used and the Kohn-Sham states are expanded into plane waves up to a cutoff energy of 600 eV. Total energies are converged to self consistence within 10^{-6} eV. Noncollinear magnetism and spin-orbit coupling are included and the magnetic unit cell of Fe_2As is used to compute relaxed atomic geometries, electronic structure, and optical properties. Phonon dispersion is computed using finite displacement method as implemented in VASP and extracted using the phonopy package [66]. After convergence test, a 3 × 3 × 2 supercell and 4 × 4 × 4 MP **k**-point grid is used. For phonon calculation, noncollinear magnetism and spin-orbit coupling is included.

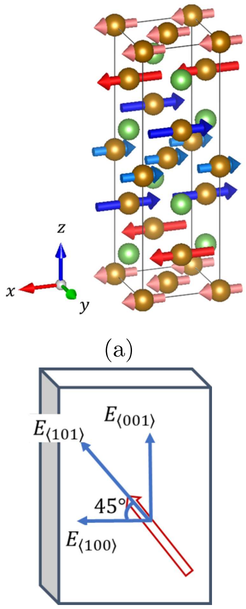

(a)

(b)

Figure 3.3: (a) Tetragonal magnetic unit cell of Fe_2As. Arsenic atoms are depicted as green spheres; Fe as brown spheres. Arrows denote the local magnetic moment of the Fe atoms. Fe atoms labelled with blue and pink arrows are crystallographically equivalent. The Cartesian coordinates x, y, z are aligned along the crystallographic a, b, c axes. (b) Experimental geometry for the time-domain thermo-birefringence (TDTB) and time-domain thermoreflectance (TDTR) experiments with the probe beam normal to the (010) face of the Fe_2As crystal. In TDTR measurements, the polarization of the probe is along x or z. In TDTB measurements, the polarization of the probe is at an angle of 45° from the x axis.

3.3 Optical and Thermal Properties Measurements

First, we discuss measurements of refractive index, electrical conductivities, heat capacity, and thermal conductivities of Fe_2As. We use the refractive index to describe the optical properties of the material and to relate thermo-reflectance and thermo-birefringence. We measure the heat capacity and decompose it into electron, phonon, and spin contributions; this allows us to compare the magnetic heat capacity to temperature dependent TDTB. From the heat capacity and thermal conductivity, we model the time-evolution of the temperature excursion created by the pump optical pulse. Finally, the combination of the measured electrical conductivity and the Wiedemann-Franz law allows us to separate the electronic and lattice contributions to the total thermal conductivity.

The equivalence of the x-axis and y-axis was demonstrated in prior work by neutron diffraction [52, 67] and torque magnetometry [68]. First-principles density functional theory (DFT) calculations give the ground-state lattice parameters as $a = 3.624$ Å and $c = 5.860$ Å, within 2% of powder X-ray diffraction measurements at room temperature, $a = 3.628$ Å and $c = 5.978$ Å. The magnetic unit cell used in the calculation is twice as long in the z direction. The Néel vector in ground-state DFT calculations is oriented along the x direction of the lattice. We confirmed the easy-plane magnetic structure by measuring the temperature dependent magnetic susceptibilities along the x and z crystallographic directions with a vibrating sample magnetometer.

In the absence of magnetic order, the dielectric tensor of a tetragonal crystal is isotropic in the x-y plane. However, if the Néel vectors have a preferred direction in the x-y plane, the dielectric function is anisotropic on length scales smaller or comparable to the characteristic size of the magnetic domains. We expect that different magnetic domains are approximately randomly oriented along the x and y directions and that our laser beam size is large compared to the domain size. Therefore, the dielectric function we measure in the x-y plane is isotropic.

3.3.1 Refractive index of Fe_2As

An effective isotropic refractive index of Fe_2As was measured by ellipsometry of the (001) and (010) faces of the crystal. Immediately prior to the ellipsometry measurements, which take place under ambient conditions, we removed surface oxides and contaminants using argon ion beam milling. The effective isotropic refraction index is $n = 2.9 + i3.3$ at a wavelength of $\lambda = 780$ nm. The optical reflectance calculated from this index of refraction is 0.56. The measured optical reflectance for both the (001) and (010) surfaces of the crystal at normal incidence and $\lambda = 780$ nm is 0.50. The optical absorption depth, $\lambda/(4\pi k)$, is 19 nm. The refractive index, computed using DFT, for light polarized along the x, y and z-axis of the crystal is $n = \sqrt{\epsilon} = 4.295 + i3.496$, $4.300 + i3.501$ and $3.381 + i4.039$ at 0 K, with a reflectance of 0.573, 0.574 and 0.619, respectively.

3.3.2 Electrical Resistivity of Fe_2As

The electrical resistivity of a polycrystalline sample of Fe_2As was reported previously as $\approx 220\ \mu\Omega\,\mathrm{cm}$ at $T = 300$ K [37]. The electrical resistivity has a shallow maximum near room temperature and decreases to $\approx 125\ \mu\Omega\,\mathrm{cm}$ at $T = 1$ K. We confirmed a value of electrical resistivity of our samples near room temperature of 240 $\mu\Omega\,\mathrm{cm}$ and the residual resistivity ratio at 300 K of 1.7. The stoichiometry of Fe_2As was evaluated using Rutherford backscattering spectrometry and Rietveld refinements to synchrotron X-ray and neutron

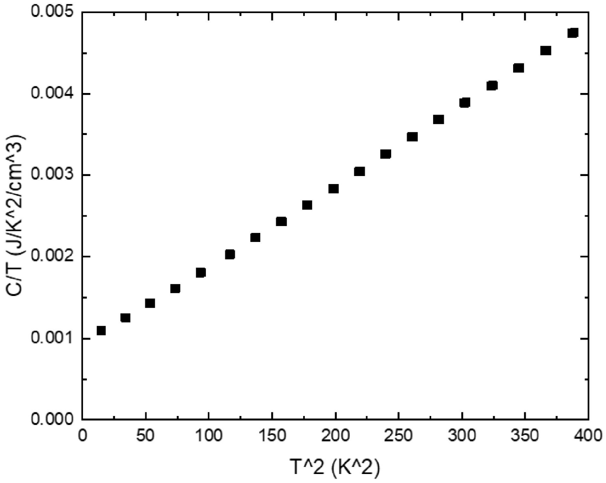

Figure 3.4: The total heat capacity of Fe_2As at low temperature plotted as C_v/T vs T^2. The low temperature heat capacity of metal can be expressed as $C(T) = \gamma T + \beta T^3$. By doing a linear fitting of plot, one can get γ =22 $\mathrm{mJ\,K^{-2}\,mol^{-1}}$, β =0.26 $\mathrm{mJ\,K^{-4}\,mol^{-1}}$.

diffraction data. These measurements converge on a slight Fe deficiency of 0.05 to 0.08 out of 2. This value also agrees with the nominal Fe:As ratio used during synthesis (1.95:1). (Nominally 2.00:1 samples exhibit metallic Fe impurities.) The high concentration of Fe vacancies in Fe_2As likely causes the large residual resistivity.

3.3.3 Magnetic Heat Capacity of Fe_2As

We measured the total heat capacity of a 35.5 mg sample of Fe_2As with a Quantum Design Physical Property Measurement System (PPMS), see Fig. 3.5a. The total heat capacity composes of contributions from electrons, phonons and magnons: $C_{tot} = C_p + C_e + C_m$. In free electron model, electron heat capacity is linear to temperature, can be expressed as $C_e = \frac{\pi^2}{3} k_{\mathrm{B}}^2 T D(E_{\mathrm{F}}) = \gamma T$. At low temperature, the phonon heat capacity is propotional to cubic temperature. The heat capacity of metal can be written as $C(T) = \gamma T + \beta T^3$. As show in Fig. 3.4, one can plot low temperature total heat capacity as C/T vs T^2. If data is linear in the plot, it is safe to get γ value and β value by fitting the data linearly. By fitting the data points at low temperature with $C(T) = \gamma T + \beta T^3$, we obtained γ =22 $\mathrm{mJ\,K^{-2}\,mol^{-1}}$, β =0.26 $\mathrm{mJ\,K^{-4}\,mol^{-1}}$.

Without specific phonon density of states, phonon heat capacity can be estimated with Debye model. At low temperature, one can use $C_p = \beta T^3$ where $\beta = \frac{12\pi^4}{5} \frac{Nk}{T_D^3}$ to calculate Debye temperature T_{D}. And use Debye temperature to calculate phonon temperature with Debye model $C_p = 9Nk \left(\frac{T}{T_{\mathrm{D}}}\right)^3 \int_0^{T_{\mathrm{D}}/T} \frac{x^4 e^x}{(e^x-1)^2} dx$. The Debye temperature of Fe_2As calculated from data is 281 K. γ, β and the Debye temperature are close to literature value [37]. With C_e and C_p calculate, we can get C_m by subtracting C_e and C_p from total heat capacity. Due to the simple models we used in calculating C_p and C_e, part of the magnetic heat capacity is negative. Another reason of this bad estimation is the specific heat of antiferromagnetic magnons at low temperature is $\sim T^3$, the same order as phonon. (The specific heat of magnons in ferromagnets at low temperature is proportional to $T^{3/2}$). So the βT^3 term cannot represent phonon heat capacity completely.

Our collaborator helped to calculate the phonon heat capacity from the phonon density of states of the ground state crystal structure and magnetic ordering, as shown in Fig. 3.6b.The Debye temperature calculated from the phonon DOS is 286 K, in good agreement with the measured value of 296 K reported by Zocco *et al.* [37].

The electronic density of states was calculated with Mermin DFT [69] and finite electronic temperatures between 0 K and 400 K, see Fig. 3.6a for 300 K. From this data we calculate the electronic heat capacity C_e and electronic specific heat γ=7.41 $\mathrm{mJ\,K^{-2}\,mol^{-1}}$.

Finally, we assume that the magnetic heat capacity is given by the difference between the total heat capacity and the sum of the lattice and electronic heat capacities, $C_m = C_{tot} - C_p - C_e$. Because lattice heat capacity dominates the total heat capacity except at very low temperatures, small errors in the measurement of the total heat capacity or the calculation of the phonon heat capacity produce large uncertainties in the magnetic heat capacity. We do not yet understand the origin of the small peak in the heat capacity data near 110 K.

We also measured the thermal conductivity of Fe_2As normal to the (001) and (010) faces of the crystal using conventional TDTR measurements and modeling as shown in Fig. 3.5b. An 80 nm thick Al film was sputtered on the sample to serve as the optical transducer in the thermal conductivity measurement. We determined the thermal conductivity by fitting the data to a multilayer thermal model [34]. The electrical contribution to the thermal conductivity was estimated by using the combination of the Wiedemann-Franz law and the measured electrical resistivity. The thermal conductivity shows a small anisotropy at $T > 300$ K (see Fig. 3.5b) and the contributions to the thermal conductivity from phonons and electronic excitations are comparable. The phonon contribution, i.e. the difference between the measurement and the electronic contribution, is approximately 3.6 $\mathrm{W\,K^{-1}\,m^{-1}}$ and independent of temperature.

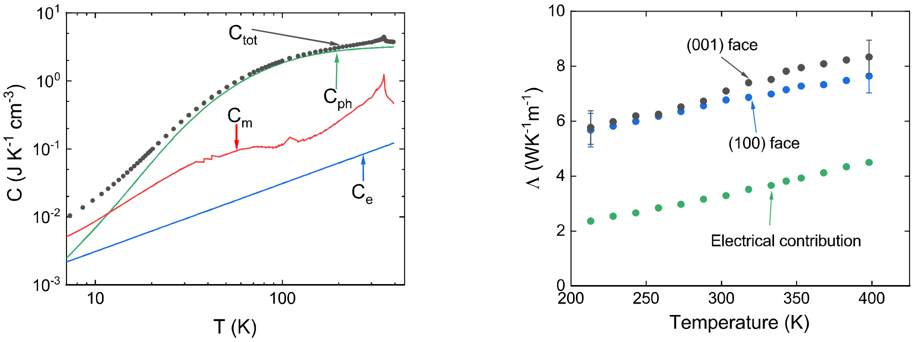

(a)

(b)

Figure 3.5: Heat capacity and thermal conductivity of Fe_2As. (a) The measured total heat capacity C_{tot} of Fe_2As and contributions to C_{tot} from excitations of electrons (e), phonons (ph), and magnons (m). The electronic and phonon contributions are calculated by density functional theory (DFT). The magnon contribution is derived by subtracting the calculated phonon and electronic contributions from C_{tot} . (b) The thermal conductivity in the direction normal to the (001) face (black circles) and (100) face (blue circles) shows a small anisotropy. The electrical contribution to the thermal conductivity (green circles) is calculated from the Wiedemann-Franz law and measurements of the electrical conductivity.

3.4 Time-domain Thermo-birefringence and Time-domain Thermoreflectance

In our experiments we probe changes in the optical function of Fe_2As induced by excitation of the sample by the pump beam. We use time-domain thermoreflectance (TDTR) to measure changes in the diagonal components of the dielectric tensor by fixing the probe polarization along various crystallographic directions and measuring transient changes in the *intensity* of the reflected probe pulse. We use time-domain thermo-birefringence (TDTB) to measure changes in the difference between the diagonal components of the dielectric tensor through transient changes in the *polarization* of the reflected probe pulse. For both TDTB and TDTR, the strongest signals we have observed are for pump and probe beams at normal incidence on the crystallographically anisotropic (010) surface of Fe_2As.

The instrument we used for the measurements of Fe_2As is the same as the instrument that we use for conventional TDTR measurements of thermal transport and time-resolved magneto-optical Kerr effect (TR-MOKE) of magnetization dynamics and thermally-driven spin generation and transport [70, 71].

The TDTB measurement geometry is shown in Fig. 3.3b and the measurement results for the Fe_2As (010) face are shown in Fig. 3.7a. In the discussion that follows, the symbol Δ indicates a transient quantity. To measure transient changes in the real part of the polarization rotation, $\text{Re}[\Delta\Theta] = \Delta\theta$, we null the balanced detector with a half-wave plate before the Wollaston prism that splits the orthogonal polarizations into two paths that are focused onto the two photodiodes of the balanced detector; to measure transient changes in

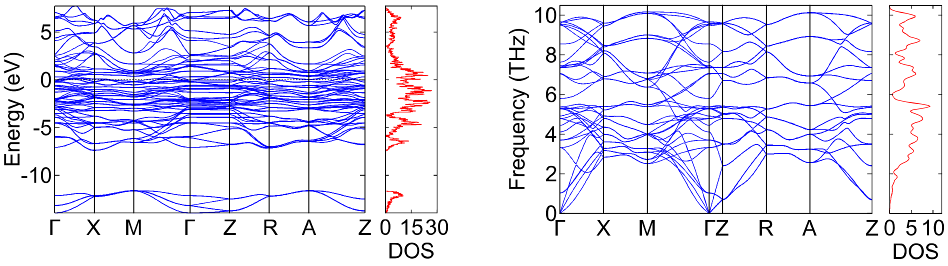

(a) (b)

Figure 3.6: (a) Calculated electronic band structure and electronic density of states (DOS) of Fe_2As. The electronic band structure include spin-orbit coupling effect through a non-collinear magnetism calculation. (b) Calculated phonon dispersion and phonon DOS of Fe_2As. For (a), the units of the electronic DOS are the number of states per magnetic unit cell per eV; for (b), the units of the phonon DOS are the number of states per magnetic unit cell per THz.

the imaginary part of the rotation, i.e., the ellipticity $\mathrm{Im}[\Delta\Theta] = \Delta\kappa$, we null the balanced detector with a quarter-wave plate. The polarization of the probe-beam is in the $x-z$ plane and 45° from the x axis. Corresponding TDTR data for a bare Fe_2As (010) face, i.e. uncoated by a metal, is shown for the two orthogonal polarizations in Fig. 3.10a.

Optical reflectance is the ratio of the intensity of the reflected electrical field to the intensity of the incident electric field: $R_z = |r_{zz}|^2$ and $R_x = |r_{xx}|^2$ where r_{zz} and r_{xx} are the Fresnel reflection coefficients for light polarized along the z and x directions, respectively. $r_{ii} = (n_{ii} - 1)/(n_{ii} + 1)$ where n_{ii} are diagonal elements of the optical index of refraction tensor; $n_{ii}^2 = \varepsilon_{ii}$ where ε_{ii} are diagonal elements of the dielectric tensor.

The birefringence of Fe_2As is relatively small. We therefore define average quantities $\bar{n} = (n_{xx} + n_{zz})/2$; $\bar{\varepsilon} = \bar{n}^2$; and $\bar{r} = (\bar{n} - 1)/(\bar{n} + 1)$. The complex rotation of the polarization of the reflected probe light is then

$$\Theta \approx \frac{(r_{xx} - r_{zz})}{2\bar{r}} \approx \frac{(n_{zz} - n_{xx})}{(1 - \bar{n}^2)} \approx \frac{(\varepsilon_{zz} - \varepsilon_{xx})}{2\sqrt{\bar{\varepsilon}}(1 - \bar{\varepsilon})}. \tag{3.2}$$

We use Eq. 3.2 to relate the polarization rotation angle to differences in the index of refraction or differences in the dielectric function. We evaluate Eq. 3.2 using the measured refractive index $n = 2.9 + i3.3$. The real and imaginary parts of the TDTB signal can then be written as $\Delta\theta = 0.005(\Delta\varepsilon'_{zz} - \Delta\varepsilon'_{xx}) - 0.003(\Delta\varepsilon''_{zz} - \Delta\varepsilon''_{xx})$ and $\Delta\kappa = 0.003(\Delta\varepsilon'_{zz} - \Delta\varepsilon'_{xx}) + 0.005(\Delta\varepsilon''_{zz} - \Delta\varepsilon''_{xx})$, where ε'_{ii} and ε''_{ii} are real and imaginary parts of the relative dielectric tensor.

Because the reflectance R_i is a function of complex dielectric function ε_{ii}, the transient reflectance, or TDTR signal, can be written as $\Delta R = \frac{\partial R}{\partial \varepsilon'}\Delta\varepsilon' + \frac{\partial R}{\partial \varepsilon''}\Delta\varepsilon''$. After taking partial derivative of reflectance and inserting the static dielectric function calculated from the measured refractive index, the transient reflectance can be written as a linear combination of transient dielectric functions, $\Delta R_i = -0.01\Delta\varepsilon'_{ii} + 0.007\Delta\varepsilon''_{ii}$.

We note that the difference in the TDTR measurements along x and z closely resembles the real part of the TDTB signal, $\Delta\theta$. This is because the linear coefficients of the transient changes in the components of the dielectric tensor that contribute to $\Delta R_x - \Delta R_z$ are approximately twice the linear coefficients of the transient changes in the components of the dielectric tensor that contribute to $\Delta\theta$. In other words, $\Delta\theta \approx -(\Delta R_z - \Delta R_x)/2$. Alternatively, if we write the complex TDTB signal as an amplitude and phase in the form $\Delta\Theta = |z|e^{i\delta}$, the real part of the TDTB signal is $\Delta\theta = |z|\cos\delta$, while in TDTR measurement, $\Delta R_z - \Delta R_x = 2|z|$.

The per pulse heating, i.e., the temperature excursion produced by a single optical pulse of the pump beam, is $\Delta T(t) \approx 3$ K. Due to the small temperature excursion, the change in the sublattice magnetization ΔM is small compared to the sublattice magnetization M, except for T very close to T_N. This justifies a description of the experiment in terms of linear response, except for T very close to T_N.

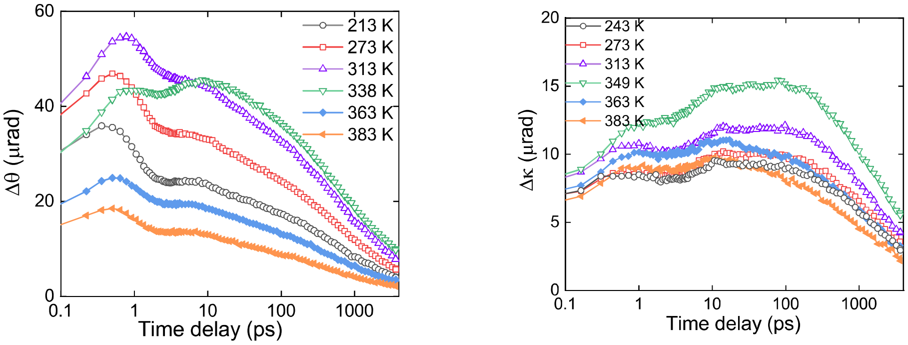

(a) (b)

Figure 3.7: (a) The real part of the time-domain thermo-birefringence (TDTB) signal measured on the (010) face of Fe_2As; and (b) the imaginary part of the TDTB signal. The temperature in the legend is the temperature of the sample stage; the spatially averaged temperature of the area of the sample that is measured in the TDTB experiment is the sum of stage temperature and the steady-state heating of 13 K. When stage temperature is at 338 K, the temperature of measured region of the sample is close to $T_N = 350$ K. Empty symbols denote data acquired at $T < T_N$; filled circles are data for $T > T_N$. We attribute the slower response at $T \approx T_N$ to the peak in the magnetic heat capacity at T_N.

3.5 Jones Matrix Derivation of TDTB Measurement

Jones matrix is a matrix representative to study light polarization. In Jones matrix scheme, light is represented with the two-dimensional vector where two elements represent two orthogonal polarized electrical field, and optics are represented by 2×2 matrix. If incoming light is $\mathbf{E}$ and it passes through a series of optics

($\mathbf{M_1}$, $\mathbf{M_2}$, $\mathbf{M_3}$, ...) sequentially, the Jones matrix of outgoing light is $...\mathbf{M_3 M_2 M_1 E}$, a two-dimensional vector.

3.5.1 Jones Matrix Calculation of the Real Part of the Birefringence Measurement

For a magnetic sample with perpendicular incident light and in-plane magnetic moment, we can measure the magnetic birefringence term by changing the light polarization to the 45° from the magnetic moment. What we measured with this configuration is difference of diagonal elements of dielectric constant, or the birefringence. Fig.3.8a shows a typical setup for measuring the real part of the MOKE signal.

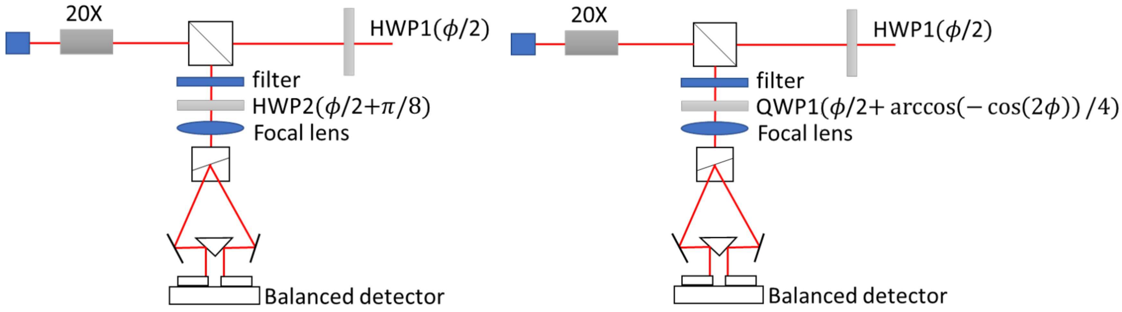

(a) (b)

Figure 3.8: (a) The setup for measuring the real part of MOKE or birefringence signal. The HWP1 is the half wave plate used to rotate the light, while the HWP2 is used to balance the detector. (b) The setup for measuring the imaginary part of MOKE or birefringence signal. The HWP1 is used to rotate the light polarization, while the QWP1 is used to balance the detector.

The Jones matrix of a half wave plate here is

$$HWP(\gamma) = \begin{pmatrix} \cos 2\gamma & \sin 2\gamma \\ \sin 2\gamma & -\cos 2\gamma \end{pmatrix} \tag{3.3}$$

If we define a reflectance matrix of the magnetic materials with magnetization stay in-plane as

$$M = \begin{pmatrix} r_{xx} & 0 \\ 0 & r_{zz} \end{pmatrix} = r_0 \begin{pmatrix} 1+\alpha & 0 \\ 0 & 1+\beta \end{pmatrix} \tag{3.4}$$

The $\alpha - \beta$ is the difference of diagonal components. The incident probe light polarization was rotated by ϕ by HWP1. Then the probe beam reflected back by the sample and balanced by HWP2. The optical axis position of HWP1 is $\phi/2$, and the position of HWP2 can be calculated with $\alpha = \beta = 0$, because we assume both α and β are much smaller than 1.

$$\begin{aligned}
\begin{pmatrix} E_x \\ E_z \end{pmatrix} &= HWP(\gamma) \cdot M(\alpha = \beta = 0) \cdot HWP(\phi/2) \begin{pmatrix} 0 \\ 1 \end{pmatrix} \\
&= r_0 \begin{pmatrix} -\sin(2\gamma - \phi) \\ \cos(2\gamma - \phi) \end{pmatrix}
\end{aligned} \tag{3.5}$$

If the light is balanced by HWP2, $|E_x|^2 - |E_z|^2 = 0$. So that $\gamma = \phi/2 + \pi/8$. Then we fix the angle of HWP2 to $\phi/2 + \pi/8$ to calculated the measured Kerr angle by balanced detector.

$$\begin{aligned}
\begin{pmatrix} E_x \\ E_z \end{pmatrix} &= HWP(\phi/2 + \pi/8) \cdot M \cdot HWP(\phi/2) \begin{pmatrix} 0 \\ 1 \end{pmatrix} \\
&= r_0 \begin{pmatrix} \frac{1}{4}\left(-\sqrt{2}(2 + \alpha + \beta) + 2(\alpha - \beta)\sin[(\pi + 8\phi)/4]\right) \\ \frac{1}{4}\left(\sqrt{2}(2 + \alpha + \beta) - 2(\alpha - \beta)\cos[(\pi + 8\phi)/4]\right) \end{pmatrix}
\end{aligned} \tag{3.6}$$

The Kerr rotation is $\widetilde{\theta} = (|E_x|^2 - |E_z|^2)/(2|E_x|^2)$. The relation between ϕ and θ was plotted in Fig.3.9a, and it was compared to measurement data.

When $\phi = \pi/4$, $\alpha = \alpha_x + i\alpha_y$ and $\beta = \beta_x + i\beta_y$, what the balanced detector reads is $(\alpha_x - \beta_x) + 1/2(\beta_x^2 + \beta_y^2 - \alpha_x^2 - \alpha_y^2)$. The transient measurement result $-\Delta\theta \approx \Delta(\alpha_x - \beta_x)$ is quadratic Kerr rotation signal.

3.5.2 Jones Matrix Calculation of the Imaginary Part of the Birefringence Measurement

To measure the imaginary part of the birefringence signal, the half wave plated in front of the balanced detector was replaced by a quarter wave plate shown as Fig. 3.8b. The Jones matrix of a quarter wave plate is

$$QWP(\sigma) = \begin{pmatrix} \cos^2\sigma + i\sin^2\sigma & (1-i)\sin\sigma\cos\sigma \\ (1-i)\sin\sigma\cos\sigma & \sin^2\sigma + i\cos^2\sigma \end{pmatrix} \tag{3.7}$$

where σ is the angle between optical axis and lab reference.To figure out the position of QWP1 to balance the detector, we suppose sample the nonmagnetic and let two outgoing orthogonal beams are at same intensity

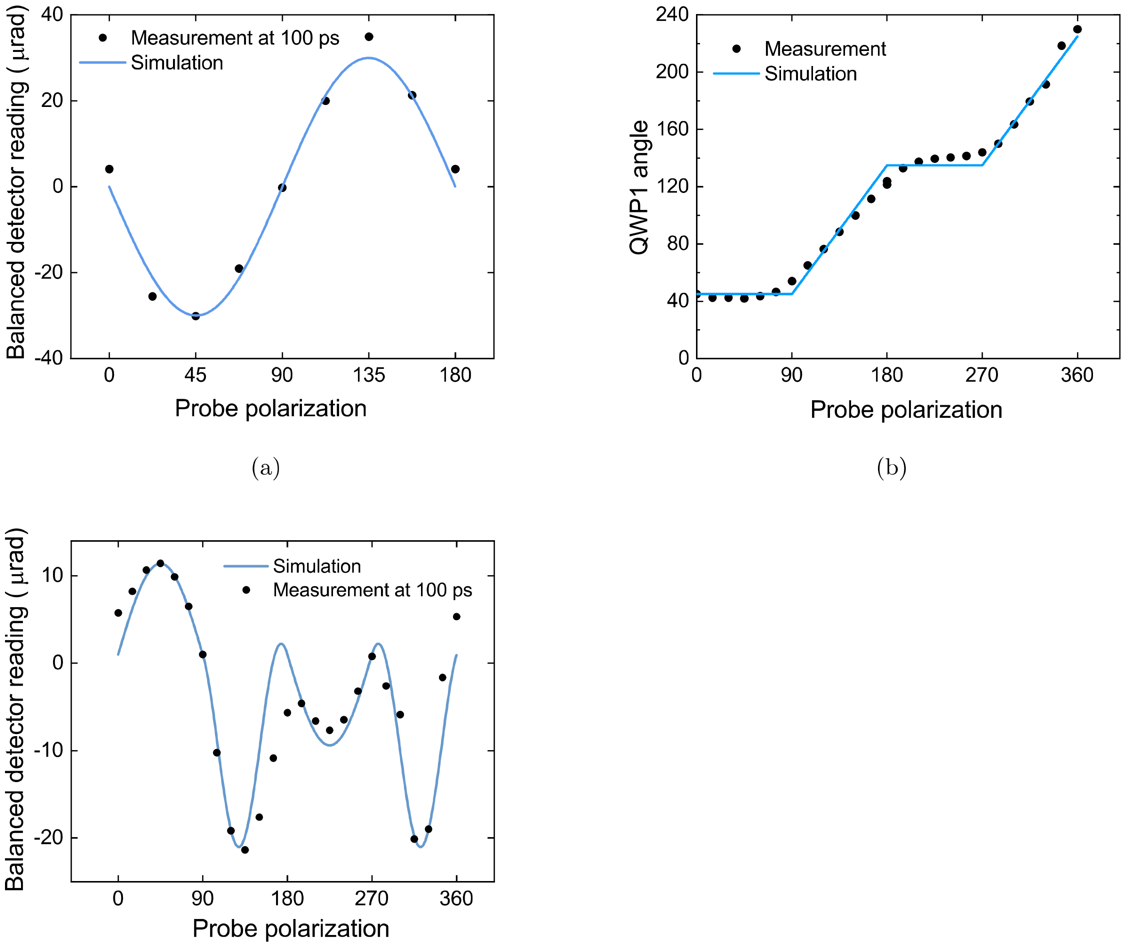

(a)

(b)

(c)

Figure 3.9: (a) The relation between balanced detector reading and light polarization in the real part of TDTB measurement at room temperature with fixed time delay 100 ps. (b)The relation between QWP1 angle used to balance detector and light polarization with the setup shown in Fig. 3.8b. (c)The relation between balanced detector reading and probe polarization in the imaginary part of TDTB measurement. The data were collected with fixed time delay 100 ps at room temperature.

$E_x^2 = E_z^2$.

$$\begin{aligned}\begin{pmatrix} E_x \\ E_z \end{pmatrix} &= QWP(\sigma)\cdot M(\alpha=\beta=0)\cdot HWP(\phi/2)\begin{pmatrix} 0 \\ 1 \end{pmatrix} \\ &= r_0 \begin{pmatrix} \frac{-1-i}{2}\left(\sin(2\sigma-\phi)+i\sin(\phi)\right) \\ \frac{1+i}{2}\left(\cos(2\sigma-\phi)+i\cos(2\phi)\right) \end{pmatrix}\end{aligned} \tag{3.8}$$

When $|E_x|^2 = |E_z|^2$ is satisfied, $\sigma = \frac{1}{4}\left(2\phi + \arccos[-\cos(2\phi)]\right)$. The relation between light polarization ϕ and QWP1 angle σ is shown in Fig.3.9b, which fits measurement results very well.

With QWP1 balances detector, the Jones matrix of the outgoing light is

$$\begin{pmatrix} E_x \\ E_z \end{pmatrix} = QWP(\frac{\arccos[-\cos(2\phi)] + 2\phi}{4}) \cdot M \cdot HWP(\phi/2) \begin{pmatrix} 0 \\ 1 \end{pmatrix} \tag{3.9}$$

And the measured signal by balanced detector is $\kappa = (|E_z|^2 - |E_x|^2)/|E_z|^2$. The calculated quadratic Kerr ellipticity signal versus light polarization is shown in Fig. 3.9c. When $\phi = 45°$, $\sigma = 45°$, and $\alpha = \alpha_x + i\alpha_y$ and $\beta = \beta_x + i\beta_y$, the balanced detector reading is $(\beta_y - \alpha_y) + (\alpha_x\beta_y - \beta_x\alpha_y)$, so in the transient measurement, the balanced detector reading is imaginary part of birefringence $\Delta\kappa = \Delta(\beta_y - \alpha_y)$. When $\phi = 135°$, $\sigma = 90°$, the balanced detector reading is $(\alpha_x - \beta_x) + 1/2(\alpha_y^2 - \beta_y^2 + \alpha_x^2 - \beta_x^2)$. In this case, the transient measurement result is real part of birefringence. Therefore, in Figure 3.9c, both real and imaginary part of Kerr rotation contribute to the balanced detector reading. Also, the intrinsic $\Delta\theta$ and $\Delta\kappa$ should have the same sign.

3.5.3 Jones Matrix Calculation of Polar MOKE Measurement

For a polar MOKE measurement setup, the polarization of perpendicular incident light changes by out-of-plane magnetization. Similarly, we use HWP and QWP measure real and imaginary part of polar MOKE signal, but 45 degree incident light polarization is not needed. Suppose the out-of-plane direction is along z-axis, and sample plane is xy-plane, the reflectance matrix of the magnetic materials with out-of-plane magnetization is:

$$M = \begin{pmatrix} r_{xx} & r_{xy} \\ r_{yx} & r_{yy} \end{pmatrix} = r_0 \begin{pmatrix} 1 & \delta \\ -\delta & 1 \end{pmatrix} \tag{3.10}$$

where we assume $r_{xy} = -r_{yx} = r_0\delta$ and δ is introduced by out-of-plane magnetization. The complex δ can be decomposed into $\delta = \delta_x + i\delta_y$. The electrical field after reflected back from sample and passing through HWP is

$$\begin{aligned} \begin{pmatrix} E_x \\ E_z \end{pmatrix} &= HWP(\pi/8) \cdot M \cdot \begin{pmatrix} 0 \\ 1 \end{pmatrix} \\ &= \frac{\sqrt{2}}{2} r_0 \begin{pmatrix} \delta + 1 \\ \delta - 1 \end{pmatrix} \end{aligned} \tag{3.11}$$

After Wollaston prism, E_x and E_y are separated and measured with balanced detector. The differential signal balanced detector measured is

$$I_x - I_y = |E_x|^2 - |E_y|^2 = 2r_0\delta_x \tag{3.12}$$

One can normalize the signal with $2(I_x + I_y)$ to get δ_x value. To get the imaginary part of δ, we normally replace HWP as QWP to balance the signal. The relation of incident light polarization and QWP angle was plotted in Fig. 3.9b. As we are using 90 degree linearly polarized light, the angle of QWP is 45 degree. So the electrical field after QWP is

$$\begin{aligned}
\begin{pmatrix} E_x \\ E_z \end{pmatrix} &= QWP(\pi/4) \cdot M \cdot \begin{pmatrix} 0 \\ 1 \end{pmatrix} \\
&= \frac{1}{2}\begin{pmatrix} 1+i & 1-i \\ 1-i & 1+i \end{pmatrix} \cdot r_0 \begin{pmatrix} 1 & \delta \\ -\delta & 1 \end{pmatrix} \cdot \begin{pmatrix} 0 \\ 1 \end{pmatrix} \\
&= \frac{ir_0}{2}\begin{pmatrix} i\delta + 1 \\ \delta + i \end{pmatrix}
\end{aligned} \tag{3.13}$$

The differential signal balanced detector measured is

$$I_x - I_y = |E_x|^2 - |E_y|^2 = 2r_0\delta_y. \tag{3.14}$$

3.6 Discussion

Since the (010) face of a tetragonal crystal is fundamentally anisotropic, we cannot directly interpret the signals plotted in Fig. 3.7 as the result of changes in magnetization with temperature. However, two aspects of the data suggest a prominent role of magnetism and magneto-optic effects. First, the real part of the TDTB signal (see Fig. 3.7a), and the TDTR signal measured with the probe polarization along the z axis (see Fig. 3.10a), show a significantly slower response when the sample temperature is close to the Néel temperature, T_N. The transfer of thermal energy in a magnetic material is often described by a three temperature model, in which energy is transferred between electrons, phonons, and magnons on ultrafast time-scales [21, 22]. Since the magnon contribution to heat capacity reaches a maximum at T_N, the temperature rise of the magnon system in response to heating of the electronic system by the pump optical pulse is expected to be slower at temperatures near T_N. We attribute the slower response at $T \approx T_N$ to this effect and conclude that the real part of the TDTB signal, and the TDTR signal measured with polarization along the z-axis, are dominated by changes in the magnon temperature. The slowing down of the demagnetization of antiferromagnetic Fe_2As at $T \approx T_N$ is reminiscent of the slowing down of the demagnetization of ferromagnetic FePt:Cu at $T \approx T_C$ where T_C is the Curie temperature [22].

Second, the temperature dependence of the transient TDTB and TDTR signals at fixed time delays closely follows the magnetic heat capacity. In Fig. 3.11, we compare the complex thermo-birefringence signals $\Delta\Theta/\Delta T$ for the (010) plane of Fe_2As and the magnetic heat capacity derived from $C_m = C_{tot} - C_{ph} - C_e$. ($C_{tot}$ is measured by experiment and C_{ph} and C_e are calculated by DFT.) We use TDTB data acquired at pump-probe delay times near 100 ps when the electrons, magnons, and phonons are in thermal equilibrium, and the strain and temperature gradients within an optical absorption depth of the surface are small. As we discuss in more detail below, we expect that for a single mechanism, the magnetic contribution to the dielectric function of an antiferromagnetic material will scale with the magnetic energy and, therefore, transient changes in the dielectric function produced by a small temperature excursion will scale with the magnetic heat capacity C_m. At $T \approx T_N$, we expect that $\Delta\Theta/\Delta T$ will be more smoothly varying with T than C_m because of the inhomogeneous temperature distribution across the lateral extent of the pump and probe beams in the experiment.

In Fig. 3.11 we also include data for the temperature dependence of $\Delta\theta$ measured on the crystallographically isotropic (001) plane. We consistently observe a small signal that is approximately independent of position. We believe there are two mechanisms that contribute to this null result. For the (001) plane of Fe_2As, the two degenerate domain orientations should produce a cancellation of any TDTB signal when measured on a length scale large compared to the characteristic domain size. We have not yet determined the domain structure of our Fe_2As crystals but evidence from related materials [31, 3] suggest that the domain size is typically in the sub-micron range while the $1/e^2$ radius of the pump and probe laser beams is ≈ 5.5 μm. Furthermore, the lack of a significant TDTR signal for light polarized along the x direction of the (010) face suggests that magnetic contributions to the ε_{xx} and ε_{yy} elements of the dielectric tensor are small. We tentatively attribute the small transient birefringence signal that we observe on the (001) face to a small, uncontrolled miscut of the sample, i.e., a small misorientation between the surface normal and the c-axis of the crystal.

Since both the real $\Delta\theta$ and imaginary $\Delta\kappa$ parts of the TDTB signals measured on the (010) face have a temperature dependence that resembles the magnetic heat capacity, we conclude that both $\Delta\theta$ and $\Delta\kappa$ have significant magnetic contributions. However, $\Delta\theta$ and $\Delta\kappa$ do not have the same dynamics, see Fig. 3.7. In the $\Delta\theta$ data set, with the exception of data collected at $T \approx T_N$, the signal reaches a peak response at short delay times on the order of 1 ps. We interpret this signal as arising from the same type of out-of-equilibrium ultrafast demagnetization that is typically observed for ferromagnetic materials using pump-probe measurements of first-order magneto-optic Kerr effects. However, we cannot yet reliably distinguish between magnetic, electronic, lattice temperature, and lattice strain contributions to $\Delta\theta$ or $\Delta\kappa$.

In the $\Delta\kappa$ data set, the signal reaches a peak response on a time-scale on the order of 10 ps. We interpret this time scale as characteristic of the time needed to fully relax the thermoelastic stress within the near surface region of the crystal that determines the reflection coefficients of the probe beam. This interpretation is supported by the character of the TDTR signal measured on the (001) face, see Fig. 3.11, that also includes a large variation in the signal at $t < 20$ ps.

In most studies of the optical properties of materials, the thermal expansion of the material contributes to the temperature dependence of the dielectric tensor. Even though the thermal expansion is three-dimension, the measurement is only sensitive to the element along the surface normal direction η_{yy} of the elastic strain tensor exists, because the laser spot size is much larger than absorption depth. Thermal stress is generated when the pump optical pulse is partially absorbed by the near-surface region of the sample. Thermal strain in the in-plane direction is strongly suppressed in a pump-probe experiments because the thermal penetration depth, i.e., the depth of the heated region, is small compared to the lateral extent of the laser spot.

Right after the sample surface was heated, the strain pulses propagates away from the sample surface with the speed of sound. Because there is no impedance mismatch in the bulk sample, the reflected acoustic wave cannot be observed. However, the thermal expansion-induced strain is observed by TDTB measurement. The buildup speed of the thermal expansion is related to the rise of lattice temperature. Because relatively smaller electron-lattice and spin-lattice coupling factor, the lattice temperature rise is slower than electron and spin. Right after the laser excitation, the thermal expansion-induced strain has not built up. So the signal at short time delay is strain-free signal.

When electron, spin and lattice temperature are at equilibrium, the stress is zero because the stress σ_{yy} depends on the electron and phonon distribution change made by laser pulse. At long time scale, the thermal expansion-induced strain will follow the temperature decay of the sample as heat dissipated away.

On the other hand, strain in the out-of-plane direction can contribute to TDTB and TDTR signals. The probe beam is sensitive to the dielectric tensor of the near-surface layer of the crystal that lies within an optical absorption depth of the surface. On this length scale, strain normal to the surface evolves on a time scale given by the optical absorption depth divided by the longitudinal speed of sound. The longitudinal speed of sound from our DFT calculations is ≈ 5 nm/ps. Therefore, the characteristic time-scale is ≈ 4 ps. At $t \ll 4$ ps, *strain* normal to the surface is negligible; at $t \gg 4$ ps, *stress* normal to the surface is negligible. On long time scales, the decay of the strain normal to the surfaces will follow the decay of the surface temperature as heat diffuses into the bulk of the sample.

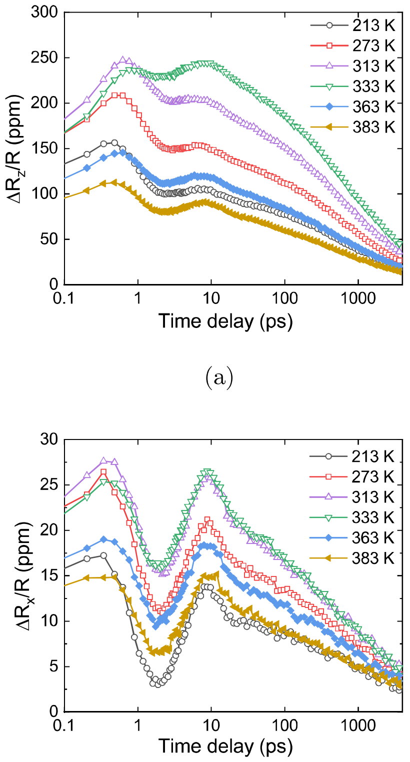

(a)

(b)

Figure 3.10: (a) Time domain thermoreflectance (TDTR) data for the (010) face of Fe_2As with (a) probe polarization aligned along the z-axis and (b) probe polarization aligned along the x-axis. TDTR data for $\Delta R_z/\Delta T$ shown in panel (a) is approximately an order of magnitude larger than TDTR data for $\Delta R_x/\Delta T$ shown in panel (b). The temperature in the legend is the temperature of the sample stage; the spatially averaged temperature of the area of the sample that is measured in the TDTR experiment is the sum of stage temperature and the steady-state heating of 13 K. Empty symbols denote data for temperatures $T < T_N$; filled symbols are for data acquired at $T > T_N$.

TDTB and TDTR signals are linearly related to transient changes in the dielectric function, see Eq. 3.2. The dielectric function tensor of magnetic materials can be written as [72]

$$\varepsilon_{ij} = \varepsilon_{ij}^0 + K_{ijk}M_k + G_{ijkl}^{\mathrm{MM}}M_kM_l + G_{ijkl}^{\mathrm{ML}}M_kL_l + G_{ijkl}^{\mathrm{LL}}L_kL_l \quad , \tag{3.15}$$

where the first term is the non-magnetic contribution to ε_{ij}, K_{ijk} are the first-order magneto-optical coefficients, and G_{ijkl} are the second-order magneto-optic coefficients. M is net magnetization , and L is the Néel vector. Because the net magnetization is zero in a collinear AF, the linear term, M_kM_l term and M_kL_l term can be neglected here, and we will use G_{ijkl} to represent G_{ijkl}^{LL} in what follows. We assume an equal population of magnetic domains with Néel vectors in the x and y directions.

To simplify the notation in the discussion below, we adopt the Voigt notation with, for example, G_{11}, G_{12}, and G_{31} replacing G_{1111}, G_{1122}, and G_{3311}, respectively. The tetragonal point group symmetry of Fe_2As has 6 independent and non-zero elements of the second-order magneto-optic tensor: $G_{11} = G_{22}$, $G_{12} = G_{21}$, $G_{13} = G_{23} = G_{31} = G_{32}$, G_{33}, $G_{44} = G_{55}$, and G_{66}. We assume that there is no correlation in the sublattice magnetization along the z axis; therefore, terms that involve the z-component of magnetization are small and we do not need to consider G_{33} or G_{44}. With the Néel vectors constrained to the x and y directions, the dielectric tensor is diagonal in the coordinate system of the crystal axes and we can also neglect G_{66}. The remaining contributions to the dielectric tensor involve three elements of the magneto-optic tensor:

$$\begin{aligned} \varepsilon_{11} &= G_{11}L_1^2 + G_{12}L_2^2 + \varepsilon_{11}^0 \\ \varepsilon_{22} &= G_{11}L_2^2 + G_{12}L_1^2 + \varepsilon_{22}^0 \\ \varepsilon_{33} &= G_{31}(L_1^2 + L_2^2) + \varepsilon_{33}^0 \quad . \end{aligned} \tag{3.16}$$

The microscopic mechanisms that contribute to the second-order magneto-optic coefficients G_{ijkl} include exchange interactions, spin-orbit coupling, and magnetostriction [51]. (Magnetostriction can be further divided into changes in the lattice parameters and, if the symmetry of the lattice is low enough, changes of the atomic positions within a unit cell [73].) Exchange interactions are usually assumed to dominate the isotropic contributions to the elements of G_{ijkl}, i.e., magnetic contributions that are independent of the orientation Néel vector. (The term "isotropic" does not imply that the magnetic contributions are the same for all elements of the dielectric tensor.) Spin-orbit interactions are usually assumed to dominate anisotropic contributions to G_{ijkl}, i.e., contributions that depend on the orientation of the Néel vector. Isotropic contributions are larger than anisotropic contributions in most materials [74, 51]. In collinear AFs with cubic symmetry, the anisotropic contribution to the dielectric function can be isolated from the isotropic contribution because birefringence can only be generated by anisotropic terms [75, 51].

Within the easy-plane of AFs with cubic, tetragonal, or hexagonal symmetry, optical birefringence can sometimes be used to image magnetic domains [76] because the anisotropy of the dielectric tensor is coupled to the orientation of the Néel vector. In a recent study of tetragonal CuMnAs [5], the transient birefringence signal measured in the x-y plane demonstrated the potential of using the anisotropic Voigt effect for determining the magnetic domain structure of tetragonal AFs. We find, however, that the Voigt effect is small for Fe_2As at the wavelength of our laser, $\lambda = 783$ nm, and we have not yet been able to use TDTB signals to study the magnetic domain structure.

On the (010) face of Fe_2As, approximately one-half of the domains have Néel vectors in the in-plane x direction and the other half of the domains have Néel vectors in the out-of-plane y direction. TDTB

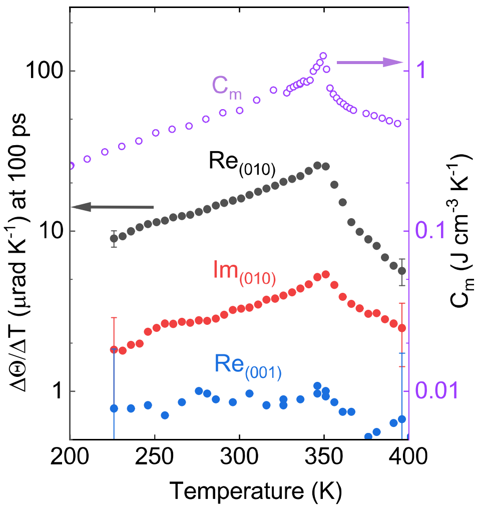

Figure 3.11: Comparison between $\Delta\Theta/\Delta T$ and magnetic specific heat as a function of sample temperature. The values for $\Delta\Theta$ are for 100 ps delay time. For each sample temperature T, ΔT at 100 ps at is calculated from a thermal model that uses the measured total heat capacity and thermal conductivity of Fe_2As as inputs to the model. The sample temperature T includes the effects of steady-state heating of measurement area that is created by the absorbed laser power. The real and imaginary parts $\Delta\Theta/\Delta T$ measured for the (010) face have a similar temperature dependence as the magnetic specific heat C_m.

signals acquired on the (010) plane are, in principle, sensitive to contributions from anisotropic terms in the magneto-optic coefficients generated by domains with Néel vectors in the x direction. TDTB signals are sensitive to contributions from isotropic terms generated by domains with Néel vectors in both the x and y directions. If the anisotropic contributions, e.g., the Voigt effect, were dominant, then $G_{11} \gg G_{31}$ [53, 54]. However, the TDTR data, see Fig 3.10, lead us to conclude that $\Delta\varepsilon_{zz} \gg \Delta\varepsilon_{xx}$, $G_{11} \ll G_{31}$, and the isotropic contribution to ε_{zz} is the dominant effect.

In previous studies of tetragonal transition metal fluorides [51, 77], the derivative of the magnetic linear birefringence with respect to temperature $d(\Delta n_m)/dT$, where Δn_m is the difference in the index of refraction between z and x axes of the crystal, has been shown to have the same temperature dependence as the magnetic specific heat. This behavior is expected because both the magnetic contributions to the dielectric function and the magnetic energy include terms that involve correlations of the products of the spin angular moment at different lattice sites. Contributions to the magneto-optic coefficients from various terms in the Hamiltonian could, however, have different constants of proportionality. Furthermore, in our time-domain thermo-birefringence (TDTB) measurements of the (010) face of the Fe_2As crystal, there are non-magnetic contributions to the TDTB signals that come from thermal excitations of electrons and phonons. The fact that the TDTB signals closely resemble the temperature dependence of the magnetic heat capacity supports

Table 3.1: Comparison of the quadratic magneto-optical coefficient G_{31} of antiferromagnetic Fe_2As determined in our work with selected previous studies of ferromagnetic (Fe, Co, Ni, $Y_3Fe_5O_{12}$) and antiferromagnetic (MnF_2, CoF_2) materials. Ni and Fe_2As have relatively large quadratic magneto-optic coefficients.

Materials	Wavelength (nm)	Magneto-optic data	Magnetization	Quadratic magneto-optical coefficient ($10^{-14}\mathrm{A}^{-2}\,\mathrm{m}^2$)
Fe [78]	670	$\varepsilon_{11} - \varepsilon_{12} = -(5.0 + i3.5) \times 10^{-2}$	$1.8 \times 10^6\,\mathrm{A\,m^{-1}}$	$G_{11} - G_{12} = -1.5 - i1.1$
Fe [79]	670	$\varepsilon_{11} - \varepsilon_{12} = -0.15 + i0.07$	$1.8 \times 10^6\,\mathrm{A\,m^{-1}}$	$G_{11} - G_{12} = -4.6 + i2.1$
Co [79]	670	$\varepsilon_{11} - \varepsilon_{12} = 0.10 - i0.13$	$1.4 \times 10^6\,\mathrm{A\,m^{-1}}$	$G_{11} - G_{12} = 5.1 - i6.6$
Ni [79]	670	$\varepsilon_{11} - \varepsilon_{12} = -0.75 + i0.20$	$5.0 \times 10^5\,\mathrm{A\,m^{-1}}$	$G_{11} - G_{12} = (-300 + i80)$
$Y_3Fe_5O_{12}$ [80]	1150	$\lvert n_\perp - n_\parallel \rvert = 3.9 \times 10^{-6}$	$1.4 \times 10^5\,\mathrm{A\,m^{-1}}$	$G_{11} - G_{12} = 1.6$
$KNiF_3$ [75]	632.8	$n_m = 3.3 \times 10^{-3}$	$1.3 \times 10^5\,\mathrm{A\,m^{-1}}$	$G_{11} = 60$
MnF_2[81]	632.8	$d(\Delta n_m)/dT = 5.0 \times 10^{-5}\ \mathrm{K^{-1}}$	$d(M^2)/dT$ $= -1.3 \times 10^{10}\ \mathrm{A^2\,m^{-2}\,K^{-1}}$	$\lvert G_{13} \rvert = 1.2$
CoF_2[81]	632.8	$d(\Delta n_m)/dT = 2.5 \times 10^{-5}\ \mathrm{K^{-1}}$	$d(M^2)/dT$ $= -1.2 \times 10^{10}\ \mathrm{A^2\,m^{-2}\,K^{-1}}$	$\lvert G_{33} - G_{13} \rvert = 0.63$
Fe_2As	783	$d(\varepsilon_{33})/dT$ $= (-1.5 + i0.21) \times 10^{-3}\ \mathrm{K^{-1}}$	$d(M^2)/dT$ $= -8.8 \times 10^8\ \mathrm{A^2\,m^{-2}\,K^{-1}}$	$G_{31} = (85 - i12)$

our conclusion that the TDTB signals are dominated by a magnetic contribution with a single underlying mechanism.

If we assume that the magnetic contribution dominates the temperature-dependence of ε_{33}, the magneto-optical coefficient G_{31} can be estimated by using the value of $\Delta\varepsilon_{33}$ and $\Delta(M_A^2)$, where M_A is sublattice magnetization of the AF. We estimate $\Delta(M_A^2)$ from our magnetic heat capacity data as described in the supplementary document. Because the sublattice magnetization is always real, the magneto-optic coefficient G_{31} is complex since $\Delta\varepsilon_{33}$ is a complex number.

$$G_{31} = \frac{\Delta\varepsilon_{33}/\Delta T}{2\Delta(M_A^2)/\Delta T} = \frac{(\Delta\varepsilon'_{33} + i\Delta\varepsilon''_{33})}{2\Delta(M_a^2)} \quad . \tag{3.17}$$

Inserting the value of the transient dielectric function and the temperature excursion of 1.5 K at a delay time of 100 ps and ambient temperature, 293 K, we find $G_{31} = (0.85 - i0.12) \times 10^{-12}\mathrm{A}^{-2}\,\mathrm{m}^2$. We emphasize that this value for G_{31} should be consider an estimate because we have assumed that the magnetic contribution dominates the temperature dependence of ε_{33}.

Finally, we compare the magnitude of our result for G_{31} of Fe_2As with the quadratic magneto-optic coefficients of several more commonly studied magnetic materials, see Table 3.1. In Table 3.1, G tensors are G^{MM} for ferromagnets and G^{LL} for antiferromagnets. In studies of ferromagnetic materials (Fe, Co, Ni, and $Y_3Fe_5O_{12}$), the magnetization vector can be manipulated with an external field and therefore the elements of the quadratic magneto-optic tensor G_{ij} can be calculated using Eq. 3.16 and $M^2 = M_s^2$, where M_s is the saturation magnetization. In studies of antiferromagnetic materials (MnF_2, CoF_2, and Fe_2As), typically, the Néel vector cannot be controlled with an external field and the values of G_{ij} are more difficult to determine. The measurements of antiferromagnetic MnF_2 and CoF_2 reported in Ref. [81] are collected from a crystallographic anisotropic plane; therefore, the magnetic birefringence data that we use in this analysis are the temperature derivatives of the birefringence data with the additional assumption that the magnetic birefringence has a stronger dependence on temperature than the crystalline birefringence. We used $M^2 = M_A^2$ to calculate the G_{ij} tensor for antiferromagnets, where M_A is sublattice magnetization. Typically, G_{11} and G_{13} or G_{12} cannot be determined separately based on birefringence data alone. Compared to the other materials listed in Table 3.1, Fe_2As and Ni have relatively large quadratic magneto-optic coefficients.

3.7 Calibration of Thermal Reflectance and Kerr Rotation Angle

3.7.1 Convert Raw TR-MOKE Data into Kerr Rotation

In a normal measurement, the MOKE we measured is proportional to magnetization $\theta \propto M$. In a pump-probe measurement, the pump beam heats the sample up and then magnetic sample starts demagnetization. So the signal what probe beam measures is magnetization change ΔM in response to the laser heating ΔT. Because of $\Delta\theta/\theta = \Delta M/M$, one is able to calculate ΔM value through both transient and static MOKE measurement. Furthermore, if the temperature excursion ΔT is small and temperature T is much smaller than critical temperature, the ΔM can be seen as a linear function of ΔT.

For our TR-MOKE measurement with pump-probe setup, the transient signal is double modulated, and demodulated by a RF lock-in and computer-based AF lock-in. The purpose of double modulation is just to improve signal-to-noise ratio, so both in-phase and out-of-phase signal should be the same as single modulation (turn off the chopper and measure from RF lock-in). While the transient signal was measured at pump frequency, the static signal we measured is at probe frequency. It is acceptable to measure static signal at pump frequency or with DC signal. The key point is to figure out the conversion factor of detectors to make sure the transient signal and static signal are comparable.

In our measurement, we used probe beam to do static measurement at 200 Hz. As we discussed in previous section, the polar MOKE signal δ measured from signal is

$$\delta = \frac{I_x - I_y}{2(I_x + I_y)} = \frac{I_x - I_y}{4I_0^2} = \frac{I_{AF,+} - I_{AF,-}}{4I_0^2} \tag{3.18}$$

where $I_0 = r_0^2$ is incident light intensity, and $I_x - I_y$ is off-diagonal change of reflection matrix comes from magnetization. In the measurement, $I_x - I_y$ is the intensity difference of two photodiodes of balanced detector at 200 Hz measured with AF lock-in. Here, I_x, I_y and I_0 are all measured at 200 Hz with AF lock-in. In a static MOKE measurement of Co/Pt multilayer with perpendicular magnetic anisotropy (PMA), the Co/Pt thin film is saturated with opposite poles of permanent magnetic (+M and -M). In this case, $I_x - I_y$ needs to be divided by an extra factor of 2 because magnetization is measured twice.

There are three outputs of the balanced detector we used (Thorlabs PDB450A), two are AF monitor output, which output intensity of two beams at AF frequency($I_{+,AF}$ and $I_{,AF}$); the other one is RF output, it gives intensity difference of two incoming beams at RF frequency.

In transient measurement, $I_x - I_y$ is measured at f_{pump} from RF lock-in and I_0 is measured at f_{probe} from AF lock-in, the transient MOKE signal is

$$\Delta\delta = \frac{V_{in,RF}}{4I_{0,RF}} = \frac{V_{in,RF}}{4I_{0,AF} \times F_c} \tag{3.19}$$

where F_c is the conversion factor between the reading from AF lock-in and the reading from RF lock-in. We considered four factors when transfer AF signal to RF signal:

1. Detector gain difference: for the balanced detector we used, the RF output is half the AF monitor output, the factor is 1/2.
2. RMS of first harmonic: with band pass filter connected to input RF lock-in, we are picking up the root mean square (RMS) of first harmonic. The wave form of pump beam is square wave, the same as function generator. The peak to peak amplitude of first harmonic of a square wave is $4/\pi$ times the amplitude of square wave. The RMS value of a sine function is $1/\sqrt{2}$ its peak-to-peak amplitude. The factor is $\frac{1}{\sqrt{2}} \cdot \frac{4}{\pi}$.
3. Impedance of lock-in: the impedance of RF lock-in is 50 Ω while the impedance of detector and AF lock-in is infinite. The factor is 1/2.
4. Gain of RF lock-in: the gain of RF lock-in is around 0.8 at 10.8 MHz. This can be measured by directly connect the output of a function generator to the input of RF lock-in. Why the factor is 0.8 is still unknown.

The input signal of the balanced detector is square wave. Suppose the amplitude of the square wave is A and the peak-to-peak voltage is $V_{pp} = 2\text{A}$. If we measure this square wave with a multimeter, the voltage one would get is $V_{DC} = A$. If one measure this square wave from AF lock-in, the observed voltage should be $V_{AF} = A \cdot \frac{1}{\sqrt{2}} \cdot \frac{4}{\pi} = 0.9A$. Both V_{DC} and V_{AF} are from monitor output of balanced detector. The RF output of balanced detector read from RF lock-in is $V_{RF} = A \cdot \frac{1}{2} \cdot \frac{1}{2} \cdot \frac{1}{\sqrt{2}} \cdot \frac{4}{\pi} \cdot 0.8 = 0.18A$. So the conversion factor F_c between V_{AF} and V_{RF} is 0.2.

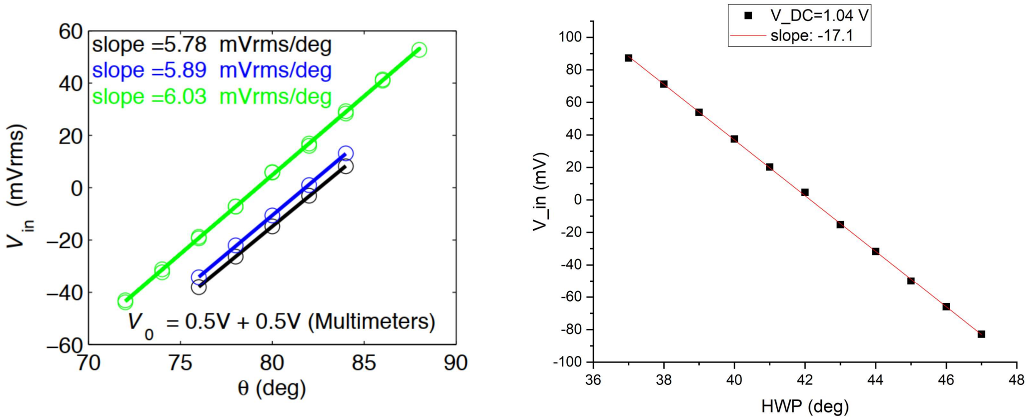

(a)

(b)

Figure 3.12: (a) The calibration data Johannes Kimling performed. The x-axis is light polarization angle, and the DC voltage of both monitor outputs are 0.5 V. (b) The calibration data I collected. The x-axis is half-wave-plate rotation angle, so the light polarization angle should be doubled. The DC voltage of either monitor outputs is 1.04 V.

A direct calibration of this conversion factor can be performed with pump beam only. In the calibration, one rotates the polarization of light with half wave plate, and read RF signal from RF lock-in to get a relationship between RF signal and the polarization rotation. During the calibration, we blocked the probe beam and remove the filter in front to balanced that was used to block pump beam. Then we connect monitor output to multimeter read the amplitude of signal V_{DC}. While we rotate the half wave plate by a small angle $\Delta\theta$, the RF signal will change linearly with the polarization by ΔV_{RF}.

In Fig. 3.12, the calibration recorded by our previous group member Johannes Kimling and the data I collected are shown. The conversion factor can be calculated with

$$\frac{\Delta V_{RF}}{\Delta\theta}\cdot\frac{1}{4V_{DC}}=\frac{\Delta V_{RF}}{\Delta\theta}\cdot\frac{1}{4V_{AF}\cdot 0.9}=\frac{F_c}{0.9} \tag{3.20}$$

The calculated F_c of Fig. 3.12a is 0.2, while the F_c calculated from Fig. 3.12b is 0.13. I think the discrepancy comes from factor 4, the gain of RF lock-in described above.

3.7.2 Calculate dR/dT, ΔR, ΔT from TDTR Data

In TDTR measurement where ratio is used to analyze data, knowing specific dR/dT value is not necessary, because it is cancelled out in ratio. However, in our TDTR measurement with Fe_2As sample, the TDTR signal strongly depends on probe polarization and magnetization. To compare our TDTR signal to our TDTB data and proves what we measured in TDTB is $\Delta R_{xx}-\Delta R_{zz}$, we need to know specific ΔR value from TDTR measurement.

To correctly calculate dR/dT, one needs to make sure the type of both transient signals ΔV_{in} and ΔT are the same. The dR/dT can be calculated with equation:

$$\frac{dR}{dT} = \frac{1}{GQ} \frac{\Delta V_{RMS}(t)}{V_0} \frac{R}{\Delta T_{RMS}(t)} \tag{3.21}$$

where $G = 5$ is gain of preamplifier, $Q \approx 10$ is is the quality factor of LC circuit combined with 50 Ω impedance in RF lock-in. It can be checked by comparing the reading after adding and removing the resonant circuit. V_0 is average output of the detector, and R is the reflectance of the sample. Here, we compare the root-mean-square value of both ΔV_{in} and ΔT. $\Delta V_{RMS}(t)$ the time-dependent in-phase signal read from RF lock-in. The peak-to-peak value of temerpature excursion $\Delta T_{p2p}(t)$ can be calculated with thermal transfer model as described in[82]. The maximal $\Delta T_{p2p}(t)$ value reflects the real temperature excursion on sample, and should be close to per pulse heating. $\Delta T_{RMS}(t) = \Delta T_{p2p}\frac{1}{2}\frac{1}{\sqrt{2}}\frac{4}{\pi}$. where 1/2 is the factor change peak to peak of square wave to amplitude of square wave, $4/\pi$ is the factor of picking up the first harmonic of square wave, and $1/\sqrt{2}$ is the factor amplitude of harmonic to RMS.

The dR/dT data of alunimum transducer I got is 1e-4 K^{-1} at 785 nm, in consistent with temperature dependent ellipsometry measurement reported in [83].

The relation between reflectance ΔR and ΔV_{in} described in [34] is

$$\frac{V_f}{V_0} = \frac{GQ}{\sqrt{2}} \frac{\Delta R}{R} \tag{3.22}$$

the same as equation showed above because the $2/\pi$ factor is considered in input pump power.

3.8 Conclusion

In collinear antiferromagnetic materials, the contribution to the diagonal elements of the dielectric tensor that are quadratic in sublattice magnetization can be probed with transient birefringence or reflectance measurements. In our measurement of time-domain thermo-birefringence (TDTB) and thermo-reflectance (TDTR) of Fe_2As, we observe that the dominant response of the dielectric tensor is in the z direction and perpendicular to the Néel vector. The temperature dependence of the TDTB signals closely follow the temperature dependence of the magnetic heat capacity, as expected if the exchange interaction is the dominant magnetic contribution to the dielectric function. In comparison to other magnetic materials, Fe_2As has relatively large quadratic magneto-optical coefficient at 783 nm.

Chapter 4

Magnetic Anisotropy of Fe_2As Measured with Torque Magnetometry

4.1 Introduction

4.1.1 Motivation

Antiferromagnets (AFs) have potential advantages over ferromagnets for spintronic device applications. Collinear AFs are relatively insensitive to external fields because the net magnetization is zero. AFs typically have higher antiferromagnetic resonance (AFMR) frequency than ferromagnets and therefore processional switching can occur in AFs at a faster rate than in ferromagnets.

The recent discovery of electrical manipulation and detection of spin configurations in metallic AFs has led to a rapidly expanding scientific literature on this class of magnetic materials. Tetragonal crystals with easy-plane magnetic anisotropy are preferred because the two degenerate orientations of the Néel vector can store binary information. In crystals with globally centrosymmetric but locally non-centrosymmetric magnetic structures—e.g., CuMnAs and Mn2Au—an electrical current exerts a torque on the Néel vector and the domain structure can potentially be switched electrically [5][31] [84][85].

A small value of the in-plane magnetocrystalline anisotropy facilitates electrical switching of the domain orientation since a smaller torque is needed to overcome the energetic barrier that separates the two orientations. A large value of the in-plane anisotropy, however, enhances the thermal stability of the domain. The Néel-Arrhenius law provides an estimate of the rate of thermal fluctuations of a single domain[86]:

$$\frac{1}{\tau} = f_0 \exp\left(-\frac{\Delta E}{k_B T}\right) \tag{4.1}$$

where τ is the average time between thermally-activated changes in the direction of the magnetization, f_0 is the resonance frequency, ΔE is the energy barrier between two degenerate magnetic states and $k_B T$ is the thermal energy. ΔE is given by the product of an anisotropy parameter K and the volume of the domain V; $\Delta E = KV$. Stable data storage typically requires $\Delta E/k_B T > 40$ to meet the criteria that data must be retained for 10 years [87].

For the media of conventional hard drives, the anisotropy parameter K is controlled by the perpendicular magnetocrystalline anisotropy of ordered intermetallic alloys. In the emerging technology of magnetic random access memory (MRAM), K is controlled by the interfacial magnetic anisotropy of a ferromagnetic layer adjacent to the oxide barrier in a magnetic tunnel junction. The perpendicular magnetic anisotropy K_1 of MRAM materials is typically $10^6 < K_1 < 10^7 \text{Jm}^{-3}$ [88].

4.1.2 Different Types of Anisotropy

For both ferroamgnetic and antiferromagnetic materials, magnetic anisotropy is the three-dimentional anisotropic distribution of energy. Thus spins prefer to align certain direction without external field to lower the total energy. A ferromagnetic sphere made of amourphous material is treated as magnetically isotropic, thus the magnetization will always parallel to external field and ferromagnetic spheres cannot get magnetized spontaneously.

Magnetic ansiotropy composes of shape anisotropy, magnetocrystalline anisotropy and stress-induced anisotropy.

The shape anisotropy of ferromagnetic materials origins from stray field (or demagnetization field). Demagnetization field is the alignment tendency of spins to reduce total magnetic energy. Because of zero net magnetization in compensated AFs, there is no stray field or shape anisotropy in AFs.

The magnetic energy of the system from demagnetization field can be represented by ferromagnetic ellipsoid:

$$\epsilon_m = \frac{1}{2}\mu_0 N V M_s^2 \tag{4.2}$$

where N is a three-dimensional demagnetization tensor and M_s is saturation magnetization. The anisotropic N value determines the energy minimum direction where the spins are aligning without external field or stress.

For needle shape ferromagnets, the ones we like to use in compass, the spins are along the needle axis (N is 0 along the needle axis, and 1/2 perpendicular to the needle axis). For thin films, e.g. 10 nm Co thin film, the spins prefer in-plane direction (N is 0 in the plane, and 1 perpendicular to the plane). For spheres, there is no shape anistropy because N is 1/3 everywhere.

Magnetocrystalline anisotropy is the magnetic ansitoropy originated from crystal structure of materials via spin-orbit coupling. The magnetocrystalline energy, is defined as the work required to make the magnetization lie along a certain direction compared to an easy direction.

There can also be a contribution to the interface anisotropy that is magnetoelastic in origin. This is related to stress relief by defect formation at interfaces. It is inversely related to the layer thickness and may therefore be significant at small thicknesses, so magnetic multilayers are widely used to produce perpendicualr magnetic ansitropy (PMA).

4.1.3 Magnetocrystallin Anisotropy of Antiferromagnetic Material Fe_2As

Magnetocrystalline anisotropy is described by a phenomenological expansion of the magnetic energy as a function of direction cosines for the orientation of magnetization of a ferromagnet or the sublattice magnetization of an antiferromagnet (AF). For a tetragonal crystal, the expansion to fourth order gives 3 coefficients K_1, K_2 and K_{22} [89]. K_1 is a second order coefficient; K_2 and K_{22} are fourth order coefficients.

$$E_{ani}/V = K_1 \sin^2\phi + K_2 \sin^4\phi + K_{22} \sin^4\phi \cos(4\theta) \tag{4.3}$$

where ϕ is the angle of the magnetization relative to the [001] direction and θ is the angle of the magnetization relative to the [100] direction (Fig. 4.3). The coefficient K_1 describes the two-fold anisotropy in (010) plane and K_2 is the higher order four-fold symmetry. Because the effect of $K_2$is usually much smaller than K_1, it will be neglected in the following discussion. A crystal with an easy-plane anisotropy is described by $K_1 < 0$. The coefficient K_{22} describes the four-fold anisotropy of the (001) plane and determines the thermal stability of an easy-plane structure.

An external magnetic field applied to an antiferromagnet (AF) produces a small induced magnetic moment. The induced moment is small because tilting of the orientation of sublattice magnetization is constrained by strong exchange interaction between the magnetic sublattices. In general, however, the induced magnetic moment is not parallel to the applied field because magnetocrystalline anisotropy favors an orientation of the sublattice magnetization along an easy axis [90][91].

The lack of alignment between the induced moment m and the applied field B produces a macroscopic torque on the sample, $\tau = \mathbf{m} \times \mathbf{B}$. A torque magnetometer measures this torque. Data for the torque as a function of applied field is sensitive to magnetocrystalline anisotropy as long as the anisotropy is not too small or too large. If the anisotropy is small, then the angle between m and B is small and the torque becomes difficult to detect. If the anisotropy is large, then the direction of m is fixed with respect to the crystallographic axis and the torque does not provide information about the magnitude of the anisotropy. We can measure the in-plane four-fold anisotropy of a mm-size bulk crystal of Fe_2As by torque magnetometry but the out-of-plane two-fold anisotropy is not accessible to this technique, because the external field is too small compare to anisotropy field to extract enough information. We instead employ first-principles calculations based on density functional theory to determine K_1.

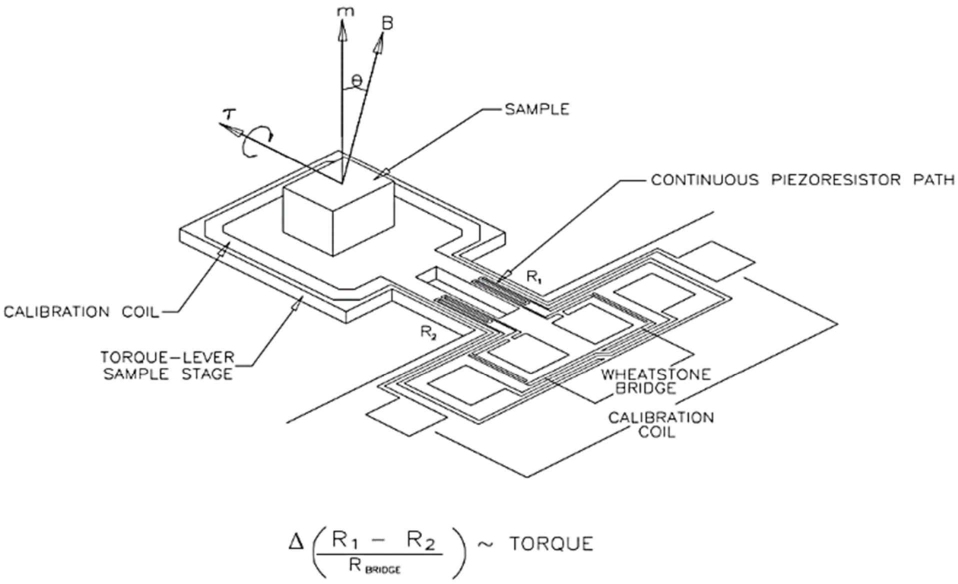

Figure 4.1: The chip for torque magnetometry measurements. When torque exerts on the torque-lever, the resistance of piezoresistor will change. The change of piezoresistor was measured by a Wheatstone bridge, and the $(R_1 - R_2)/R_{\mathrm{bridge}}$ is proportional to the actual torque. Only the component of torque perpendicular to sample stage is measured.

When magnetic energy is larger than the anisotropy energy, the amplitude of the torque in the (001) plane saturates and the four-fold magnetic anisotropy, K_{22} can be directly determined from the amplitude of the torque. We measured three samples from the same batch, and the K_{22} value of all three samples is around -150 J/m^3 at 4 K. The magnitude of K_{22} drops quickly as temperature increases and reaches a small value above 150 K. The temperature dependence of magnetic anisotropy for antiferromagnets is the same as that for ferromagnets, following a power law of sublattice magnetization [92][93].

Rather strikingly, torque data for the applied field rotating in the (010)-plane reveal the motion of domain walls. An applied field in the (010) plane of 1 T is sufficient to orient the Néel vector fully perpendicular to the applied field. Domain wall motion occurs even at T = 4 K and, therefore, is not thermally activated.

In the final section, we derive the lowest-frequency, zone-center AFMR frequency for easy-plane AFs, $\omega = |\gamma| \sqrt{2H_E(H_{22} - H_1)}$, where γ is the gyromagnetic ratio, and H_E, H_1, $H_{22}$are the exchange field, out-of-plane anisotropy field and in-plane anisotropy field, respectively. The lower limit on the value of H_1 derived from torque magnetometry data on Fe$_2$As implies a lower limit to the AFMR frequency of f >84 GHz. With K_1 calculated by DFT as K_1 = -830 kJ/m^3 and experimentally measuredK_{22} as -150 J/m^3 , the AFMR frequency is f = 670 GHz at 4 K.

4.2 Methods

Fe_2As crystallizes in the Cu2Sb tetragonal crystal structure. Based on the corresponding magnetic symmetry (mmm1' magnetic point group), the Néel vector of Fe_2As has two degenerate orientations in the (001)-plane [68][52][94].

The Fe_2As crystal was synthesized by mixing Fe and As powders in a 1.95:1 ratio and vacuum sealing inside a quartz tube. The vacuum tube was heated at 1/min up to 600 and held for 6 hours in a furnace. The temperature was then ramped to 975 at 1 $\circ$C/min and held for 1 hour before cooling down slowly to 900 at 1 /min. Finally, the quartz tube was kept at 900 for 1 hour and allowed to cool down to room temperature in the furnace at 10 /min. We obtained a large silver crystal ingot of Fe_2As and it easily detached from the quartz tube. Part of the ingot was crushed into powder for powder XRD characterization and the data showed phase pure Fe_2As. The remaining ingot was then fractured and the fractured surface revealed a smooth facet. Laue diffraction was carried out after polishing this fractured surface. A four-fold symmetry pattern was observed indicating the fractured surface is the (001) plane.

We used a wire saw to cut the sample into smaller pieces for magnetic property characterization and torque measurements. One of the pieces was measured on the superconducting quantum interference device vibrating sample magnetometer (SQUID-VSM, see below), the other three pieces were used in torque magnetometry measurements. We name these three samples measured by torque magnetometry sample A, sample B, sample C and the one for SQUID-VSM sample D.

The temperature-dependent magnetic susceptibility was measured with SQUID-VSM in a Quantum Design Magnetic Properties Measurement System (MPMS). The sample was measured while cooling from 398 K to 4 K in a 10 mT field.

Torque measurements were performed in a Quantum Design Physical Property Measurement System (PPMS). We mounted the sample on a standard torque sensor chip (P109A from Quantum Design with a sensitivity of 1 10^{-9} N·m) as shown in Fig. 4.1. The torque exerted on the torque-lever will change the resistance of two piezoresistor path. This change introduces imbalance to Wheatstone bridge. The imbalance-to-resistance ratio, $(R_1 - R_2)/R_{\text{bridge}}$, is proportional to the actual torque with coefficient called torque coefficient. R_1, R_2 are resistances of two legs of the sample stage. The measured torque compress on of two legs and stench the other one, so that $R_1 - R_2$ can represent the change of torque. During the measurement, the $R_1 - R_2$ value is usually between 1 to 2 Ω. R_{bridge} is the total resistance of the brdige and usually between 600 Ω and 800 Ω.

The specific torque coefficient changes from chip to chip. Thus a calibration process is needed before doing measurement. Without any sample on sample stage, current applied through calibration coil to mimic a magnetic moment. The sample is place at an angle where induced moment is perpendicular to external field, so that cross product, or torque is maximized. The torque coefficient can be derived by comparing imbalance of Wheatston bridge with torque.

The PPMS horizontal sample rotator is used to control the angle between the crystal and the applied field. During the measurement, the external field rotates in either the (010) plane or the (001) plane, while the field-induced moment resides in the same plane as the rotating applied field. We detect the torque component, $m \times B$, that is perpendicular to this plane.

We performed first-principles DFT simulations using the Vienna Ab Initio Simulation Package (VASP) [60][61], to calculate the two-fold anisotropyK_1 and obtain an estimate for the four-fold anisotropy K_{22}. The projector augmented wave (PAW) method[64] is used to describe the electron-ion interaction. Kohn-Sham states are expanded into plane waves up to a kinetic energy cutoff of 600 eV. The Brillouin zone is sampled by a $21 \times 21 \times 7$ Monkhorst-Pack [65] (MP) k-point grid and the total energy is converged self-consistently to within 10^{-9} eV. The local density approximation (LDA) [95] and the generalized-gradient approximation developed by Perdew, Burke, and Ernzerhof (PBE) [63] are used to describe the exchange-correlation energy function, and results from the two different computational strategies are compared.

Achieving the extremely high accuracy for total energies that is required to compute the magnetocrystalline anisotropy on the order of μeV per magnetic unit cell is numerically challenging; the required convergence parameters render it computationally too expensive to perform such calculations fully self-consistently. Instead, we use the convergence parameters quoted above to compute Kohn-Sham states, electron density, and relaxed atomic geometries for collinear magnetism and take non-collinear magnetism and spin-orbit coupling [96] into account without self-consistency of the Hamiltonian, as described in Ref. [97].

4.3 Results and Discussion

4.3.1 Magnetic susceptibility and domain wall motion

We use data for the magnetic susceptibility as input for modeling the torque magnetometry data and to provide insight into the reorientation of antiferromagnetic domains in an external magnetic field. Fig. 4.2a summarizes the results for the magnetic susceptibility in the limit of small field. We fixed the applied field at 10 mT, along the [100] or [001] direction, measured the induced magnetic moment while cooling from T = 400 K, and calculated the susceptibility, $\chi = M/H$, where M is the magnetization. The measured susceptibility is similar to that in a prior report[52].

When the applied field is along an easy axis, we must take domain wall motion into account. We assume

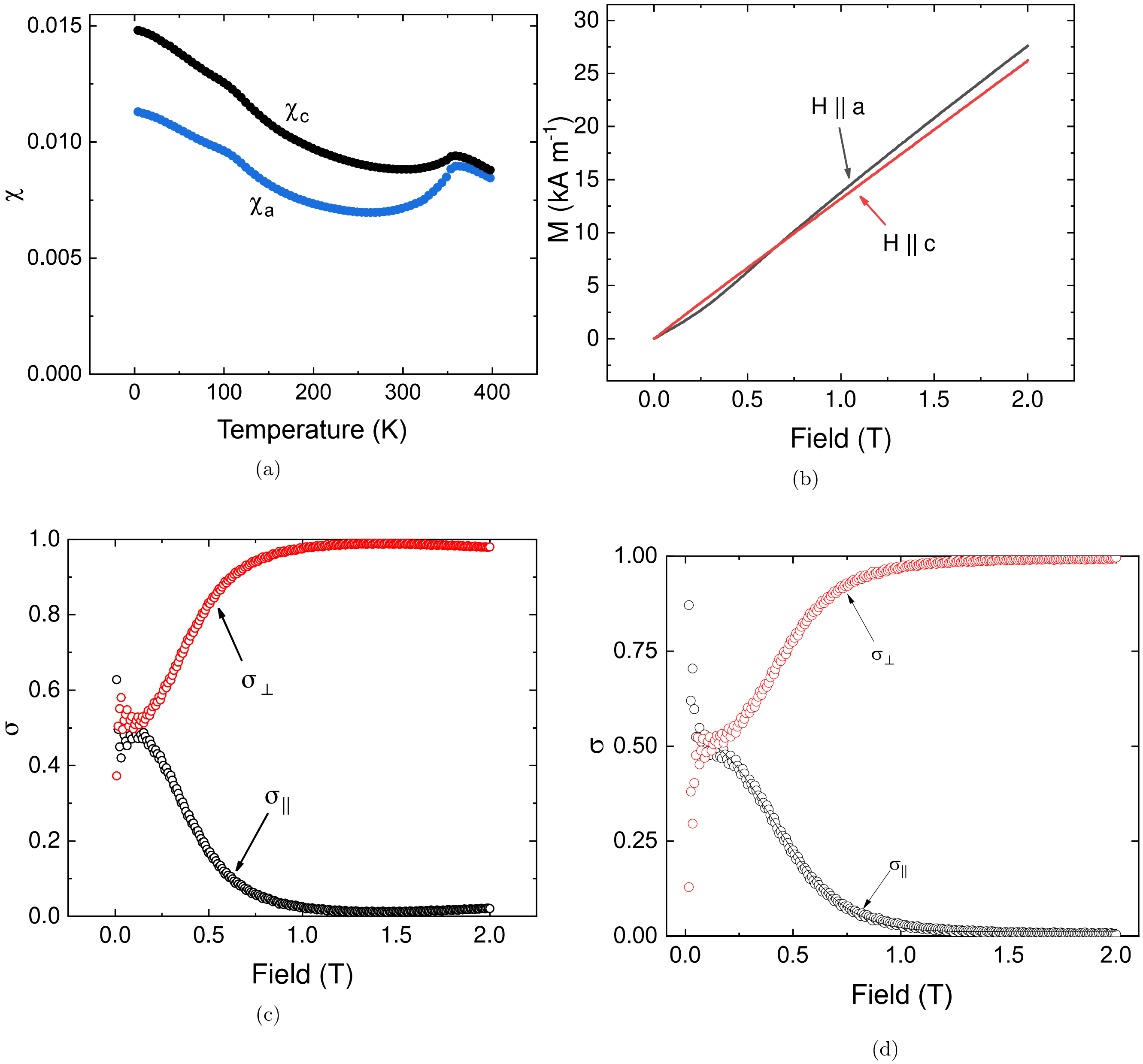

(a)

(b)

(c)

(d)

Figure 4.2: (a) Temperature dependence of the magnetic susceptibility of Fe_2As in the low field limit as measured using 10 mT field applied along the a- and c-axis of the crystal. (b) Dependence of Fe_2As magnetization M on applied field H at T = 4 K. With H along the c-axis, M is a linear function of H. With H along the a-axis, the non-linear dependence of M on H is due to the rotation of antiferromagnetic domains. (c) The population of domains with Néel vectors parallel and perpendicular to the applied field estimated from the dependence of M on H at 4 K and (d) 300 K. The assumptions are: 1) in zero field, the population of domains with Néel vectors in the a and b directions are equal; 2) in the high field limit, the Néel vector is perpendicular to the applied field; and 3) domain wall motion is reversible.

that a 10 mT external field is too weak to significantly affect the domain structure. We further assume that the magnetic moment generated by an applied field along the [100] direction (the a-axis of the crystal) has equal contributions from two types of domains that we label as D1 (Néel vector along [100]) and D2 (Néel vector along [010]) as illustrated in Fig. 4.3. For an applied field in the (001)-plane, we define the susceptibility parallel to the Néel vector as $\chi_{||}$ while that perpendicular to the Néel vector as $\chi'_{\perp}$. On the other hand, the susceptibility for an applied field in the [001] direction is defined as $\chi_{\perp}$. We expect$\chi'_{\perp}$and $\chi_{\perp}$ to be similar but due to the tetragonal symmetry of the crystal structure, $\chi'_{\perp}$and $\chi_{\perp}$ are not necessarily equal. We show below that the difference between $\chi_{\perp}$ and $\chi'_{\perp}$ is less than 5%.

Measurements of the magnetization as a function of field, see Fig. 4.2b, show that χ_c is constant for H applied along the c-axis. For H along the a-axis, $\chi_a$increases with field at low field, and is approximately constant for an applied field > 1 T. We attribute the field dependence of χ_a to domain wall motion and the consequent evolution of the populations of domains with Néel vectors parallel and perpendicular to the applied field.

The populations of the two degenerate domains can be estimated from the M vs H curve in Fig. 4.2a by expressing the field-induced magnetization as $M_a = \sigma_{\perp}\chi'_{\perp}H + \sigma_{||}\chi_{||}H$ and $M_c = \chi_{\perp}H$, where $\sigma_{\perp}$ and $\sigma_{||}$ are the normalized domain fraction perpendicular and parallel to the a-axis, respectively, and $\sigma_{\perp} + \sigma_{||} = 1$. We made three assumptions: (1) $\sigma_{\perp} = \sigma_{||} = 0.5$ at zero field; (2) $\sigma_{\perp} \approx 1$ at high field; and (3) domain wall motion is reversible. The field-dependent distribution of domains parallel and perpendicular to the external field along the a-axis at T = 4 K and T = 300 K are shown in Fig. 4.2c and Fig. 4.2d respectively. For the 4 K data, $\chi_{\perp}$ and $\chi_{||}$ are treated as free parameters; we find $\chi_{||} = 0.008$ and $\chi_{\perp} = 0.018$. For an ideal colinear antiferromagnet, it is expected that $\chi_{||} = 0$ at low temperatures [9, 24]. This is not what we observed in our measurements. The reason is that there is a background susceptibility that we do not yet understand. We assume that the background susceptibility is isotropic. The domain distribution can be fitted phenomenologically with a Gaussian distribution function. The fitted widths of $\sigma_{||}$ at 4 K and 300 K do not have significant difference.

4.4 Torque Magnetometry

The field-induced torque is the cross product of the field-induced magnetic moment and the applied field, $\tau = \mathbf{m} \times \mathbf{B}$. The direction of the induced magnetic moment m is given by the minimum in the total energy:$E_{tot} = E_m + E_{ani} + E_{ex}$, where E_m is the magnetic energy; E_{ani} is the magnetocrystalline anisotropy energy; and E_{ex} is the exchange energy that couples the two sublattices. We refer to the condition $E_m \ll E_{ani}$

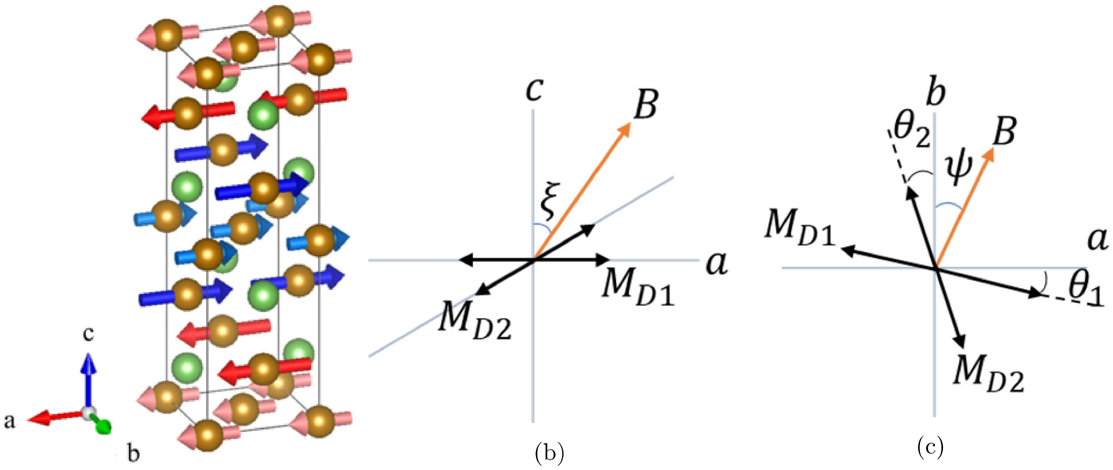

(a)

(b)

(c)

Figure 4.3: Geometry of the torque magnetometry experiments. The a-b-c coordinates are the crystal axes. MD1 and MD2 are the sublattice magnetizations of the two types of domains labeled as D1 and D2. (a) The magnetic unit cell of Fe_2As. (b) Three dimensional perspective of the measurement with the magnetic field rotating in the ac-plane. The magnetic field makes an angle with the c-axis of the crystal. MD1 and MD2 are assumed to stay along the a- and the b-axis, respectively. The torque is along the b-axis. (c) Plan-view of the measurement with the magnetic field rotating in the ab-plane. The magnetic field makes an angle with the b-axis of the crystal. MD1 and MD2 tilt away from a- and b-axis by θ_1 and θ_2, respectively (and are not necessarily the same). The torque is along the c-axis (normal to the plane of the drawing).

as the low field limit and the condition$E_m \geq E_{ani}$ as the intermediate field regime[24]. We ignore a separateE_{ex} term when we analyze the torque data in the (001)-plane because we assume that the exchange interaction stays the same and can be represented by susceptibility. For torque data in the (010) plane, our analysis is based on the anisotropy in the susceptibility, $\chi_\perp - \chi_{||}$, which is also related to the strength of the exchange interaction.

Fig. 4.3a shows the experimental geometry when the applied field is rotating in the (010)-plane. ξ is the angle between the c-axis and the applied field. The induced moments are also in the (010)-plane. Thus, the torque is along the [010] direction. In the low temperature limit, $\chi_{||} = 0$ if the isotropic background is ignored; the induced moment of domain D1 is therefore along [001] and the induced moment of D2 lies in the (010) plane between [001] and [100]. The direction of the induced moment of D2 is determined by $\chi_\perp$ and $\chi'_\perp$.

Fig. 4.3b shows the experimental geometry when the applied field is rotating in the (001)-plane. In this case, because of the relatively small magnetocrystalline anisotropy, the tilt of the sublattice magnetization away from the crystal axes is significant. ψ is the angle between the external field and the crystal axes; θ_1, θ_2 are the angles between the directions of the sublattice magnetization of domains D1, D2 and the crystal axes, respectively (θ_1 and θ_2 are not necessarily equal).

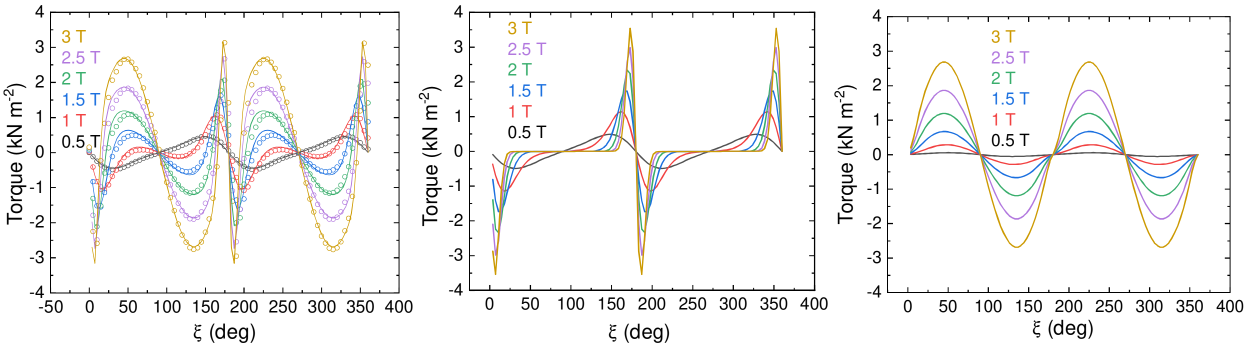

(a) (b) (c)

Figure 4.4: a) Torque magnetometry measurements in the ac-plane of Fe$_2$As at T = 4 K. Open symbols are measured data; solid lines are fits to the data. (b) Calculated torque generated by domains of type D1 as a function of applied field. (c) Calculated torque generated by domains of type D2 as a function of applied field.

Torque magnetometry in the (010)-plane in the low field limit

The torque is zero when the applied field is along the easy or hard axis of a sample, because the induced magnetization is in the same direction as the field. Here, we refer to the easy axis as the lowest energy orientation of the Néel vector, and define orientations of the hard axis as perpendicular to the easy axis. When the applied field is oriented away from an easy or hard axis, the direction of the induced magnetization shifts toward a hard axis because $\chi_{\perp} > \chi_{||}$. In an AF, the slope of the torque as a function of field orientation has opposite signs when the field passes through the orientation of an easy axis and when it passes through the orientation of a hard axis. In our sign convention, torque with a negative slope as a function of angle indicates a hard axis; torque with a positive slope as a function of angle indicates an easy axis. In a single magnetic domain of Fe2As, there are two hard axes: the c-axis perpendicular to the (001) plane and the axis perpendicular to the Néel vector in the (001) plane.

Torque data at 4 K with the field rotating in the (010)-plane are shown in Fig. 4.4a. The slope when the field is along the a-axis ($\xi = 90^\circ$) is positive at B = 0.5 T and changes to negative at B ¿ 0.5 T. Therefore, when the 0.5 T field is oriented along the a-axis, the a-axis is an easy axis but when B is greater than 0.5 T, the a-axis becomes a hard axis. This interpretation is consistent with the analysis of the domain distribution discussed above and displayed in Fig. 1(c). When the applied field along the a-axis is larger than 1 T, the majority of domains are in the D2 configuration and the a axis becomes a hard axis.

The slope of torque data when the applied field is along the c-axis ($\xi = 0^\circ$) is negative because the c-axis is a hard axis. However, when $\xi = 10^\circ$ and B ¿ 0.5 T, the sign of the torque changes abruptly. This dramatic change in the sign of the torque is periodic; the periodicity indicates that domain wall motion is reversible. When the applied field is aligned along the c-axis, the populations of domain D1 and D2 are equal. As the field rotates away from the c-axis, the projection of the applied field in the (001)-plane changes the domain distribution as described by Fig. 1(c). When the field returns to the c-axis, the populations of domain D1 and domain D2 become equal again.

To model the torque data, we first calculate the direction and magnitude of the induced magnetization M by describing the susceptibility as a tensor $M_i = \sum_j \chi_{ij} H_j$[8]. As shown in Fig. 4.3a, there are two degenerate domains with their Néel vectors perpendicular to each other. For domains of type D1, the Néel vector is along the a-axis and the susceptibility tensor is

$$\chi_{D1} = \begin{pmatrix} \chi_{||} & 0 & 0 \\ 0 & \chi'_{\perp} & 0 \\ 0 & 0 & \chi_{\perp} \end{pmatrix} \tag{4.4}$$

For domains of type D2, the Néel vector is along the b-axis and the susceptibility tensor is

$$\chi_{D2} = \begin{pmatrix} \chi'_{\perp} & 0 & 0 \\ 0 & \chi_{||} & 0 \\ 0 & 0 & \chi_{\perp} \end{pmatrix} \tag{4.5}$$

The external field in the (010)-plane is $H = H_0 \begin{pmatrix} \sin(\xi) & 0 & \cos(\xi) \end{pmatrix}^T$, where is the angle between the c-axis and the external field as depicted in Fig. 4.3a. We consider the effect of the projection of the applied field along the a-axis $H_0 \sin\xi$ on the domain distribution as described by the data of Fig. 4.2c. The torque signal of two types of domains are $\tau_{D1}/V = \sigma_{D1}\chi_{D1}H \times B$ and $\tau_{D2}/V = \sigma_{D2}\chi_{D2}H \times B$, while the total torque is the sum $\tau_{D1} + \tau_{D2}$. To evaluate this model, we use the measured magnetic susceptibility as shown in Fig. 4.2. The free parameters are $\chi'_{\perp}/\chi_{\perp}$ and$\chi_{||}$.

Fig. 4.4b and Fig. 4.4c show the calculated values of τ_{D1} and τ_{D2}; the solid lines in Fig. 4.4a are the summation of the two. The good correspondence between the model and the data supports our assertion that domain wall motion is reversible. The difference in the sign of τ_{D1} and τ_{D2} contributes to the abrupt change in the torque signal near an angle of 10. For D1 domains, when the applied field is rotating in the (010)-plane, the induced moment is always close to the c-axis because $\chi_{||}$ is small. For D2 domains, the field-induced magnetization is

$$M = H_0 \begin{pmatrix} \chi'_{\perp} \sin(\xi) & 0 & \chi_{\perp} \cos(\xi) \end{pmatrix}^T . \tag{4.6}$$

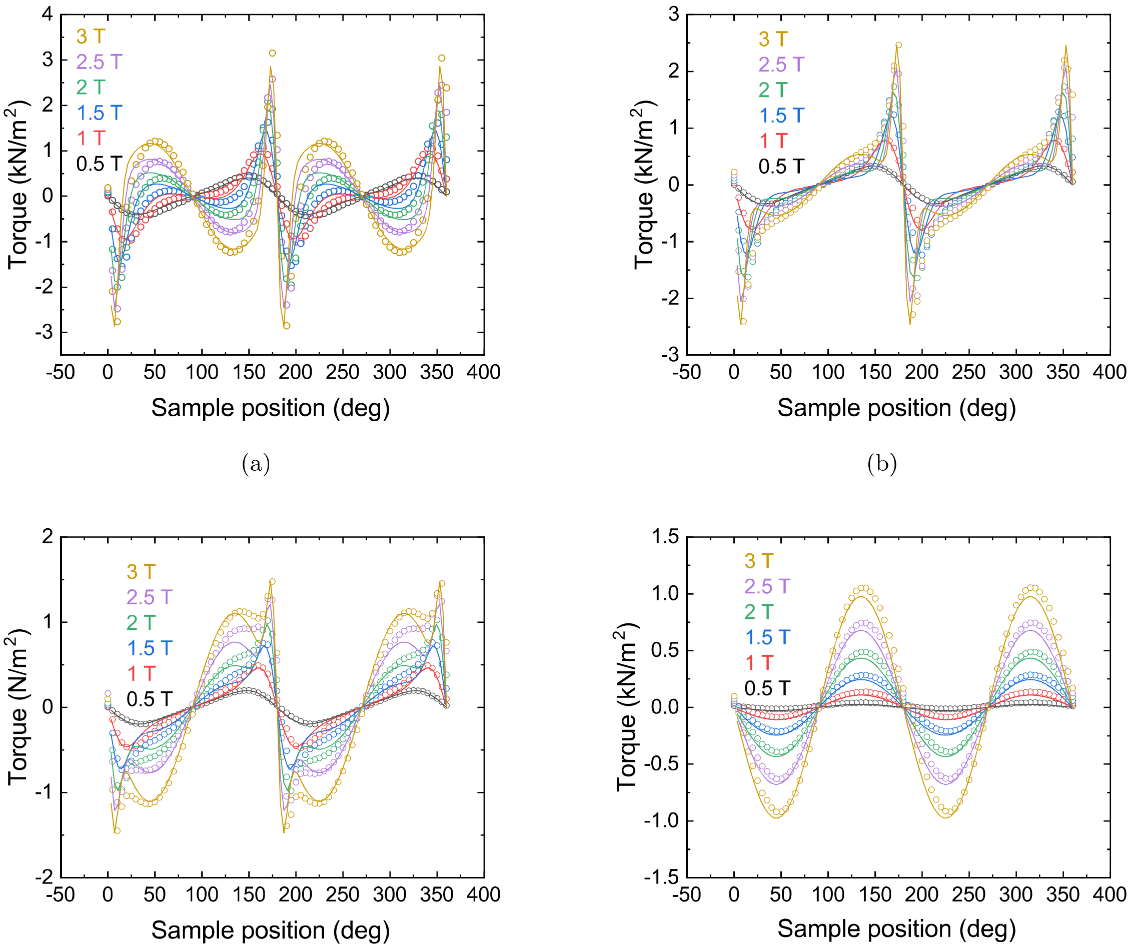

(a) (b)

(c) (d)

Figure 4.5: a) Torque magnetometry measurements in the ac-plane of Fe_2As at (a) 77 K, (b) 200 K, (c) 300 K and (d) 360 K. The open circles are measured data, while the solid line are calculated with model.

If $\chi'_\perp = \chi_\perp$, the induced magnetization $M = \chi_\perp H_0 \begin{pmatrix} \sin(\xi) & 0 & \cos(\xi) \end{pmatrix}^T$, would be parallel to the applied field H. This would infer that there is no torque signal from D2 domains and the total torque signal would be generated only by D1 domains (Fig. 4.4b).

However, the total torque signal we observe is obviously different from what is depicted in Fig. 4.4b (D1 domains only). The torque signal resembles a combination of two domains, hence, we can conclude $\chi'_\perp \neq \chi_\perp$. On the other hand, the dramatic change in the sign of the total torque signal at $\xi = 10°$ and T = 4 K indicates that τ_{D1} and τ_{D2} have opposite signs. Since the induced moment of D1 domains is along the c-axis, the induced moment of D2 domains must be between B and the a-axis.

The torque data at temperature $T > 4$ K were shown in Fig. 4.5. At 360 K, there is no domain movement,

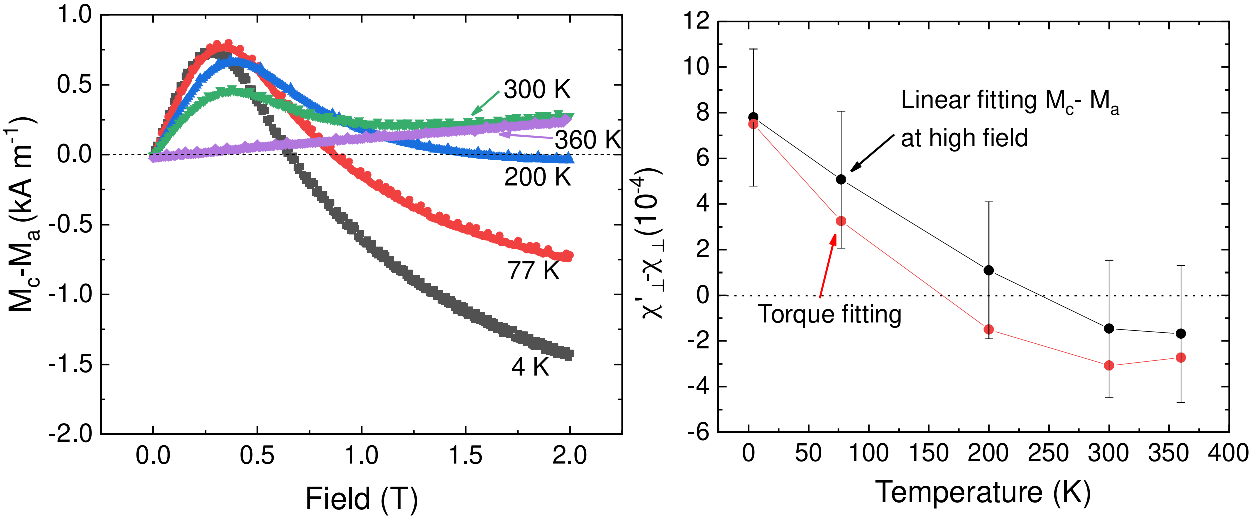

(a)

(b)

Figure 4.6: (a)The field dependent of at different temperatures measured with SQUID-VSM. When the applied field along the a-axis is larger than 1.5 T, all domains can be treated as equivalent to MD2. Therefore, the slope of the data for magnetic fields larger than 1.5 T is . (b) A comparison of the temperature dependent of value from VSM measurements and from fitting the torque data.

the same as we expected because the temperature is higher than Néel temperature. The torque signal comes from anisotropy of crystal and induced magnetic moment in paramagnetic phase. From 77 K and 200 K, the torque signal of domain D2 flipped the sign, because the value of $\chi'_\perp - \chi_\perp$ changes from positive to negative. For torque signal at different temperature, the drastic slop changes of total toque happened at the almost same sample position where $\xi \approx 10^\circ$. This proves The fields needed to trigger the domain wall movement at different temperature are approximately the same.

The difference between $\chi_\perp$ and$\chi'_\perp$ is also observed in the dependence of M on H (Fig. **??**). Figure 4(a) shows the difference between M_c and M_a as a function of applied field and temperature. The bump of $M_c - M_a$ at room temperature and below is due to domain wall motion; the difference at high fields is a result of $\chi_\perp - \chi'_\perp$.

The magnetization of D2 domains in the (010)-plane experiences an anisotropic environment that originates from the difference of the a- and c-axis of the crystal. By fitting the model to the torque data, we determine $\chi'_\perp - \chi_\perp$ as a function of temperature (Fig. 4.6b). We observe a change in sign of $\chi_\perp - \chi'_\perp$ near 200 K that is consistent with the anisotropy in the dependence of M on H (Fig. 4.6a). This change in sign indicates that the field-induced magnetization of D2 domains is between the applied magnetic field and the a-axis below 200 K, and between the applied magnetic field and the c-axis above 200 K. The anisotropy in the perpendicular susceptibility, $\chi_\perp - \chi'_\perp$, is always small compared to its absolute value: $|\chi_\perp - \chi'{}_\perp|/\chi_\perp \leq 0.05$.

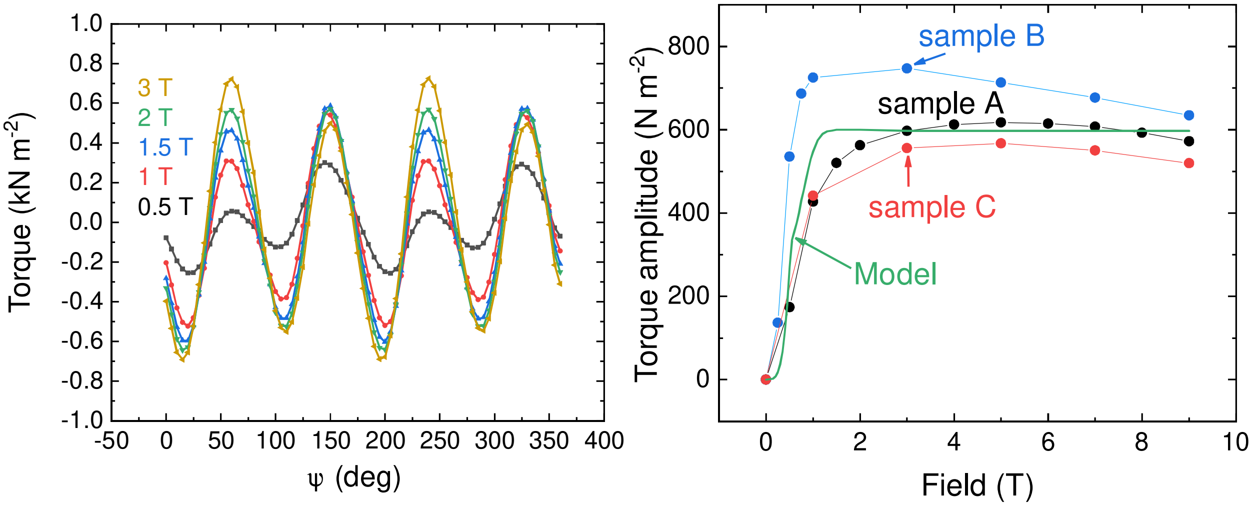

(a)

(b)

Figure 4.7: a) Torque magnetometry measurements of Fe_2As (sample A) in the ab-plane at 4 K. (b) The four-fold symmetry amplitude extracted from torque measurements at 4 K and from the model. When torque amplitude is saturated, the in-plane anisotropy can be derived with $\tau_0 \approx 4K_{22}$

Torque magnetometry in the (001)-plane under intermediate field

Figure 5(a) shows torque data acquired with the applied field rotating in the (001) plane. As expected, the data show four-fold symmetry. We attribute the small two-fold symmetry to a background that comes from misalignment of the sample. (The c-axis is not precisely perpendicular to the field direction.) The amplitude of the four-fold contribution to the torque as a function of applied field of three samples from the same batch is plotted in Fig. 4.7b. To quantify the magnetic anisotropy in the (001)-plane of Fe2As, we analyze the torque data by minimizing the total energy for D1 domains and D2 domains, respectively, then add τ_{D1} and τ_{D2} together to compare it to the data. WhenE_m is comparable to or larger than E_{ani} ($E_m \geq E_{ani}^{(001)}$), Néel vectors start tilting away from crystal axes as shown in Fig. 4.3b. We assume that the two sublattice magnetizations are approximately parallel to each other, so the exchange interaction is considered in magnetic energy. With the applied field rotating in the (001)-plane of Fe2As, the total energy is

$$E_{tot}/V = -\frac{1}{2}H(\psi)\chi_{tot}(\psi,\theta)H^T(\psi) + K_{22}\cos(4\theta) + K_1 + K_2 \tag{4.7}$$

where $\chi_{tot} = \sigma_{D1}\chi_{D1}$, $\theta = \theta_1$ for D1 domains and $\chi_{tot} = \sigma_{D2}\chi_{D2}$, $\theta = \theta_2$ for D2 domains.

To obtain an accurate value of E_m, we rotate the susceptibility tensor together with the Néel vector $\chi^R(\theta) = R(\theta)\chi R^T(\theta)$[89], where θ is the angle between the Néel vector and the crystal axis, and $R(\theta)$ is the rotation matrix:

$$R(\theta) = \begin{pmatrix} \cos(\theta) & -\sin(\theta) & 0 \\ \sin(\theta) & \cos(\theta) & 0 \\ 0 & 0 & 1 \end{pmatrix} \tag{4.8}$$

During the rotation, the field component along M_{D1} and M_{D2} result in a change in the populations of D1 and D2 domains. Thus, σ_{D1} and σ_{D2} are determined by the angle between the applied field and the spin axis, $(\theta + \psi)$.

The analogous behavior of a uniaxial antiferromagnet (AF) [10] provides a point of comparison. In a uniaxial AF, the critical field for the spin-flop transition is $H_c = \sqrt{2(K_1 + K_2)/(\chi_\perp - \chi_{||})}$. For Fe2As, as shown in Fig. 4.2c and Fig. 4.7b, we do not observe a sudden change in the domain populations that would be characteristic of a spin-flop transition. Furthermore, in a perfect crystal that is free from disorder, the single domain structure created by an applied field would persist after the field is removed. (In ferromagnets, domains form to reduce the contribution of the magnetic energy of stray fields to the total energy. In AFs, this driving force for domain formation is absent.) We attribute gradual and reversible domain movement in Fe_2As to random strain fields created by static disorder in the crystal that create local variations in the anisotropy energy.

The midpoint of the change in the populations of the D1 and D2 domains as a function of field is, however, close to what is expected for the characteristic field of a spin-flop transition of an ideal single domain easy plane antiferromagnetic crystal. The total energy of D2 when $\xi = 90°$ is [89]

$$\frac{E_{tot}}{V} = K_1 + K_2 + K_{22}\cos(4\theta_2) + \frac{1}{2}(\chi_\perp - \chi_{||})H^2\cos^2(\psi + \theta_2) - \frac{1}{2}\chi_\perp H^2 \tag{4.9}$$

Both anisotropy and magnetic energy are function of θ_2 but with different periodicity. When $H < H_c$, the $E_{tot}(\theta = 0°)$ is at a local minimum; when $H > H_c$, the $E_{tot}(\theta = 0°)$ should be at global maximal so that spins are aligning along global energy minimum $\theta = 90°$. The characteristic field H_c is when $E_{tot}(\theta = 0°)$ just equal to maximal energy. One can take derivative $\frac{\partial E}{\partial \theta}$ to get theta value when E is maximal, and let $\theta = 0$ to derive H_c. The critical field we got is $\mu_0 H_c = \sqrt{16\,|K_{22}|/(\chi_\perp - \chi_{||})} = 560\text{mT}$ with the measurement of $K_{22} = -150\text{J/m}^3$ is described below.

The domains begin to move in a field smaller than H_c because at some locations the energy barrier is smaller. The domain wall motion is not complete until fields larger than H_c because in some areas, local K_{22} is larger so a higher field is required to switch the domains. When the external field is removed, the random strain field dominates the domain distribution again and the volume fraction of domains is reversed

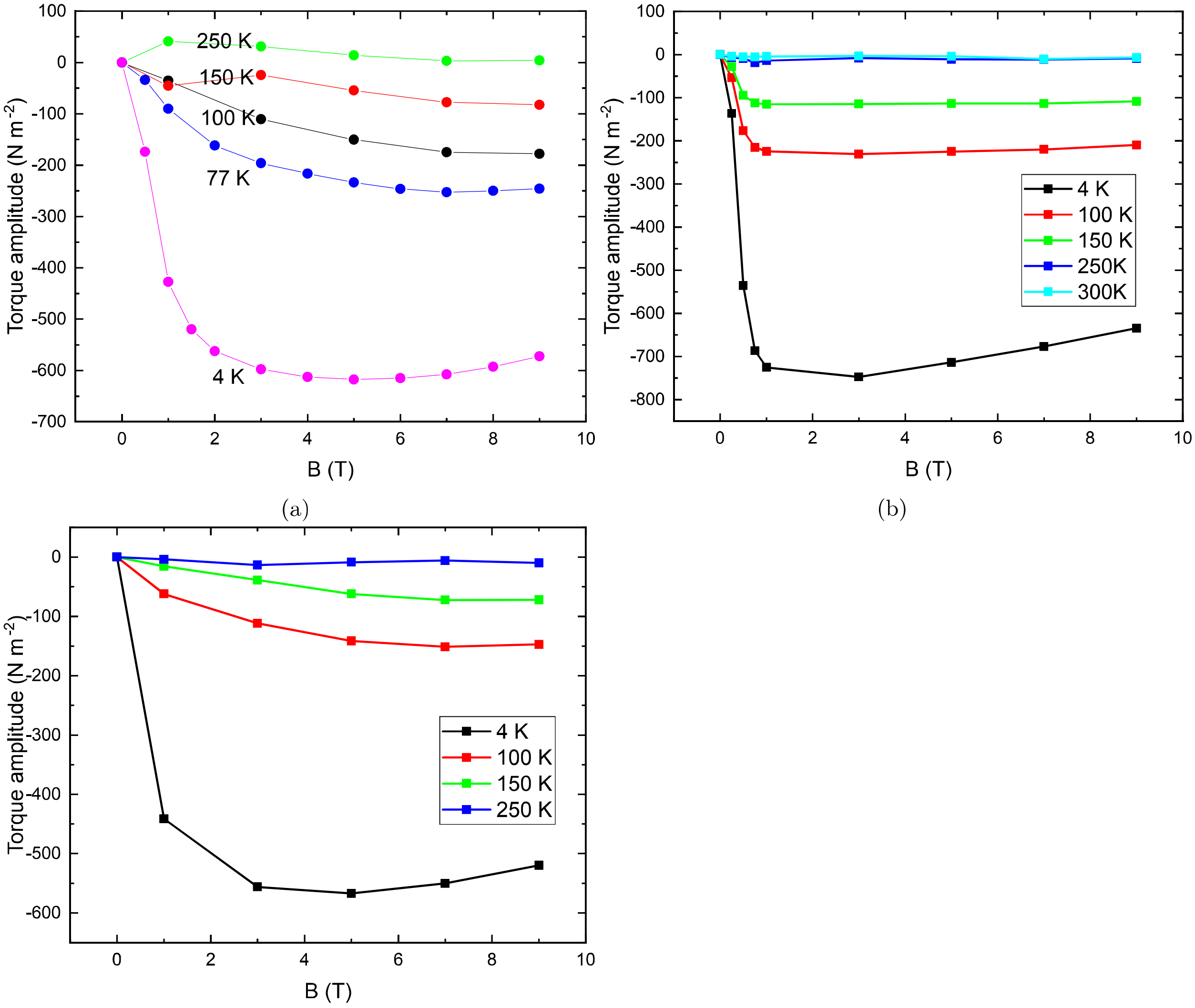

(a) (b) (c)

Figure 4.8: Field-dependent of four-fold torque amplitude in the Fe_2As (001) plane measured at different temperatures. Data collected on three samples from the same batch: (a) sample A, (b) sample B, and (c) sample C.

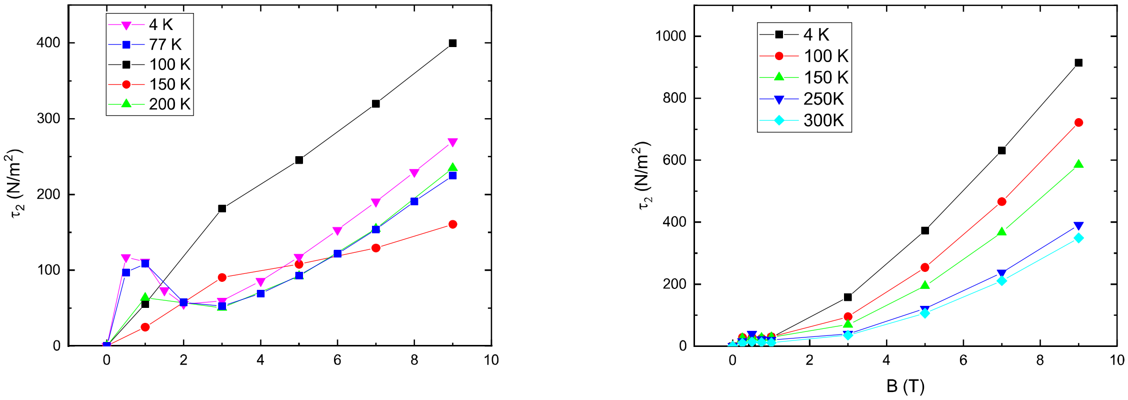

(a) (b)

Figure 4.9: The field-dependence of two fold symmetry amplitude in the Fe_2As (001) plane measured at different temperatures. (a) sample A and (b) sample B. The two-fold signal could come from the miscut of sample.

[91].

The torque induced by the applied field is the derivative of the total energy $\tau = dE_{tot}/d\psi$. In the intermediate field regime, i.e., $E_m \geq E_{ani}$ or $H \geq H_c$, it is reasonable to assume that the sample is a single domain and the sublattice magnetization is always nearly perpendicular to the applied field, i.e., $\theta+\psi \approx \pi/2$. The "intermediate field" regime refers to an applied field larger than the critical field, but not large enough to significantly change the exchange interaction. One important assumption here is that the tilt of two sublattice magnetizations in the external field is small enough to be neglected. With this approximation, the magnetic energy is nearly independent of θ and ψ, $E_m \approx -\frac{1}{2}\chi_\perp H_0^2$. Then, the torque can be easily related to the anisotropy: $\tau = \frac{dE_{tot}}{d\psi} \approx \frac{dE_{ani}}{d\psi} = -4K_{22}\sin(4\psi)$, where τ no longer depends on the magnitude of the applied field.

A graduation reorientation of domains of an easy-plane antiferromagnet as a function of applied field was also recently observed in 50 nm thick CuMnAs epitaxial layers grown on GaP [4]. (CuMnAs and Fe_2As have essentially the same crystal structure with Cu and Mn atoms in CuMnAs occupying the same lattice sites as the two crystallographically distinct Fe atoms in Fe2As.) The strength of the field needed to reorient antiferromagnetic domains in CuMnAs epitaxial layers is similar to what we observe in Fe_2As bulk crystals. Thinner, 10 nm thick, CuMnAs layers show a pronounced in-plane uniaxial anisotropy and a more abrupt transition in domain structure as a function of field than 50 nm thick layers. X-ray magnetic linear dichroism (XMLD) measurements of CuMnAs epitaxial layers reveals that the domain reorientation is not fully reversible and hysteresis for fields less than 2 T. X-ray photoelectron microscopy (XPEEM) images acquired after applying 7 T fields in orthogonal directions also show that the domain structure does not revert back to a fixed configuration in zero field.

We fit raw data with a summation of two-fold and four-fold symmetry:

$$\tau = \tau_2 \sin 2\psi + \tau_4 \sin 4\psi \tag{4.10}$$

where τ_4 is related to in-plane anisotropy, and τ_2 is from miscut of the sample. Fig. 4.8 shows field dependent τ_4 value for three samples at different temperature. For field much smaller than H_c, we expect the τ_4 is quadratic to the external field, because anisotropy energy dominates the total energy and magnetic energy dominates the $\frac{dE_{tot}}{d\psi}$, as well as the torque value. We did not observe τ_4 is quadratic to field, becuase the domains starts rotating as small as 0.5 T, and the torque value at field smaller than 0.5 T would be too small to measure.

The fitted field-dependent τ_2 values of sample A and sample B were plotted in Fig. 4.9. In Fig. 4.9b, the τ_2 value is quadratic to external field. We attributed this to miscut of the sample. If the miscut is along a-axis or b-axis, the out-of-plane anisotropy K_1 will project on the plane we measured. Because of the large value of K_1, even though the projection of K_1 on the surface we measured is still larger than magnetic energy and satisfied $H \gg H_c$.

Based on our observation in Fig. 4.7b, as field increases, τ increases quickly then saturates. At higher fields, τ is slightly smaller than the saturation value, rather than staying the same until 9 T. At higher fields, the tilting of spins caused by the external field cannot be neglected, so exchange interaction is no longer a constant. In our model, however, the torque stays the same after saturation based on our assumption of constant susceptibility and exchange interaction. But the assumption is no longer valid in higher field. While induced magnetization is smaller than χH, the torque is smaller than the saturation value, too.

As our model predicts, the experimentally measured torque amplitude saturates as the applied field approaches 1 T for sample sample B, and 3 T for samples sample A and sample C. Hence, it is safe to select 1 T and 3 T as the "intermediate field" regime for sample B and sample A(sample C), respectively. The measured K_{22} value of sample A is $-150\mathrm{J/m}^3$. The field-dependence of K_{22} in all three samples follow precisely the same trend, however, individual data points do not overlap perfectly. We attribute this discrepancy to the non-uniformity of the sample.

With a temperature-dependent measurement of torque in the ab-plane at an intermediate field, we can obtain the temperature-dependence of K_{22} for the samples as shown in Fig. 4.10. The overall temperature dependence is the same for all three samples despite some minor differences in the detail. As temperature increases, the magnitude of K_{22} decreases and becomes close to zero at T > 150 K. K_{22} of sample A even

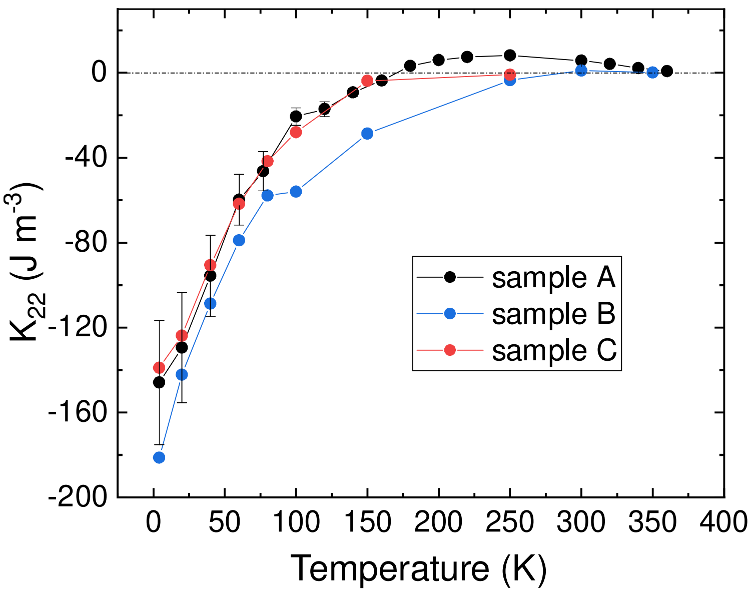

Figure 4.10: The temperature dependence of K_{22} of Fe$_2$As. The torque data with the external field rotating in the (001) plane were measured with an intermediate field strength (3 T for sample A and sample C, and 1 T for sample B) and the amplitude of the four-fold symmetry was extracted to obtain the in-plane anisotropy with $\tau_0 \approx 4K_{22}$. Intermediate field is defined as a field strength under which the torque amplitude of four-fold symmetry saturates at 4 K. There is 20% uncertainty of determining saturation value of torque amplitude.

becomes marginally positive for temperatures > 150 K. From Eq. (2), the total energy reaches a minimum when the Néel vector is along the crystal a- and b-axis ($\theta = 0°$or $\pm 90°$) for $K_{22} < 0$ at zero field. When $K_{22} > 0$, the Néel vector lies in directions with $\theta = \pm 45°$ to minimize the anisotropy energy [89].

First-principles calculations of magnetocrystalline anisotropy

Magnetocrystalline anisotropy of Fe$_2$As has two contributions, one from spin-orbit interaction (SOI) and one from classical magnetic dipole-dipole interaction (MDD): anisotropy from SOI is calculated using DFT for noncollinear magnetism with spin-orbit coupling, by rotating the Néel vector within the easy plane (001) and out of plane towards the hard axis (010). The corresponding total-energy changes are visualized in Fig. S2 and the anisotropy energies are then obtained by fitting the energy change vs. Néel vector orientation to Eq. (2). This leads to a two-fold symmetric SOI anisotropy energy for the Néel vector in the (010) plane and a four-fold symmetric one for the (001) plane. In DFT-PBE, the corresponding values are K_1=534 kJ/m^3 for the (010) plane and K_{22}= 277 J/m^3 for the (001) plane. In DFT-LDA, the (010) plane anisotropy energy is K_1= 315 kJ/m^3 and K_{22}= -292 J/m^3 for the (001) plane. Non-zero K_{22} indicates the existence of two local energy minima. The sign of K_{22} differing between DFT-LDA and DFT-PBE implies that the energetic ordering of these two minima is inverted. Negative K_{22} means that the energy minimum occurs for a Néel vector along a [100] equivalent direction and positive K_{22} for a Néel vector along a ¡110¿ equivalent

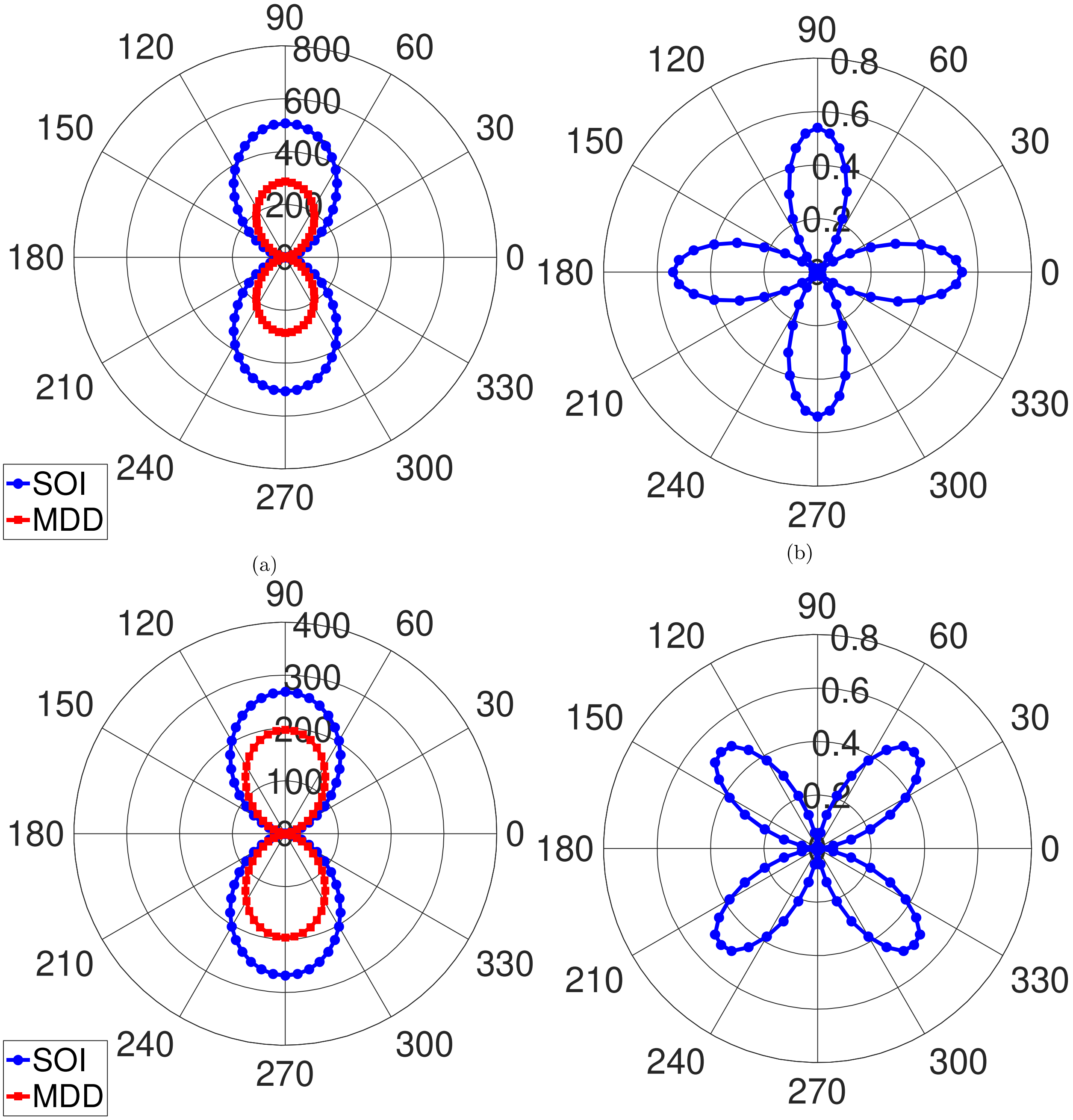

(a)

(b)

(c)

(d)

Figure 4.11: Anisotropy energy contributions (unit: μeV per magnetic unit cell) due to spin-orbit interaction (SOI) and magnetic dipole-dipole interaction (MDD) for Néel vector in the (010) plane (panels (a) and (c)) and in the (001) plane (panels (b) and (d)). Anisotropy energy from MDD in the (001) plane is very small. Zero degree corresponds to the [100] crystallographic axis, and 90 degree corresponds to the [001] axis in (a, c) and [010] axis in (b, d), respectively.

direction.

The MDD contribution is computed using a classical model that is parametrized using the chemical and magnetic ground-state structure from DFT. We use the ground-state chemical and magnetic structure from DFT-LDA as well as DFT-PBE, to evaluate the following expression for the classical magnetic dipole-dipole interaction and to compare the influence of exchange and correlation:

$$E_d = -\frac{1}{2}\frac{\mu_0}{4\pi}\sum_{i\neq j}\frac{3\left[m(r_i)\cdot r_{ij}\right]\left[m(r_i)\cdot r_{ij}\right] - m(r_i)\cdot m(r_j) r_{ij}^2}{r_{ij}^5} \tag{4.11}$$

In order to obtain the anisotropy energy for bulk Fe_2As from this expression, we use an interaction shell boundary r_{ij} of 180 Å, which converges the result to within 10^{-7} eV. This leads to a two-fold symmetric MDD contribution to the anisotropy energy in the (010) plane of K_1= 223 kJ/m^3 and K_1= 296 kJ/m^3 in LDA and PBE, respectively. The MDD contribution in the (001) plane is less than 1 neV and, thus, negligible.

In summary, we find a total out-of-plane anisotropy energy of -539 kJ/m^3 and -830 kJ/m^3 from LDA and PBE, respectively. We attribute 2/3 of the total out-of-plane anisotropy energy to the SOI contribution and 1/3 to the MDD contribution. Both terms show two-fold symmetry with the hard axis along the [001] direction. Torque magnetometry can only measure a lower bound for the out-of-plane anisotropy energy, which is K_1 >36 kJ/m^3 and does not contradict our DFT results.

The in-plane anisotropy energy is computed as K_{22}= 276.5 J/m^3 (DFT-PBE) and K_{22}= -292 J/m^3 (DFT-LDA), while the measured result is K_{22} = -150 J/m^3. A negative sign of the measured K_{22} implies an easy axis for the Néel vector along the [100] direction. In contrary, the positive sign found in DFT-PBE implies preferential alignment along the ¡110¿ direction. Four-fold symmetry is found for these contributions in the (001) plane both in experiment and in DFT calculations.

Antiferromagnetic resonance of easy plane antiferromagnets

Without anisotropy, the magnon dispersion of energy in antiferromagnet is zero at the center of the Brillouin zone. The existence of anisotropy introduces a band gap at the zone center. The antiferromagnetic resonance (AFMR) mode we refer to in this work describes this precessional magnetization motion at the zone center. With the anisotropy values, we can make an estimation of the AFMR frequency.

We start from equations of motion under the 'macrospin' approximation of the two magnetic sublattices

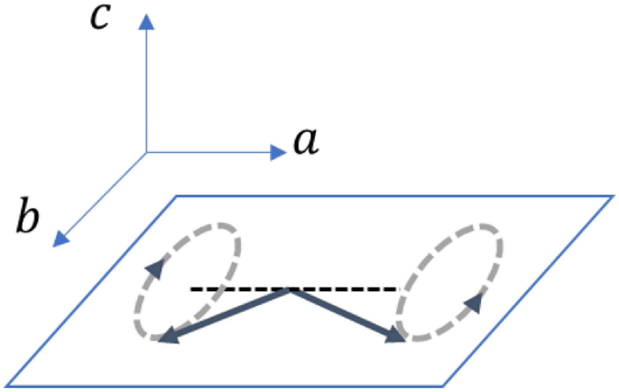

Figure 4.12: The zone center antiferromagnetic resnance (AFMR) mode. While spins along a-axis start oscillation, there is no net magnetization along c-axis or b-axis. But there will be net magnetization along b-axis.

in domain D1 [98][99]:

$$\begin{aligned}\frac{dM_1}{dT} &= |\gamma|\, M_1 \times \left[(H_{22}+H_{ex})\hat{i} + \left(-\lambda M_2^b + \frac{M_1^b}{M}H_{22}\right)\hat{j} + \left(-\lambda M_2^c + \frac{M_1^c}{M}H_1\right)\hat{k}\right] \\ \frac{dM_2}{dT} &= |\gamma|\, M_2 \times \left[(-H_{22}-H_{ex})\hat{i} + \left(-\lambda M_1^b + \frac{M_2^b}{M}H_{22}\right)\hat{j} + \left(-\lambda M_1^c + \frac{M_2^c}{M}H_1\right)\hat{k}\right]\end{aligned} \tag{4.12}$$

Where γ is the gyromagnetic ratio, M_1 and M_2 are sublattice magnetizations of domain D1, H_1 and H_{22} are out-of-plane and in-plane anisotropy fields, respectively, which can be written as K_1/M and K_{22}/M. $H_{ex} = \lambda M$ and λ is the inter-sublattice exchange interaction. $M_1^a = -M_2^a \approx M$, M^b and M^c are magnetization components along the b- and the c-axis when spin processes, respectively.

Expand the Eq. 4.12 along x-direction.

$$\begin{aligned}\frac{dM_1^a}{dt} &= \gamma\left(\frac{M_1^b M_1^c}{M}H_1 - \frac{M_1^b M_1^c}{M}H_{22}\right) \\ \frac{dM_2^a}{dt} &= \gamma\left(-\frac{M_2^b M_2^c}{M}H_1 + \frac{M_2^b M_2^c}{M}H_{22}\right)\end{aligned} \tag{4.13}$$

Because $M_1^b M_1^c$ and $M_2^b M_2^c$ are very small, $\frac{dM_1^a}{dt}$ and $\frac{dM_1^a}{dt}$ are approximately zero.

Then expand Eq. 4.12 along y-axis and z-axis and let $M_1^a = -M_2^a = M$:

$$\frac{dM_1^b}{dt} = |\gamma|(M_1^c(H_{22}+H_E) - H_1 M_1^c + \lambda M M_2^c) \tag{4.14a}$$

$$\frac{dM_1^c}{dt} = |\gamma|(-H_E M_1^b - \lambda M M_2^b) \tag{4.14b}$$

$$\frac{dM_2^b}{dt} = |\gamma|(-M_2^c(H_{22}+H_E) + H_1 M_2^c - \lambda M M_1^c) \tag{4.14c}$$

$$\frac{dM_2^c}{dt} = |\gamma|(H_E M_2^b + \lambda M M_1^b) \tag{4.14d}$$

Take $H_E = \lambda M$ into Eq. 4.14b and Eq. 4.14d, Eq. 4.14b and Eq. 4.14d become

$$\begin{aligned}\frac{dM_1^c}{dt} &= -|\gamma| H_E (M_1^b - M_2^b)\\ \frac{dM_2^c}{dt} &= |\gamma| H_E (M_1^b + M_2^b)\end{aligned} \tag{4.15}$$

The only difference of the Eq. 4.15 in the right hand side is a negative sign, it means $\frac{dM_1^c}{dt} = -\frac{dM_2^c}{dt}$. Meanwhile, Eq. 4.15 requests M_1^b and M_2^b in the same sign to ensure $\frac{dM_1^c}{dt}$ and $\frac{dM_2^c}{dt}$ are not zero.

Add time evolution to M_1^b, M_2^b, M_1^c and M_2^c:

$$\begin{aligned}M_1^b &= M_2^b = M^y e^{i\omega t}\\ M_1^c &= M^z e^{i(\omega t + \frac{\pi}{2})} = iM^z e^{i\omega t}\\ M_2^c &= M^z e^{i(\omega t - \frac{\pi}{2})} = -iM^z e^{i\omega t}\end{aligned} \tag{4.16}$$

Eq. 4.14 reduce from four equations to two equations:

$$\begin{aligned}\omega M^y &= |\gamma| M^z (H_{22} - H_1)\\ \omega M^z &= 2|\gamma| H_E M^y\end{aligned} \tag{4.17}$$

With negative value discarded, the angular frequency is $\omega = |\gamma|\sqrt{2H_E(H_{22} - H_1)}$. Another eigenvalue of Eq. 4.14 is $\omega = 0$.

Because the two sublattices along the a-axis are aligned antiparallel to each other, the anisotropy fields along a-axis are of opposite signs. Along the b- and c-axes, the sign of the effective aniostropy field is determined by the signs of $M_{1,2}^b$ and $M_{1,2}^c$. In domain D1, although the sublattice magnetizations stay along the a-axis, the in-plane anisotropy is of four-fold symmetry, so there is equivalent anisotropy along the a- and b-axes. The effective anisotropy fields along the a- and b-axes are determined by the projection of magnetization on these axes. The only non-zero solution of the equation of motion requires $M_1^b = M_2^b$ and $M_1^c = -M_2^c$, as shown in Fig. S2. The corresponding angular frequency can be expressed as $\omega = |\gamma|\sqrt{2H_{ex}(H_{22} - H_1)}$.

In easy-plane AFs, $K_1 < 0$ and its absolute value is usually much larger than K_{22}, thus the frequency is always real. Besides, the AFMR frequency is smaller with smaller $H_{22} - H_1$ value, because the system is more isotropic. For easy-plane materials with $|K_{22}| - |K_1| \ll 0$, the AFMR frequency is dominated by the anisotropy out of the easy plane.

Our torque measurement with field rotating in the (010)-plane of Fe_2As is in the low field limit, which means the critical field in the (010)-plane must be larger than 3 T. With $H > H_c = \sqrt{\frac{2|K_1|}{\chi_\perp - \chi_\parallel}}$, we can calculate a lower bound of $|K_1|$, which is 36 kJ/m^3. For the exchange field, we use sublattice magnetization $M_{D1} = 4 \times 10^5$A/m and an exchange integral $\lambda \approx 1/\chi_\perp$. We obtain an exchange field $H_{ex} \approx 50$T, and an anisotropy field $H_1 > 0.09$ T. Therefore, the lower bound of the AFMR frequency of Fe$_2$As is 84 GHz. The K_1 value calculated with DFT-PBE can provide us with a better estimation of the AFMR frequency. With calculated K$_1$= -830 kJ/m^3, the AFMR frequency is f = 670 GHz. For tetragonal antiferromagnets like Fe2As, the AFMR is dominated by K_1 and is still high because $|K_1| \gg |K_{22}|$. The same relation is also valid for Mn2Au where a previous calculation [30] shows that the magnitude of the out-of-plane anisotropy is also much larger than the in-plane anisotropy. It is important to determine both K_1 and K_{22} value if one wants to estimate AFMR frequency as well as the thermal stability of spintronics materials.

As discussed in Refs. [2] and [100], the electrical current can only switch a very small number of antiferromagnetic domains. As the anisotropy energy scales with sample volume, the total in-plane anisotropy energy is determined by the volumetric difference of the two kinds of domains, $\Delta E = (V_{D1} - V_{D2})K_{22}$. $V_{D1} - V_{D2}$depends on temperature, current density and the pulse width [101]. If the attempt frequency is not high enough and $V_{D1} - V_{D2}$ is small, the magnetic state is more susceptible to thermal fluctuations.

4.5 Conclusion

We performed torque magnetometry measurements on an easy-plane antiferromagnet Fe2As. The measurement results prove that the domain wall motion in the single-crystalline sample is reversible, and allow us to extract the in-plane anisotropy when the magnetic energy E_m is comparable to magnetocrystalline anisotropy energyE_{ani}. The in-plane anisotropy of Fe$_2$As is K_{22} = -150 J/m^3 at 4 K. $K_{22}$is strongly temperature-dependent and its magnitude decreases as a function of temperature. This means that the domain structure in Fe$_2$As may be easily perturbed by a small applied field at room temperature. With K_1=-830 kJ/m^3 calculated from DFT, we derived the AFMR frequency $f = \frac{|\gamma|}{2\pi}\sqrt{2H_{ex}(H_{22} - H_1)} = 670$ GHz. Our analysis of torque magnetometry data suggests that the in-plane magnetic anisotropy of some candidate materials for antiferromagnetic spintronic applications, such as Fe2As, can be very small at room temperature. A field smaller than 1 T is sufficient to significantly alter its domain structure. The measurement of K_{22} in Fe$_2$As provides a baseline value for further studies of magnetic anisotropy of easy-plane antiferromagnets and the motion of antiferromagnetic domain walls.

Chapter 5

Polarization Modulation Microscopy to Image Magnetic Materials

5.1 Introduction

5.1.1 The Motivations of Imaging of Magnetic Domains in Antiferromagnetic Spintronics

In cases of easy-plane antiferromagnetic materials, it was found that current-induced spin-orbit torque can change the orientation of the Néel vector in the easy plane. This was indeed recently demonstrated with metallic antiferromagnets CuMnAs[5], Mn_2Au[102] and antiferromagnetic insulator/platinum bilayers [7][8]. However, in the electrical switching experiments the necessary current densities are close to the damage limit and further materials optimization is required, specifically aimed at a reduced domain wall pinning. To this end, characterization of antiferromagnetic domain structure is of major importance.

To understand these materials and the underlying spin-orbit torque needed for future devices, we need to visualize the magnetic domain configuration. Moreover, field-dependent magnetic domain imaging can help to determine key magnetic properties, e.g., the spin-flip field. When the magnetic field is larger than spin-flip field, the domain structure will dramatically change. As the spin-flip field is determined by the susceptibility and magnetic anisotropy, observations of domain structure and spin flip are helpful in characterizing magnetic anisotropy.

In reference [31], images of domain switching of CuMnAs film show that only a small fraction of domains are switched by electrical currents. The effectiveness of switching of CuMnAs is much smaller compared to the images of ferromagnetic spintronics switching[103]. On the contrary, mapping of domains in Ref. [8] shows effective domain switching driven by electrical currents.

As described in the last chapter, magnetic materials like Fe_2As have domain structures that can be manipulated by external fields. An external field achievable with an electromagnet (~ 1 T) can significantly switch the magnetic domains at room temperature. As we observed with vibrating sample magnetometry, the domain population returned to the initial configuration when the external field was removed, even though a multi-domain structure is energetically unfavourable. The in-plane magnetic anisotropy is the energy barrier that separate two degenerated magnetic domain orientations. The sample should remain in a single domain configuration at zero field after the application of an external field flips all domains towards one of the easy axes. We attributed the reversible distribution to random strains from local defects in the sample that locally introduces a preference of one of the easy axes.

The image of magnetic domains with external field applied can help us understand the reason for the reversibility of the domain distribution. Since the Néel vector can be reorientated by an external field, the field-dependent magnetic optical birefringence can be studied if the signal is larger than the noise.

5.1.2 Optical Geometry in Magneto-optical Effects

Changes in the polarization of light are often used to detect the magnetization of materials.

With X-rays as the source, one can study magnetic domains with scanning X-ray microscopy and X-ray photo-emission electron microscopy (PEEM). These methods use absorption contrast produced by magnetic linear dichroism (XMLD) to probe antiferormangetic domains or magnetic circular dichorism (XMCD) to probe ferromagnetic domains.

Similarly, circularly and linearly polarized laser sources can probe magnetism. Compared to non-magnetic materials, the alignment of spins in magnetic materials breaks rotational symmetry. Optical detection of symmetry breaking of magnetic materials is known as magneto-optical (MO) effects. MO effects come from contributions of magnetism to the dielectric constant as shown in Eq. 1.3. The optical geometry to measure first-and second-order magnetization with perpendicular incident light are depicted in Fig. 5.1.

When the magnetization is out-of-plane, the magnetization breaks rotational symmetry, which means the sample is different when it is rotated by 180° around y-axis or x-axis. This symmetry breaking makes what left and right circularly polarized (LCP and RCP) light see different, so there will be an amplitude and phase change when circularly polarized light is reflected back from the sample. When incident light is perpendicular to the sample surface, we call this measurement configuration polar MOKE. Similarly, in-plane magnetization changes the amplitude and phase of linearly polarized light. This is because the in-plane magnetization makes sample different for linearly polarized light when sample is rotated by 90° around z-axis.

There are several key elements for successfully imaging of magnetic domains. For the sample itself, there needs to be sufficient contrast signal for different domains. For polar MOKE measurement of ferromagnetic samples, the MOKE signal for magnetization pointing along opposite directions would have opposite sign (θ and $-\theta$). The null signal is the middle point of θ and $-\theta$, and optical elements can be zeroed accordingly.

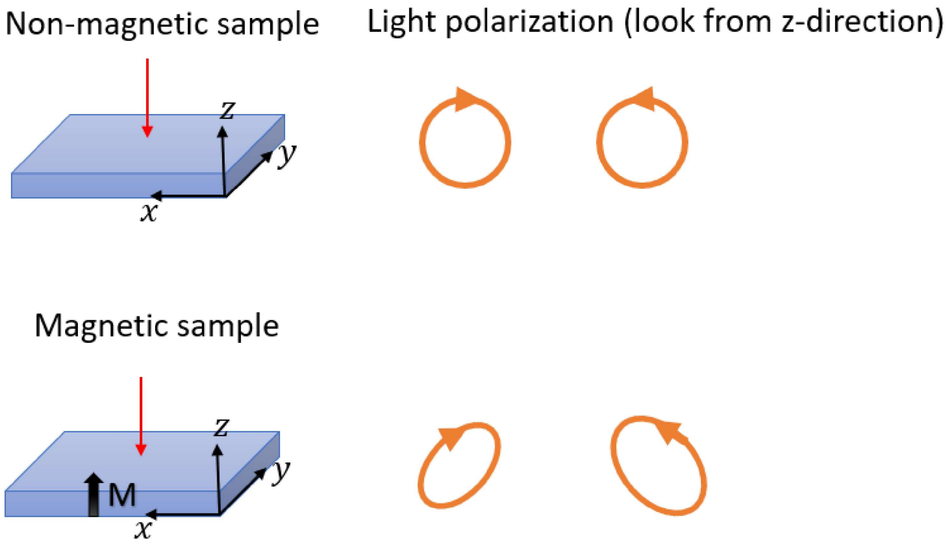

(a) When light probes a sample, if we flip both non-magnetic sample, magnetic sample and the incoming left and right circularly polarized (LCP and RCP) light, the non-magnetic sample is still the same, as is the light polarization transmitted or reflected by a non-magnetic sample. But the magnetic sample is no longer the same after flipping, and both LCP and RCP see a different sample when reflected or transmitted. Therefore, the amplitude and phase is changed by out-of-plane magnetization.

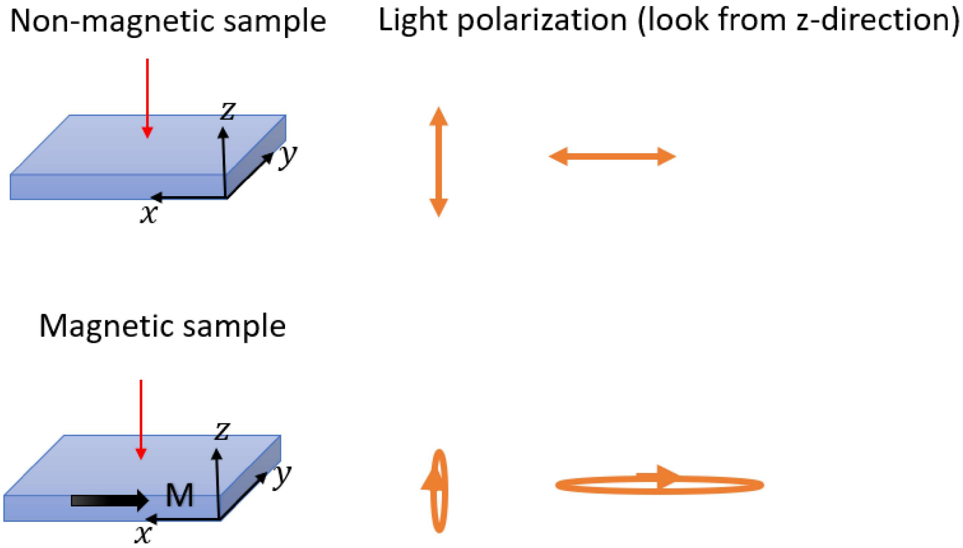

(b) With the assumption that the non-magnetic sample is isotropic, if the non-magnetic sample is rotated by 90° around z-axis, it is still the same. As is the linearly polarized light reflected back by a non-magnetic sample. But for a magnetic sample with magnetization along the x-axis, light polarized laong the x- and y-axis will see a different sample if it is rotated around the z-axis by 90°. Thus, the amplitude and phase of reflected light will be changed by in-plane magnetization or anisotropy.

Figure 5.1: The interaction between light polarization and magnetization in materials with magnetization is (a) out-of-plane (b) in-plane.

For birefringence measurement of easy plane antiferromagnetic materials with Néel vector of two degenerate domains perpendicular to each other, we can null the signal with the fact that the birefringence signal for these two domains should have opposite sign.

Sufficient signal-to-noise ratio (S/N) and spatial resolution are required to successfully image magnetic materials.

The spatial resolution of a scanning laser miscroscopy is controlled by the beam spot size. If the domain size is small compared to the beam spot size, the signal we detected is an average of all magnetic domains inside the laser spot. The lower limit of the laser spot size is determined by the diffraction limit $d = \frac{\lambda}{2N.A.}$, where N.A. is numerical aperture. For a 50 X objective lens from Mitutoyo with N.A. = 0.55, the minimal spatial resolution with 635 nm laser is 1.2 μm. If we try to directly measure antiferromagnetic thin films like CuMnAs, it will be unrealistic if the domain size is submicron scale, less than laser beam spot size [31]. But for bulk antiferromagnetic samples, it is possible that domain size is larger than laser spot size. In reference [104], the domains of NiO (111) was observed a with focused laser beam.

The signal-to-noise ratio (S/N) needs to be considered. For Co/Pt multilayer with perpendicular magnetic anisotropy, the polar Kerr rotation for 785 nm is around 3 mrad. The quadratic term with magnetization in-plane is about ten times smaller. With our setup, we measured the quadratic MOKE signal of Co at 635 nm as 0.12-i0.04 mrad. For magnetic birefringence signal of antiferromagnet, like MnF_2, $\Delta n/n$ is between $10^{-4} \sim 10^{-3}$[105]. The noise of our polarimetry system achieve 10^{-5} rad as discussed in following chapters.

5.2 Experimental Setup, Jones Matrix and Coefficients

5.2.1 Experimental setup

Laser source

The experimental setup is shown in Fig. 5.2. With a common He-Ne laser, the noise level of the signal significantly increases when laser beam is focused, an effect we attributed to high coherence of the He-Ne laser. Thus we chose a low-coherence diode laser (Schafter+Kirchhoff GmbH LCN-56CM-635-6-H10-T12-H-6) as the light source. The pulsed laser source (Mai-Tai) with an optical parametric oscillator can be used as light source with wider wavelength options, but it has higher intensity noise than the diode laser. The comparison of noise with diode laser and with pulsed laser will be discussed below.

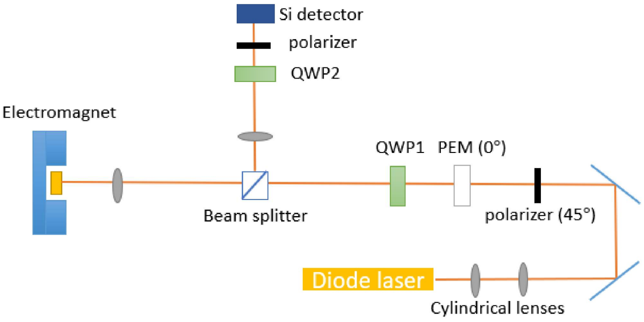

Figure 5.2: The optical setup of polarimetry to measure quadratic MOKE signal and magnetic birefringence. The polar MOKE signal can be measured with QWP1 and QWP2 removed.

Retarder

The layout of the experimental setup is shown in Fig. 5.2. The beam shape of laser comes out of laser source is elliptical, thus two cylindrical lenses (+150 mm and -50 mm) are placed after the diode laser to adjust the beam shape to make it circular. Before light passes through the photoelastic modulator (PEM), we polarized the light to 45° away from the axis of the PEM with a Glan-Taylor polarizer (GT polarizer). The extinction ratio of GT polarizer (10^5:1) is much higher than a wire-grid polarizer (800:1).

After the GT polarizer, the light polarization is modulated with a PEM. The PEM modulates light by mechanically compressing or stretching a fused silica bar with a natural resonant frequency of 50 kHz. This vibration is sustained by a quartz piezoelectric transducer attached to the end of the bar.

In a birefringent crystal, the velocities of light with polarization perpendicular and parallel to the optical axis is different due to the anisotropic refractive index. The optical beam path difference will result in a phase difference as light passes through the crystal $\Delta\delta = \frac{2\pi}{\lambda} d\Delta n$, where d is the thickness of the crystal, Δn is the birefringence, and λ is wavelength. The wave plates changes the polarization of light with a birefringent crystal specifically designed to add a specific fixed phase difference to the light. A half-wave plate (HWP) has phase retardance π and a quarter-wave plate (QWP) has phase retardance $\pi/2$. We describe the polarization of incident light by $\vec{E}e^{i(kz-wt)}$ and decompose the incident light along the optical axis $\vec{e}_1$ and perpendicular to the optical axis $\vec{e}_2$:

$$\vec{E}e^{i(kz-wt)} = (E_1\vec{e}_1 + E_2\vec{e}_2)e^{i(kz-wt)} \tag{5.1}$$

After passing through the half-wave plate, a phase retardance of $\Delta\delta = \pi$ is added to the light and the electric field component along the optical axis E_1 stays the same while the component perpendicualr to the optical

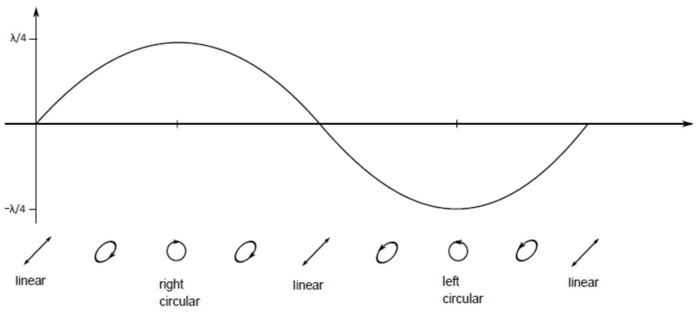

Figure 5.3: The light polarization in one period after the PEM.

axis E_2 changes sign:

$$\begin{aligned} &(E_1\vec{e}_1 + E_2\vec{e}_2e^{i\pi})e^{i(kz-wt)} \\ =&(E_1\vec{e}_1 - E_2\vec{e}_2)e^{i(kz-wt)} \end{aligned} \tag{5.2}$$

Linearly polarized light with angle θ with respect to the optical axis of the HWP will be rotated by 2θ to $-\theta$. Similarly, electric fields after the QWP are $(E_1\vec{e}_1 \pm iE_2\vec{e}_2)e^{i(kz-wt)}$, which is circularly polarized light.

In contrast to wave plates that add a fixed phase retardance, the retardance of the PEM is oscillating at frequency $f = 50$ kHz. We set the amplitude of the PEM to $\pi/2$, thus, the PEM works as a QWP when retardance is at maximum or minimum. The temporal phase retardance of the PEM and the light polarization over one period is shown in Fig. 5.3. When the incident light is polarized at 45°, the light will oscillate between left circularly polarization (LCP) and right circularly polarization (RCP).

The retardance of the PEM can be expressed as $\Delta\delta = \delta_0 \sin(2\pi ft)$, and the electrical field after PEM is $(E_1\vec{e}_1 + E_2\vec{e}_2e^{i\delta_0 \sin(2\pi ft)})e^{i(kz-wt)}$. The exponential term can be expanded with Bessel functions, where the imaginary part is at the first harmonic f and the real part is at the second harmonic $2f$. Since the MO effect can be complex, the real and imaginary change of light polarization can be resolved by measuring signals with a lock-in amplifier at f and $2f$.

With light polarization oscillating between LCP and RCP, the out-of-plane magnetization can be measured with the setup. Once a quarter wave plate (QWP) is inserted after the PEM (QWP1 in Fig. 5.2) with angle set to 45°, another $\pi/2$ retardance is added to the light. The light polarization then oscillates between vertically and horizontally polarized states. In this configuration, the measurement is sensitive to in-plane magnetization or anisotropy of the materials.

Table 5.1: Measurement configurations of polarimetry

Measurement frequency	Without QWP1 or QWP2	With QWP1 and QWP2
$1f$	θ_2	β_1
$2f$	θ_1	β_2

Sample configuration

In the polarimetry setup, the laser beam passes through the non-polarizing beam splitter twice. We used a laser line non-polarizing beam splitter (Newport 05BC16NP.4) because it is less birefringent than a broadband non-polarizing beam splitter. In front of the sample, a focal lens or objective lens was used to focus the beam on the sample.

An electromagnet was placed around the sample to apply an in-plane magnetization to change the domain structure. There are two poles surrounded by coils to confine the magnetic field inside the gap between the two poles. The upper limit of the field can be changed by adjusting the gap. The field of the electromagnet is controlled with a high power current source. Without water cooling, the applied current cannot exceed 4 A. We used a chiller to circulate cooling water in the coils. With foolings, the maximum current is 8 A.

Analyzer

To measure the change in the polarization of light produced by the sample, we used a linear polarizer or a circular polarizer to decompose the light along certain axis. We then use a silicon photodetector to measure the light intensity change as described in Fig. 5.4. The light intensity is composed of a DC part, and first harmonic and second harmonic parts. The DC signal is measured with a multimeter, and the signals at f and $2f$ are read from AF lock-in amplifier by choosing harmonics. The reference input of lock-in amplifier is connected to the sync output of the PEM controller.

Figure 5.4 from Ref. [106] shows the amplitude and phase change of light polarization in a polar MOKE measurement scheme. With a linear polarizer as the analyzer, the amplitude and phase change of light can be picked up at first and second harmonic.

Both amplitude and phase of the optical electric fields will be changed by magnetization, while we are only able to measure light intensity. Properly choosing analyzers and pick-up frequency can separate the measurement of phase and amplitude of light to gain information about the real and imaginary part of Kerr rotation or magnetic birefringence of magnetic materials. If we write the complex Kerr rotation as $\theta = \theta_1 + i\theta_2$ and complex birefringence or quadratic MOKE as $\beta = \beta_1 + i\beta_2$, the setup to measure these terms are shown in Table. 5.1. We use a wire-grid polarizer as la inear polarizer, and a polarizer combined with a QWP (QWP2 shown in Fig. 5.2) as a circular polarizer.

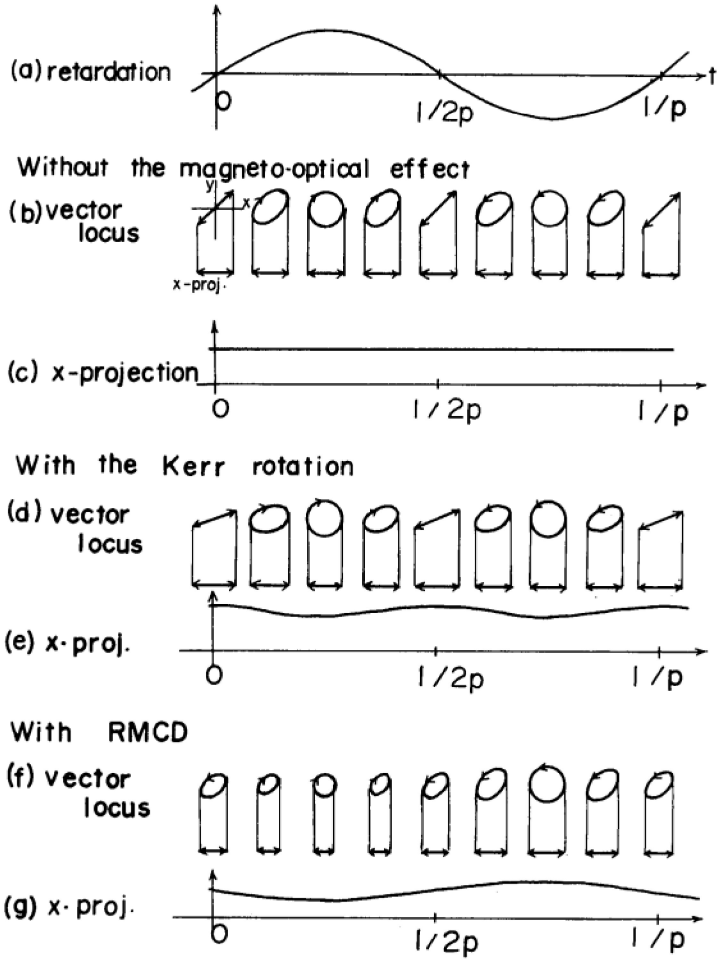

Figure 5.4: The light polarization of polar Kerr rotation measurement scheme from reference [106]. The "x-projection" is the light projected along the x-direction, which is achieved with a linear polarizer during measurement. (a) The retardance of PEM in one period with frequency p. (b)(c) The light polarization and projection on x-axis after PEM. (d)(e) The phase change of the light polarization after it is reflected back from sample. The x-projection of the polarization change is at thesecond harmonic. (f)(g) The amplitude change of the light polarization, and the projection along the x-axis shows it can be measured at first harmonic.

5.2.2 Jones Matrix Calculation of the Measurement Configuration

To better understand the optical setup and derive the relationship between the MO signal and the light intensity reading, we used a Jones matrix scheme to model how MO signals are generated and detected.

Polar MOKE measurement

As described earlier, the electrical field after the PEM is $(E_1\vec{e}_1 + E_2\vec{e}_2 e^{i\delta_0 \sin(2\pi ft)})e^{i(kz-wt)}$ where $\vec{e}_1$ is along optical axis. Since the incoming light before the PEM is polarized along 45°, $E_1 = E_2$. The Jones matrix of light polarization after passing through the PEM is a 2D vector representative of electrical field, which is

$$\begin{pmatrix} 1 \\ e^{i\delta} \end{pmatrix} = \begin{pmatrix} e^{-i\delta/2} \\ e^{i\delta/2} \end{pmatrix} \tag{5.3}$$

where E_1 and E_2 are normalized, $\delta = \delta_0 \sin(2\pi ft)$ and $\delta_0 = \pi/2$ is the phase retardance amplitude set by the PEM controller. The sample with out-of-plane magnetization is

$$\mathbf{M} = r \begin{pmatrix} 1 & -\theta \\ \theta & 1 \end{pmatrix} \tag{5.4}$$

where θ is complex polar MOKE signal. If we set the light propagation direction as the z-axis, then the electrical field reflected by the sample is

$$\begin{pmatrix} E_x \\ E_y \end{pmatrix} = r \begin{pmatrix} e^{-i\delta/2} - \theta e^{i\delta/2} \\ \theta e^{-i\delta/2} + e^{i\delta/2} \end{pmatrix} \tag{5.5}$$

If we write complex θ as $\theta_1 + i\theta_2$, the light intensity with polarization along x- and y-axis are:

$$\begin{aligned} I_x &= |E_x|^2 = |r|^2(1 + |\theta|^2 - 2\theta_1 \cos\delta - 2\theta_2 \sin\delta) \\ I_y &= |E_y|^2 = |r|^2(1 + |\theta|^2 + 2\theta_1 \cos\delta - 2\theta_2 \sin\delta) \end{aligned} \tag{5.6}$$

The $\cos\delta$ and $\sin\delta$ can be expanded with Bessel functions

$$\begin{aligned} \sin\delta &= \sin(\delta_0 \sin(2\pi ft)) = 2J_1(\delta_0)\sin(2\pi ft) + ... \\ \cos\delta &= \cos(\delta_0 \sin(2\pi ft)) = J_0(\delta_0) + 2J_2(\delta_0)\sin(4\pi ft) + ... \end{aligned} \tag{5.7}$$

When $\delta_0 = \pi/2$, the Bessel function coefficients are $J_0(\pi/2) = 0.47$, $J_1(\pi/2) = 0.57$, $J_2(\pi/2) = 0.25$. The $\sin\delta$ term can be measured at f, and $\cos\delta$ contributes to both DC part and $2f$ part. By aligning the polarizer in front of Si detector along x-or y-direction, what we measure is the same as I_x and I_y in Eq. 5.6. If the polarizer is polarized along the x direction, the DC part measured with multimeter is $I_{DC} = |r|^2$ after neglecting small terms. The signal measured by the lock-in is $I_{1f} = -4|r|^2\theta_2 J_1(\pi/2)$ and $I_{2f} = -4|r|^2\theta_1 J_2(\pi/2)$.

If we set phase retardance δ_0 to 2.405, the Bessel coefficients $J_0 = 0$, $J_1 = 0.52$ and $J_2 = 0.43$. There is no extra DC component from $\cos\delta$ and second harmonic signal is larger because $J_2(2.405)$ is almost twice $J_2(\pi/2)$.

With $\pi/2$ retardance, the coefficient between I_{1f} read from lock-in and I_{DC} read from multimeter is

$$\frac{I_{1f}}{I_{DC}} = -2\theta_2 \sin\delta \frac{1}{\sqrt{2}} = -1.61\theta_2 \sin(2\pi f t) \tag{5.8}$$

where $\sqrt{2}$ comes from conversion between rms voltage and DC voltage. Similarly, the relation between I_{2f} and I_{DC} is

$$\frac{I_{2f}}{I_{DC}} = -2\theta_1 \cos\delta \frac{1}{\sqrt{2}} = -0.71\theta_1 \sin(4\pi f t) \tag{5.9}$$

Both θ_1 and θ_2 can be resolved with polarizer is along either x-or y-axis. θ_2 can be measured without analyzer, because $2f$ terms from I_x and I_y cancel out:

$$I = I_x + I_y = 2|r|^2(1 + |\theta|^2 - 2\theta_2 \sin\delta) \tag{5.10}$$

Magnetic birefringence measurement

For samples with magnetization or anisotropy in-plane, the Jones matrix of the sample is

$$\mathbf{M} = r \begin{pmatrix} 1+\beta & 0 \\ 0 & 1-\beta \end{pmatrix} \tag{5.11}$$

where β is complex, $\beta = \beta_1 + i\beta_2$. We call β magnetic birefringence for second order magneto-optic effects generated by Néel vector of AFs, and quadratic MOKE for second order magneto-topcial effect generated by the magnetization of FMs.

After the beam passes through PEM, QWP1(45°), and reflected by the sample, we use circular polarizer (QWP2 at 45° and a polarizer at 0 or 90°) as the analyzer. The light intensity after QWP2 along x-and y-axis is

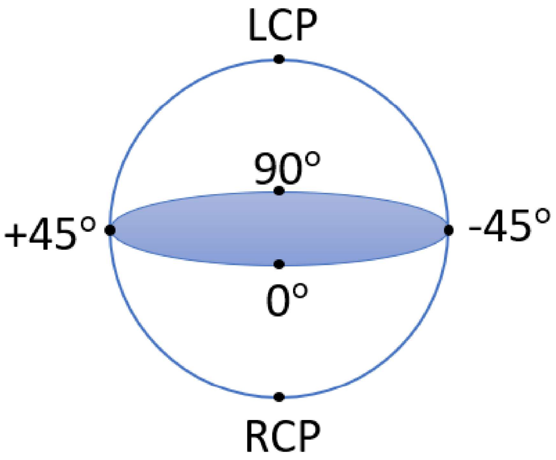

Figure 5.5: The Poincare sphere. The points on equator represent linear polarization. The north pole and south pole represent left and right circularly polarized ligh (LCP and RCP).

$$\begin{aligned} I_x =& 1 + |\beta|^2 - 2\beta_1 \sin\delta - 2\beta_2 \cos\delta \\ \approx& 1 - 2\beta_2 J_0 - 4\beta_1 J - \beta_1 \sin(2\pi f t) - 4\beta_2 J_2 \sin(4\pi f t) \\ I_y =& 1 + |\beta|^2 - 2\beta_1 \sin\delta + 2\beta_2 \cos\delta \\ \approx& 1 + 2\beta_2 J_0 - 4\beta_1 J - \beta_1 \sin(2\pi f t) + 4\beta_2 J_2 \sin(4\pi f t) \end{aligned} \tag{5.12}$$

Similarly, we can measure β_1 at $1f$ and β_2 at $2f$.

5.2.3 Poincare Sphere to Understand Polarization

The Poincare sphere is a representative of the light polarization. Points on the sphere surface represent polarization states. As shown in Fig. 5.5, points on the equator are linear polarized light, while the north pole and south pole represent circularly polarized light. If the points are not on poles or the equator, they represent elliptically polarized states.

In our polarimetry setup, the linear polarizer we used in front of the photodetector connects points on the sphere to the equator. The intensity after the linear polarizer is related to the distance connecting the point on the sphere and the equator.

For example, for elliptically polarized light on the arc between +45° and LCP, the intensity is maximized when the linear polarizer is set to +45° and minimized when the linear polarizer is set to -45°.

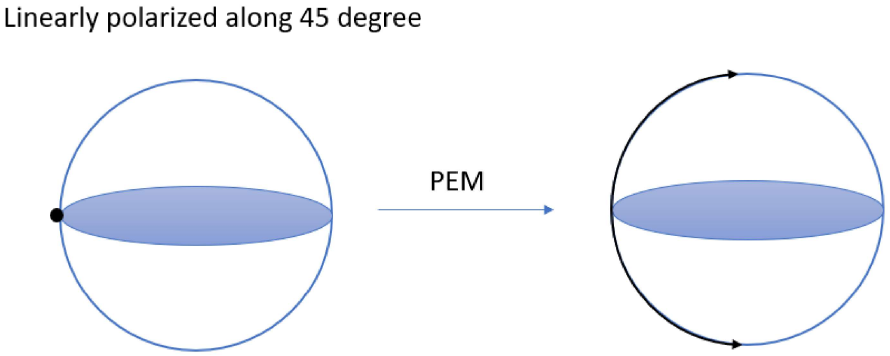

Figure 5.6: After PEM, the polarization of light is oscillating between LCP and RCP.

In the polarimetry setup, the incident light is polarized at an angle of +45°, and after the PEM, the polarization state is oscillating along an arc connecting north and south poles on the sphere as shown in Fig. 5.6.

In a polar MOKE measurement, both the amplitude and phase of the optical electric field will be changed by magnetization as in Fig. 5.7. The amplitude change means for circularly polarized light either LCP of RCP is smaller and the other one is larger. The phase change means that the polarization is away from +45° while the modulation is zero as visualized in Fig. 5.7a.

The amplitude change for linear polarization, as shown in Fig. 5.7b, means the magnitude of either light polarized at an angle of 0° of 90° is smaller while the other one is larger. The effect is linear light is rotated by some angle. Circular polarized components introduced and the light is slightly elliptical.

5.2.4 Noise and birefringence of the system

Noise characterization of polarimetry setup

As discussed above, the noise floor of the system determines the smallest signal we can observe. Thus, characterization of the noise floor is an essential procedure in evaluation a measurement setup.

The noise of the polarimetry setup was recorded by measuring 50 data points from lock-in amplifier and calculating their standard deviation. To avoid the effect of birefringence from the beam splitter, a mirror was placed at the position of the non-polarizing beam splitter that directly reflects light towards the detector.

Comparing Table 5.2 and Table 5.3, we see that the diode laser is more stable overall, and the noise level of polarimetry measurement with the diode laser as the laser source is at the 10^{-5} rad level with 300 ms time constant (5×10^{-6} rad/$\sqrt{\text{Hz}}$).

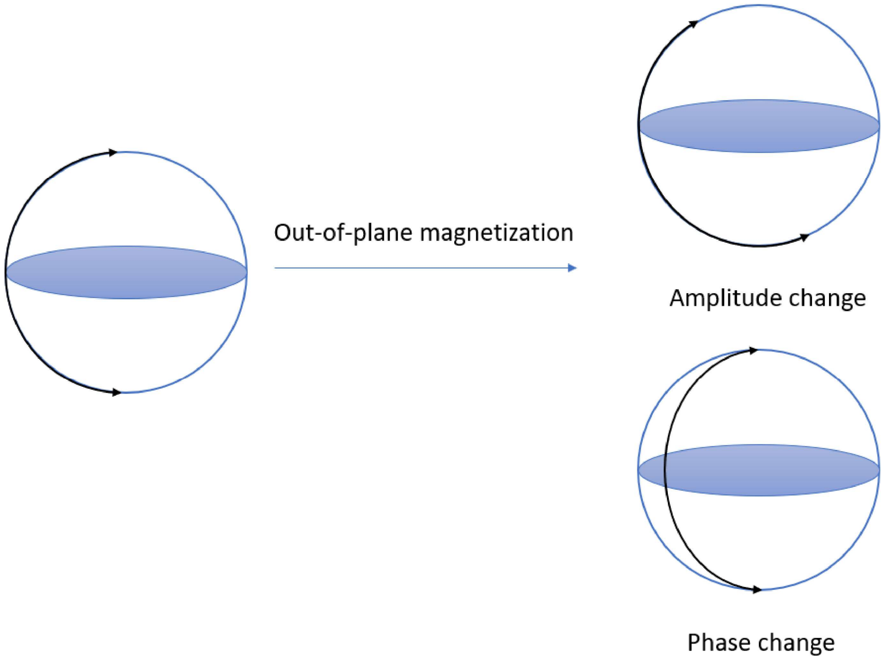

(a) The light state is modified by the out-of-plane magnetization, and the change can be decomposed into amplitude change and phase change.

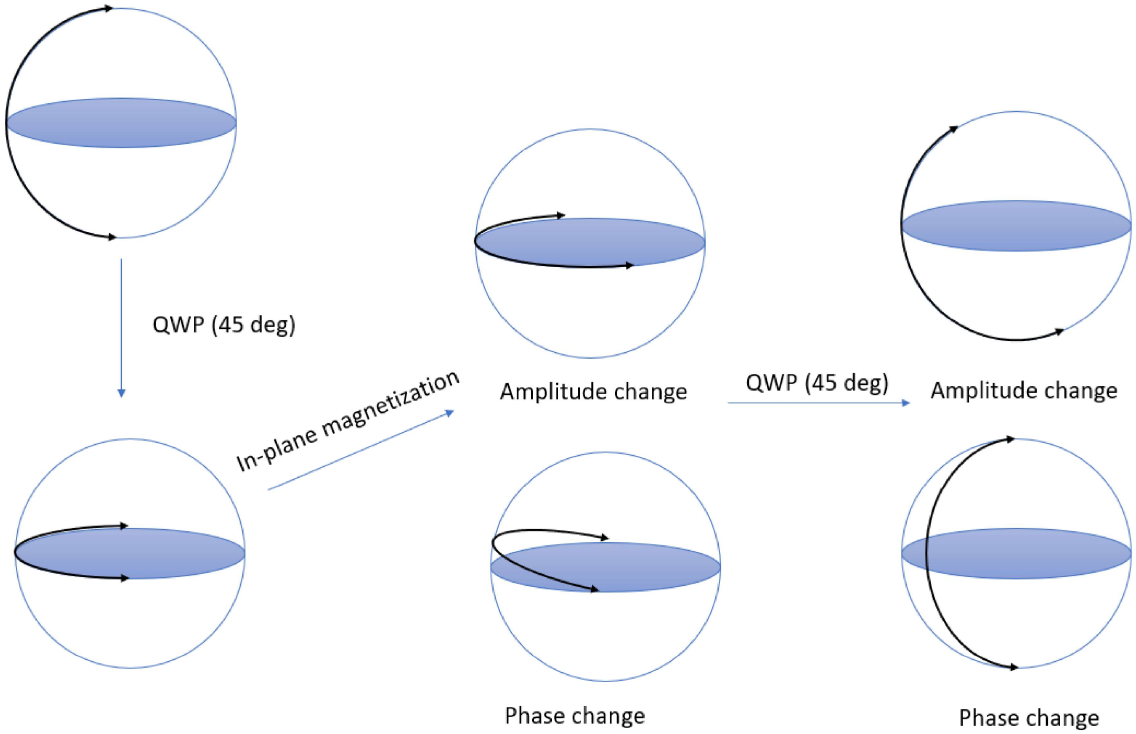

(b) To detect in-plane magnetization, the light polarized between LCP and RCP passes through QWP1, then it is oscillating between 0° and 90°. The in-plane magnetization changes phase and amplitude of the linear light. After passing through QWP2, both amplitude and phase change look similar to upper figure and can be picked up with the same way.

Figure 5.7: Poincare sphere representation of light polarization in polarimetry setup.

Setup	standard deviation of $1f$ signal (rad)	standard deviation of $2f$ signal (rad)
PEM→ mirror→ det	4×10^{-6}	4×10^{-6}
PEM→ mirror→ polarizer(0°)→ det	6×10^{-4}	3×10^{-4}
PEM → QWP(45°) → mirror → det	1×10^{-5}	3×10^{-6}
PEM → QWP(45°) → mirror → polarizer(0°) → det	2×10^{-3}	6×10^{-4}
PEM → QWP(45°) → mirror → QWP(45°) → polarizer(0°) → det	1×10^{-3}	1×10^{-4}

Table 5.2: Signal fluctuation of polarimetry with OPO as laser source with 300 ms time constant

Setup	standard deviation of $1f$ signal (rad)	standard deviation of $2f$ signal (rad)
PEM→ mirror → det	5×10^{-6}	7×10^{-6}
PEM→ mirror → polarizer(0°)→ det	6×10^{-6}	1×10^{-5}
PEM → QWP(45°) → mirror → det	5×10^{-6}	2×10^{-5}
PEM → QWP(45°) → mirror → polarizer(0°) → det	3×10^{-5}	2×10^{-5}
PEM → QWP(45°) → mirror → QWP(45°) → polarizer(0°) → det	9×10^{-6}	8×10^{-6}

Table 5.3: Signal fluctuation of polarimetry with diode laser as laser source with 300 ms time constant

Signal drift at long time scale

During the polarimetry measurement, we also noticed that the signal is slowly drifting. The drift was recorded by collecting data points of a non-magnetic sample for 50 seconds with the setup depicted Fig. 5.2. The signal fluctuation is shown in Fig. 5.8a. We do not yet understand the origin of the slow drift. One possible reason of the drift is the laser heats the optics and change the birefringence of the optics slowly.

To solve this problem, we modulated the external field by turning on and off the electromagnet with frequency 1 Hz, and use the signal difference of field-on and field-off as the value we measured. The voltage was controlled with the auxiliary output of the lock-in amplifier. By programming the aux out, we oscillate the field by turning on the voltage for 500 ms then turning off the voltage for another 500 ms. Since the 1 s interval is much maller than the time scale of the drift, we can assume the difference of on and off is relatively free from the effect of the slow drifts.

However, this field modulation method only works for AF materials, because we expect the field-induced magnetic birefringence is linear in the external field. If we treat the signal at zero field as null signal, $V_{rf}(H) = V_{rf}(H) - V_{rf}(0)$. The field modulation method cannot be used to eliminate contributions from slow drifts for ferromagnetic materials. The $V_{rf}(0)$ is not zero in FMs due to the existence of hysteresis.

Birefringence from optics

In our experimental setup (Fig. 5.2), we first used a 1" broad band non-polarizing beam splitter cube (400 nm to 700 nm). Then we realized that broadband thick beam splitter introduced large birefringence signal and affected our measurement result.

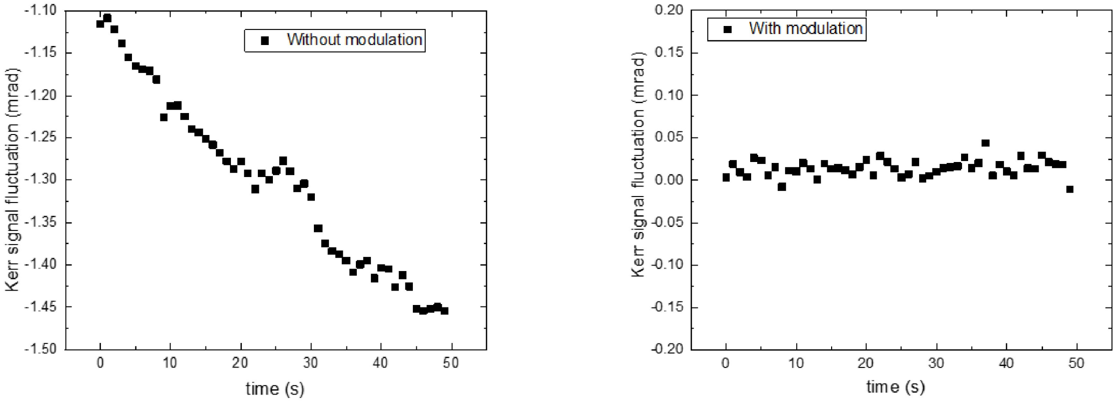

(a) TBA

(b)

Figure 5.8: (a) (b)

When we used the Kerr rotation measurement setup (PEM → BS → sample → BS → pol(0d) → detector) to measure a non-magnetic sample (Au sputtered on Si), we expect both 1f and 2f signals should be close to zero. In our observation, however, the 2f signal is small, the 1f signal is about 40% of the DC signal, which is equivalent to a 0.24 rad (14 deg) Kerr rotation angle if we apply Eq. 5.8. This deviation is too large to compensate with rotating the linear polarizer in front of the detector. In other words, for circularly polarized incident light, the beam splitter makes the light polarization elliptical.

To solve this problem, the 1” broad-band BS was replaced by a 0.5” laser line BS. With the similar Kerr rotation measurement setup (PEM → BS → sample → BS → pol(-8d) → detector), the 1f signal is only 5% of DC signal. This small deviation can be compensated by slightly rotating linear polarizer by a small angle, or by placing QWP2 in the beam path and rotating it by a small angle (elliptical component added to CP light can be removed by QWP2).

5.2.5 How to set the angle of optics

For wire-grid polarizers, the marked optical axis sometimes can be off by 1 to 2 degrees. Moreover, the mounting of PEM can make the optical axis off from absolute vertical by a small angle. Since the real signal we want to measure is in mrad scale, much smaller than the deviation of optics, properly adjusting the angle of optics can help to minimize the birefringence of the system.

We first set the angle of the GT polarizer to 45° by rotating the optical mount by looking at the scale. For polar MOKE measurement, we only need to adjust the angle of the linear polarizer in front of the detector. Without the linear analyzer, the $1f$ signal is propotional to θ_2 and the $2f$ signal should be zero. One can measure θ_2 without an analyzer. To measure θ_1, a linear polarizer is needed as an analyzer, the angle of polarizer was set to 0 or 90 degree. If the $1f$ signal read from the AF lock-in is non-zero, we can null the signal by slightly rotating the polarizer by a small angle, this step can help to eliminate deviation-induced rotation of light polarization. If extra ellipticity was added to light polarization because of birefringent optical elements, we can place QWP2 in front of linear polarizer, and set the angle parallel to the linear polarizer, then iteratively and slightly adjust the angle of the linear polarizer and QWP2. A small rotation of QWP2 can eliminate the ellipticity that comes from the system birefringence.

For birefringence measuremenst, both QWPs and the linear polarizer can be adjusted. We roughly set the QWP1 angle to 45 degree by eye, and then null the $2f$ signal by finely adjusting the QWP1 without an analyzer. According to Eq. 5.12, the $2f$ signal is zero without an analyzer $(I_x + I_y)$. The QWP2 should be placed at 45 degree or 135 degree, parallel or perpendicular to QWP1. The QWP1 changes CP to linear polarizer for detection, and the QWP2 changes linear polarizer back to CP to further analyze the signal, as shown in Poincare representations. The angle of QWP2 can be adjusted by minimizing or maximizing the DC signal. We then orient the linear polarizer to 0 degree or 90 degree. Both linear polarizer and QWP2 can be slightly adjusted to null the $1f$ signal.

5.3 Quadratic MOKE of Cobalt and YIG

Our measurement setup is sensitive to in-plane magnetization of FMs. For magnetic samples with easy-plane, we can measure its quadratic MOKE signal by rotating an external field. In this section, we report the quadratic MOKE measurement of a Co thin film and a YIG/GGG ample by rotating the external field.

The cobalt thin film was deposited with magnetron sputtering with structure Pt(2 nm)/Co(10 nm)/Sapphire. The thick cobalt deposited on top of c-plane of sapphire would have in-plane anisotropy. We used a Halbach cylinder, a magnet composed of 12 small magnets arranged to create a ~700 Oe in-plane field, to rotate the field in the sample plane. For both Co thin film and YIG, the 700 Oe field is enough to saturate the magnetization in-plane. We can get the quadratic MOKE signal comes from M_s^2 based on the geometric relationship between field and light polarization.

To get the quadratic MOKE signal with rotating magnetization, we mathematically derived the relation between magnetization and polarization with a Jones matrix calculation. The calculation process is the same as in the previous chapter, except we rotate the magnetized sample matrix with a rotation matrix by θ. The rotation matrix is:

$$R(\theta) = \begin{pmatrix} \cos(\theta) & \sin(\theta) \\ -\sin(\theta) & \cos(\theta) \end{pmatrix} \tag{5.13}$$

The rotated sample matrix is $M_{rot} = R(-\theta)MR(\theta)$ where

$$M = r \begin{pmatrix} 1+\beta & 0 \\ 0 & 1-\beta \end{pmatrix}$$

and $\beta = \beta_1 + i\beta_2$

During the measurement, QWP1 was inserted in the incident light path. For reflected light, there are four measurements we can do: no circular analyzer at 1f and 2f; and with circular analyzer at 1f and 2f.

Without the circular polarizer, the intensity of the reflected beam at DC, 1f and 2f are:

$$\begin{aligned} I_{DC} &= 1 + \beta_1^2 + \beta_2^2 \\ \frac{I_{1f}}{I_{DC}} &= -2\beta_1 \cos(2\theta) \sin\delta \frac{1}{\sqrt{2}} = -1.61\beta_1 \cos(2\theta) \sin(2\pi f t) \\ \frac{I_{2f}}{I_{DC}} &= -2\beta_1 \sin(2\theta) \cos\delta \frac{1}{\sqrt{2}} = -0.71\beta_1 \sin(2\theta) \sin(4\pi f t) \end{aligned} \tag{5.14}$$

With the circular polarizer (QWP2 at 45° and followed by a linear polarizer at 0°), the intensity of the neglected beam at DC, 1f and 2f are:

$$\begin{aligned} I_{DC} &= 1 + \beta_1^2 + \beta_2^2 \\ \frac{I_{1f}}{I_{DC}} &= -2(\beta_1 \cos(2\theta) - \beta_2 \sin(2\theta)) \sin\delta \frac{1}{\sqrt{2}} = -1.61(\beta_1 \cos(2\theta) - \beta_2 \sin(2\theta)) \sin(2\pi f t) \\ \frac{I_{2f}}{I_{DC}} &= -2(\beta_1 \sin(2\theta) - \beta_2 \cos(2\theta)) \cos\delta \frac{1}{\sqrt{2}} = -0.71(\beta_1 \sin(2\theta) - \beta_2 \cos(2\theta)) \sin(4\pi f t) \end{aligned} \tag{5.15}$$

The coefficients are calculated with phase retardance $\delta_0 = \pi/2$. From above four measurements, it is adequate to derive β_1 and β_2 from Eq. 5.15 and Eq. 5.14.

No matter if circular polarizer is used, the β_1 value can be written as is

$$\beta_1 = \frac{i_{1f}(90°) - i_{1f}(0°)}{2(1.61)} = \frac{i_{2f}(45°) - i_{2f}(135°)}{2(0.71)} \tag{5.16}$$

where lower case i represents normalized intensity I_{1f}/I_{DC} and I_{2f}/I_{DC}.

The β_2 only appears when circular polarizer is used:

$$\beta_1 = \frac{i_{1f}(135°) - i_{1f}(45°)}{2(1.61)} = \frac{i_{2f}(90°) - i_{2f}(0°)}{2(0.71)} \tag{5.17}$$

From the measurement data with Co film (Fig. 5.9), the β_1=0.12 mrad and β_2 = -0.04 mrad. For YIG,

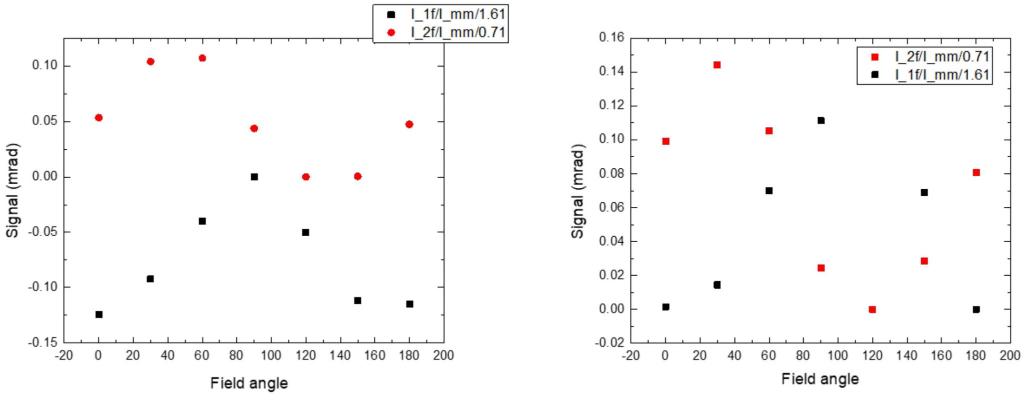

(a) (b)

Figure 5.9: The polarimetry measurement of Pt(2)/Co(10)/Sapphire with 700 Oe field rotating in the sample plane (a)without cirular polarizer and (b)with circular polarizer as analyzer. The data were picked up at both $1f$ and $2f$.

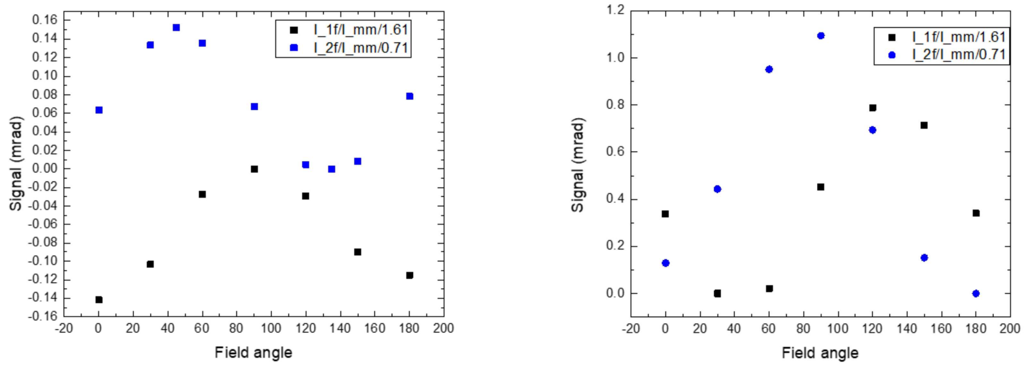

(a) (b)

Figure 5.10: The polarimetry measurement of YIG/GGG with 700 Oe field rotating in the sample plane (a)without cirular polarizer and (b)with circular polarizer as analyzer. The data were picked up at both $1f$ and $2f$.

the $\beta_1 = 0.075$, $\beta_2 = 0.5$ mrad. Because both Co and YIG have small coercivity, 700 Oe in-plane field is enough to saturate the sample.

5.4 Circular Dichroism of Sugar Solution

Sugar molecules are chiral so they are optically active to circularly polarized light. Since sugar is non-magnetic, we can name the optical rotation as circular dichroism. Sugar solution can be used to evaluate the polarimetry because: a) the transmission can give much larger signal than reflection, b) the analyzer is only sensitive to circular dichorism signal, so it's free from birefringence of optics in the setup.

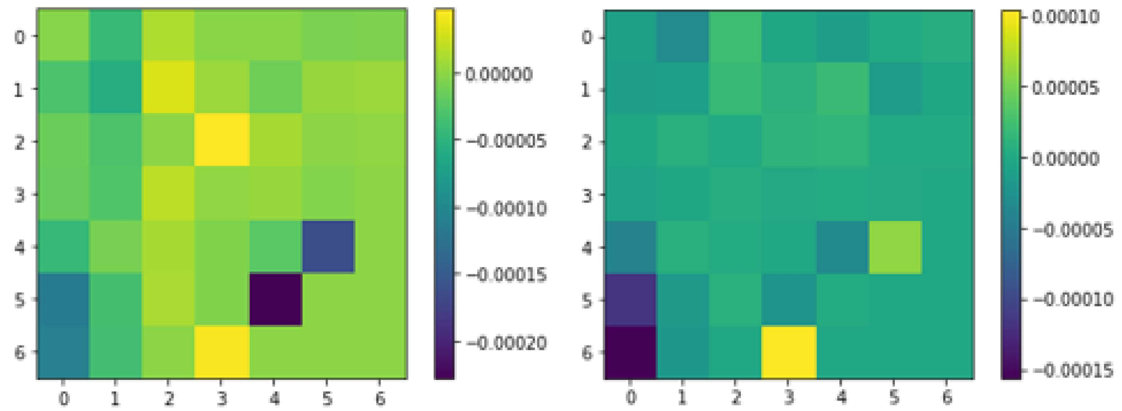

(a) (b)

Figure 5.11: The mapping of Fe_2As (001) face measured with scanning polarimetry. At each point, The external field was modulated between zero field and B field for three cycles and averaged. (a) B = 0 T, (b) B = 1 T. QWP1 was at 45 degree in the measurement and no analyzer was used. Signals are collected at first harmonic.

From optical rotation equation of sucrose[107],

$$\frac{\theta}{l_c} = \frac{A}{\lambda^2 - \lambda_0^2} \tag{5.18}$$

where l_c is optical path, λ is wavelength, $\lambda_0 = 131$ nm, $A = 2.16 \times 10^7$ deg nm^2 dm^{-1} g^{-1} mL. Because the sugar solution is transparent, the imaginary part can be neglected.

I mixed 0.45 g sugar with 5 g water (90 g/mL) and fill the cuvette with sugar solution. From Eq. 5.18, the optical rotation with 90 g/mL concentrate is 1.12 mrad/mm. The optical path of cuvette is 10 mm. So the expected rotation is 11.2 mrad.

To measure the optical rotation of sugar solution, I placed the cuvette in front of beam splitter and let the laser beam passed through. Neither QWP1 nor QWP2 is used, but linear polarizer used as analyzer. The data were collected at $2f$ with linear polarizer is at near 0 deg. We record the change of AC signal from AF lock-in with covette and without covette, and the DC signal was read from a multimeter. The signals we got for sugar solution is I_{2f} = -375 μV and I_{DC} = 69 mV with $\pi/2$ retardation. So the real part of the rotation is 7.7 mrad, close to what we expected.

5.5 Magnetic Birefringence Measurement of Antiferromagnetic Materials

Fe_2As has two degenerated magnetic domains: one with Néel vector along [100], the other one with Néel vector along [010]. When an external field is applied along [100], the domains along [100] won't be affected, but the domains along [010] would reorient and becomes [100]. We expected to do two types of measurements with our polarimetry setup: mapping of two kinds of domains at zero field; and mapping of birefringence with a field applied along one of easy axes.

We used a 100 mm focal lens to focus the laser beam on the sample because objective lens is close to electromagnet at focus and the Faraday effect cannot be neglected. The beam size is around 100 μm.

We did a magnetic field dependent measurement and mapping of Fe_2As. Fig. 5.11 shows the mapping results of Fe_2As. The Fe_2As crystal was polished along (001) face, and, during the measurement, the external field was applied in the (001) plane along [100] direction. At each point, the field was modulated between zero field and B field, where B = 0 T in Fig. 5.11a and B = 1 T in Fig. 5.11b. Because we believe the field-induced domain motion is reversible when the field is removed, modulating external field would help to remove the effect of slow drifts as described above. We did not observe obvious difference when external field is applied or not applied. The standard deviation of the signal in Fig. 5.11a is 4.7×10^{-5}, and std in Fig. 5.11b is 3.5×10^{-5}. It implies for signal smaller than 4×10^{-5}, it is less likely to be observed.

In Fig. 5.12, the field dependent β_1 of three locations in Fe_2As (001) is shown. It is clear that the at position 2 the β_1 signal is field dependent. So the major domains in position 2 is parallel to external field, while domains in position 1 and position 3 are perpendicular to external field. The domain size should comparable or even larger than laser beam size. When external field is 1 T, the β_1 signal of location 2 is 5×10^{-6} rad, about ten times smaller than standard deviation of mapping signal showed above. That can explain why we cannot observe domains in mapping plots. The large standard deviation of mapping can come from the imperfect surface of the sample.

5.6 Conclusion

In this chapter, I discussed methodology of setting up polarization modulation miscrocopy to image and measure magnetic signals. The polarimetry was studied with Poincare sphere and Jones matrix representative to understand the light polarization in the setup. The noise of the system was characterized and the birefringence from optics was lowered.

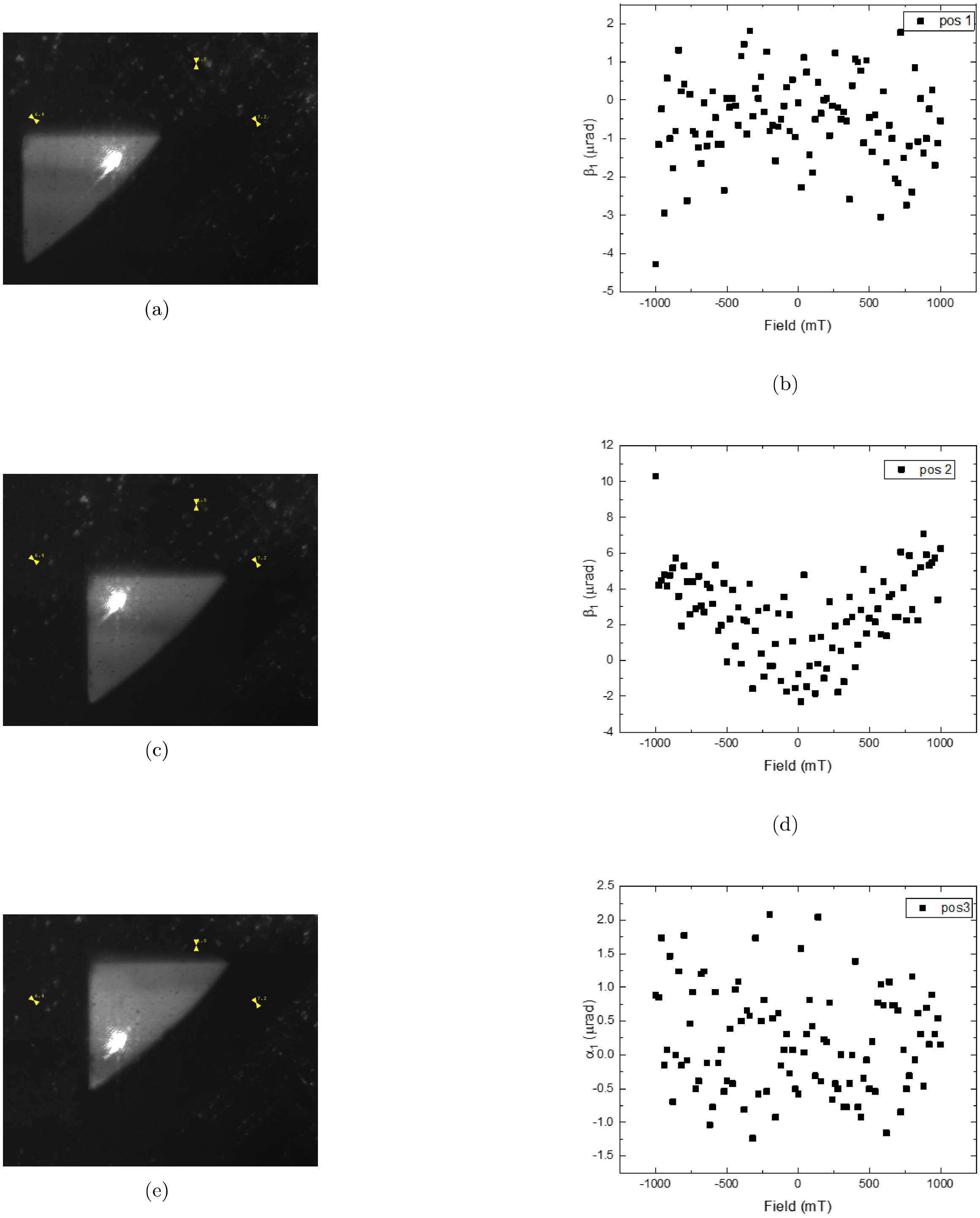

(a)

(b)

(c)

(d)

(e)

(f)

Figure 5.12: Field-dependent β_1 value of Fe_2As (001) measured with external field applied along a-axis of Fe_2As at three different locations on the sample. The external field was modulated for ten cycles for each data point.

With the setup, we can measure polar MOKE, quadratic MOKE and magnetic birefringence by properly choosing wave plates and analyzers. The circular dichroism signal of sugar solution was measured to evaluate the setup, and the signal we observed is consistent with literature. We also reported the quadratice MOKE of two typical FM samples, cobalt thin films and YIG.

We did field-dependent magnetic birefringence measurement of Fe_2As and noticed a location-dependent behavior with around 100 μm beam size. We did birefringence mapping of the easy plane of Fe_2As. Due the the limitation of large standard deviation of mapping and beam spot size of focal lens, the domain imaging of antiferromagnetic materials is difficult to achieve.

The polarization modulation can be combined with pump-probe system (TDTR-II). A PEM can be used in the probe path to modulate the polarization of the probe beam. By changing the incoming light polarization, the polar MOKE and quadratic MOKE can be measured in the time domain. If the light polarization is oscillating between horizonal and vertical, we use a polarizer at a down stream position to let the light intensity is modulated like chopper.

Chapter 6

Conclusions

Metallic antiferromagnetic materials with easy-plane structure are promising in spintronics study due to their advantages of insensitivity to magnetic field and fast dynamics. In this dissertation, I studied magneto-optical effect and magnetic anisotropy of metallic AF Fe_2As with optical techniques and magnetometers. Due to the lack of net magnetization, we focused over study on the second order of Néel vector-related birefringence with optical techniques. With the help of magnetometers, the magnetic properties of AFs are studied, including susceptibility, anisotropy and domain movement in a field.

We did extensive experimental studies of the ultrafast quadratic magneto-optic response of the metallic antiferromagnetic Fe_2As. The experimental work on ultrafast magneto-optic response is supported by 1st principles calculations, and thorough characterization of the thermophysical, magnetic, and electrical properties of these materials. We combined measurements of the transient reflectivity and transient birefringence to gain deeper understanding the changes in the dielectric constant produced by an ultrafast temperature excursion. The high-signal-to-noise of our measurements enables us to work in the regime of linear response. Counter to conventional wisdom, we found that the component of the dielectric tensor perpendicular to the vector of the sublattice magnetization is influenced by magnetization much more strongly than the component parallel to the magnetization. It shows that the thermal birefringence signal we observed is dominated by the exchange interaction, which is independent of the orientation of Néel vector or domain structure.

We studied the magnetic anisotropy and domain movement in Fe_2As with torque magnetometry. In the torque measurements, misalignment of field and field-induced magnetic moment due to anisotropy $\tau = \mathbf{m} \times \mathbf{B}$ is measured. In the measurement of the crystalline anisotropic *ac*-plane, we observed reversible domain population distribution, and the model where the induced magnetic moment $\mathbf{m}$ is calculated from the magnetic susceptibility is consistent with the measurement data. With the measurement of crystalline isotropic *ab*-plane, we calculated the magnetic anisotropy in the easy-plane. The torque data can be modeled by minimizing the total energy. The measurements of *ac*-plane and *ab*-plane brought us two scenarios to analyze the data: low field limit (magnetic energy much smaller than anisotropy) and intermediate field limit (magnetic energy comparable to anisotropy). Moreover, we derived the antiferromagnetic resonance

(AFMR) mode for easy-plane AF materials, and obtain the AFMR frequency with out-of-plane magnetic anisotropy from density-functional theory calculation.

Our torque magnetometry study suggested even 1 T field in the easy-plane of Fe_2As can significantly change the domain population. We attributed the domain population to local defects induced random strains. To further understand reversible domain movement in a magnetic field and observe field-induced magnetic birefringence, we set up a polarization modulation microscopy to do the scanning microscope of magnetic texture of materials. We modulated the polarization of laser with a photo-elastic modulator, and we can measure both complex polar MOKE and complex birefringence by choosing proper wave plates. We first measured the static complex quadratic MOKE signal of Co and YIG thin films by rotating the in-plane magnetic field angle and comparing it to Jones matrix calculations. As for the easy-plane of Fe_2As, we observed the location-dependent magnetic birefringence signal, which suggested the domain movement induced birefringence is measurable. We also measured the noise floor of the microscope to assist further study of magnetic domains.

As our measurements showed that in-plane anisotropy of Fe_2As is strongly temperature dependent and is very small at room temperature, it could be the reason that the MO coefficients depend on orientation of Néel vector (G_{11}) are small. To test this hypothesis, a further MO measurements related to G_{11} can be performed.

To explore the reason of reversal domain movement we observed in torque measurements, a field-dependent magnetic domain imaging would be helpful. As the standard deviation of the laser-based scanning microscopy is larger than the effective signal, further research can be done with X-ray based microscopy.

The dissertation work was partially supported by the NSF MRSEC under Award Number DMR-1720633.

Chapter 7

Codes in Thesis

7.1 Codes for Modelling Torque Magnetometry Data

The matlab code can be found in GitHub: `https://github.com/Yang-kexin/Torque_Fe2As`

7.2 Codes for Collecting Data from Polarimetry

The code can be found in GitHub: `https://github.com/Yang-kexin/Microscopy`

References

[1] A Fert and IA Campbell. Two-current conduction in nickel. *Physical Review Letters*, 21(16):1190, 1968.

[2] Nevill Francis Mott. The electrical conductivity of transition metals. *Proceedings of the Royal Society of London. Series A-Mathematical and Physical Sciences*, 153(880):699–717, 1936.

[3] AA Sapozhnik, M Filianina, S Yu Bodnar, A Lamirand, M-A Mawass, Y Skourski, H-J Elmers, H Zabel, M Kläui, and M Jourdan. Direct imaging of antiferromagnetic domains in mn 2 au manipulated by high magnetic fields. *Physical Review B*, 97(13):134429, 2018.

[4] M Wang, C Andrews, S Reimers, OJ Amin, P Wadley, RP Campion, SF Poole, J Felton, KW Edmonds, BL Gallagher, et al. Spin flop and crystalline anisotropic magnetoresistance in cumnas. *Physical Review B*, 101(9):094429, 2020.

[5] V Saidl, P Němec, P Wadley, V Hills, RP Campion, V Novák, KW Edmonds, F Maccherozzi, SS Dhesi, BL Gallagher, et al. Optical determination of the néel vector in a cumnas thin-film antiferromagnet. *Nature Photonics*, 11(2):91, 2017.

[6] S Yu Bodnar, L Šmejkal, I Turek, T Jungwirth, O Gomonay, J Sinova, AA Sapozhnik, H-J Elmers, M Kläui, and M Jourdan. Writing and reading antiferromagnetic mn 2 au by néel spin-orbit torques and large anisotropic magnetoresistance. *Nature Communications*, 9(1):348, 2018.

[7] Yang Cheng, Sisheng Yu, Menglin Zhu, Jinwoo Hwang, and Fengyuan Yang. Electrical switching of tristate antiferromagnetic néel order in α- fe 2 o 3 epitaxial films. *Physical Review Letters*, 124(2):027202, 2020.

[8] Felix Schreiber, Lorenzo Baldrati, Christin Schmitt, Rafael Ramos, Eiji Saitoh, Romain Lebrun, and Mathias Kläui. Concurrent magneto-optical imaging and magneto-transport readout of electrical switching of insulating antiferromagnetic thin films. *arXiv preprint arXiv:2004.13374*, 2020.

[9] Markus Meinert, Dominik Graulich, and Tristan Matalla-Wagner. Electrical switching of antiferromagnetic mn 2 au and the role of thermal activation. *Physical Review Applied*, 9(6):064040, 2018.

[10] BK Tanner. Antiferromagnetic domains. *Contemporary Physics*, 20(2):187–210, 1979.

[11] Stephen M Wu, Wei Zhang, KC Amit, Pavel Borisov, John E Pearson, J Samuel Jiang, David Lederman, Axel Hoffmann, and Anand Bhattacharya. Antiferromagnetic spin seebeck effect. *Physical review letters*, 116(9):097204, 2016.

[12] W Zhang, K Nadeem, H Xiao, R Yang, B Xu, H Yang, and XG Qiu. Spin-flop transition and magnetic phase diagram in caco 2 as 2 revealed by torque measurements. *Physical Review B*, 92(14):144416, 2015.

[13] IS Jacobs. Spin-flopping in mnf 2 by high magnetic fields. *Journal of Applied Physics*, 32(3):S61–S62, 1961.

[14] IS Jacobs and PE Lawrence. Metamagnetic phase transitions and hysteresis in fecl 2. *Physical Review*, 164(2):866, 1967.

[15] FLA Machado, PRT Ribeiro, J Holanda, RL Rodríguez-Suárez, A Azevedo, and SM Rezende. Spin-flop transition in the easy-plane antiferromagnet nickel oxide. *Physical Review B*, 95(10):104418, 2017.

[16] Gyung-Min Choi, André Schleife, and David G Cahill. Optical-helicity-driven magnetization dynamics in metallic ferromagnets. *Nature communications*, 8(1):1–7, 2017.

[17] RM Bozorth. Directional ferromagnetic properties of metals. *Journal of Applied Physics*, 8(9):575–588, 1937.

[18] J-Y Bigot, M Vomir, LHF Andrade, and E Beaurepaire. Ultrafast magnetization dynamics in ferromagnetic cobalt: The role of the anisotropy. *Chemical physics*, 318(1-2):137–146, 2005.

[19] Takuya Satoh, Sung-Jin Cho, Ryugo Iida, Tsutomu Shimura, Kazuo Kuroda, Hiroaki Ueda, Yutaka Ueda, BA Ivanov, Franco Nori, and Manfred Fiebig. Spin oscillations in antiferromagnetic nio triggered by circularly polarized light. *Physical review letters*, 105(7):077402, 2010.

[20] AV Kimel, A Kirilyuk, PA Usachev, RV Pisarev, AM Balbashov, and Th Rasing. Ultrafast non-thermal control of magnetization by instantaneous photomagnetic pulses. *Nature*, 435(7042):655–657, 2005.

[21] E Beaurepaire, J-C Merle, A Daunois, and J-Y Bigot. Ultrafast spin dynamics in ferromagnetic nickel. *Physical review letters*, 76(22):4250, 1996.

[22] Johannes Kimling, Judith Kimling, RB Wilson, Birgit Hebler, Manfred Albrecht, and David G Cahill. Ultrafast demagnetization of fept: Cu thin films and the role of magnetic heat capacity. *Physical Review B*, 90(22):224408, 2014.

[23] Johannes Kimling, Gyung-Min Choi, Jack T Brangham, Tristan Matalla-Wagner, Torsten Huebner, Timo Kuschel, Fengyuan Yang, and David G Cahill. Picosecond spin seebeck effect. *Physical review letters*, 118(5):057201, 2017.

[24] Gyung-Min Choi, Byoung-Chul Min, Kyung-Jin Lee, and David G Cahill. Spin current generated by thermally driven ultrafast demagnetization. *Nature communications*, 5(1):1–8, 2014.

[25] Stephen M Wu, John E Pearson, and Anand Bhattacharya. Paramagnetic spin seebeck effect. *Physical review letters*, 114(18):186602, 2015.

[26] Yasuhiro Niimi and YoshiChika Otani. Reciprocal spin hall effects in conductors with strong spin–orbit coupling: a review. *Reports on progress in physics*, 78(12):124501, 2015.

[27] Joseph Sklenar, Wei Zhang, Matthias B Jungfleisch, Wanjun Jiang, Hilal Saglam, John E Pearson, John B Ketterson, and Axel Hoffmann. Spin hall effects in metallic antiferromagnets–perspectives for future spin-orbitronics. *AIP Advances*, 6(5):055603, 2016.

[28] Wei Zhang, Matthias B Jungfleisch, Wanjun Jiang, John E Pearson, Axel Hoffmann, Frank Freimuth, and Yuriy Mokrousov. Spin hall effects in metallic antiferromagnets. *Physical review letters*, 113(19):196602, 2014.

[29] X Marti, I Fina, C Frontera, Jian Liu, P Wadley, Qing He, RJ Paull, JD Clarkson, J Kudrnovskỳ, I Turek, et al. Room-temperature antiferromagnetic memory resistor. *Nature materials*, 13(4):367–374, 2014.

[30] M Wang, C Andrews, S Reimers, OJ Amin, P Wadley, RP Campion, SF Poole, J Felton, KW Edmonds, BL Gallagher, et al. Spin flop and crystalline anisotropic magnetoresistance in cumnas. *Physical Review B*, 101(9):094429, 2020.

[31] MJ Grzybowski, P Wadley, KW Edmonds, R Beardsley, V Hills, RP Campion, BL Gallagher, Jasbinder S Chauhan, V Novak, T Jungwirth, et al. Imaging current-induced switching of antiferromagnetic domains in cumnas. *Physical review letters*, 118(5):057701, 2017.

[32] Anke Sander, Maik Christl, Cheng-Tien Chiang, Marin Alexe, and Wolf Widdra. Domain imaging on multiferroic bifeo3 (001) by linear and circular dichroism in threshold photoemission. *Journal of Applied Physics*, 118(22):224102, 2015.

[33] David G Cahill. Analysis of heat flow in layered structures for time-domain thermoreflectance. *Review of scientific instruments*, 75(12):5119–5122, 2004.

[34] David G Cahill. Analysis of heat flow in layered structures for time-domain thermoreflectance. *Review of scientific instruments*, 75(12):5119–5122, 2004.

[35] Quantum Design. *Physical Property Measurement System Heat Capacity Option User's Manual*, 2004.

[36] Leo J van der Pauw. A method of measuring the resistivity and hall coefficient on lamellae of arbitrary shape. *Philips technical review*, 20:220–224, 1958.

[37] Diego A Zocco, Duygu Y Tütün, James J Hamlin, Jason R Jeffries, Samuel T Weir, Yogesh K Vohra, and M Brian Maple. High pressure transport studies of the lifeas analogs cufete2 and fe2as. *Superconductor Science and Technology*, 25(8):084018, 2012.

[38] Rembert Duine. Spintronics: An alternating alternative. *Nature materials*, 10(5):344, 2011.

[39] Jairo Sinova and Igor Žutić. New moves of the spintronics tango. *Nature materials*, 11(5):368, 2012.

[40] Takuya Satoh, Bas B Van Aken, Nguyen Phuc Duong, Thomas Lottermoser, and Manfred Fiebig. Ultrafast spin and lattice dynamics in antiferromagnetic cr2o3. *Physical Review B*, 75(15):155406, 2007.

[41] Christian Tzschaschel, Kensuke Otani, Ryugo Iida, Tsutomu Shimura, Hiroaki Ueda, Stefan Günther, Manfred Fiebig, and Takuya Satoh. Ultrafast optical excitation of coherent magnons in antiferromagnetic nio. *Physical Review B*, 95(17):174407, 2017.

[42] Aleksandra Mikhailovna Kalashnikova, Alexey Vol'demarovich Kimel, and Roman Vasilievich Pisarev. Ultrafast opto-magnetism. *Physics-Uspekhi*, 58(10):969, 2015.

[43] S Visnovsky, V Prosser, R Krishnan, V Parizek, K Nitsch, and L Svobodova. Magnetooptical polar kerr effect in ferrimagnetic garnets and spinels. *IEEE Transactions on Magnetics*, 17(6):3205–3210, 1981.

[44] Jeffrey McCord. Progress in magnetic domain observation by advanced magneto-optical microscopy. *Journal of Physics D: Applied Physics*, 48(33):333001, 2015.

[45] DS Schmool, N Keller, M Guyot, R Krishnan, and M Tessier. Magnetic and magneto-optic properties of orthoferrite thin films grown by pulsed-laser deposition. *Journal of applied physics*, 86(10):5712–5717, 1999.

[46] Tomoya Higo, Huiyuan Man, Daniel B Gopman, Liang Wu, Takashi Koretsune, Olaf MJ van't Erve, Yury P Kabanov, Dylan Rees, Yufan Li, Michi-To Suzuki, et al. Large magneto-optical kerr effect and imaging of magnetic octupole domains in an antiferromagnetic metal. *Nature photonics*, 12(2):73, 2018.

[47] P Nemec, M Fiebig, T Kampfrath, and AV Kimel. Antiferromagnetic opto-spintronics: Part of a collection of reviews on antiferromagnetic spintronics. *arXiv preprint arXiv:1705.10600*, 2017.

[48] WB Muir and JO Ström-Olsen. Electrical resistance of single-crystal single-domain chromium from 77 to 325 k. *Physical Review B*, 4(3):988, 1971.

[49] Tomas Jungwirth, X Marti, P Wadley, and J Wunderlich. Antiferromagnetic spintronics. *Nature nanotechnology*, 11(3):231, 2016.

[50] SS Dhesi, G van der Laan, and E Dudzik. Determining element-specific magnetocrystalline anisotropies using x-ray magnetic linear dichroism. *Applied physics letters*, 80(9):1613–1615, 2002.

[51] J Ferré and GA Gehring. Linear optical birefringence of magnetic crystals. *Reports on Progress in Physics*, 47(5):513, 1984.

[52] Hisao Katsuraki and Norio Achiwa. The magnetic structure of fe2as. *Journal of the Physical Society of Japan*, 21(11):2238–2243, 1966.

[53] H Le Gall, Tran Khanh Vien, and B Desormiere. Theory of the elastic and inelastic scattering of light by magnetic crystals. ii. second-order processes. *physica status solidi (b)*, 47(2):591–606, 1971.

[54] N Tesařová, P Němec, E Rozkotová, J Šubrt, H Reichlová, D Butkovičová, F Trojánek, P Malý, V Novák, and T Jungwirth. Direct measurement of the three-dimensional magnetization vector trajectory in gamnas by a magneto-optical pump-and-probe method. *Applied Physics Letters*, 100(10):102403, 2012.

[55] Kwangu Kang, Yee Kan Koh, Catalin Chiritescu, Xuan Zheng, and David G Cahill. Two-tint pump-probe measurements using a femtosecond laser oscillator and sharp-edged optical filters. *Review of Scientific Instruments*, 79(11):114901, 2008.

[56] SV Frolov and ZV Vardeny. Double-modulation electro-optic sampling for pump-and-probe ultrafast correlation measurements. *Review of Scientific Instruments*, 69(3):1257–1260, 1998.

[57] V Baltz, Aurelien Manchon, M Tsoi, T Moriyama, T Ono, and Y Tserkovnyak. Antiferromagnetic spintronics. *Reviews of Modern Physics*, 90(1):015005, 2018.

[58] Takuya Satoh, Sung-Jin Cho, Ryugo Iida, Tsutomu Shimura, Kazuo Kuroda, Hiroaki Ueda, Yutaka Ueda, BA Ivanov, Franco Nori, and Manfred Fiebig. Spin oscillations in antiferromagnetic nio triggered by circularly polarized light. *Physical review letters*, 105(7):077402, 2010.

[59] Masayuki Hagiwara, Koichi Katsumata, H Yamaguchi, M Tokunaga, I Yamada, M Gross, and P Goy. A complete frequency-field chart for the antiferromagnetic resonance in mnf 2. *International journal of infrared and millimeter waves*, 20(4):617–622, 1999.

[60] Georg Kresse and Jürgen Furthmüller. Efficient iterative schemes for ab initio total-energy calculations using a plane-wave basis set. *Phys. Rev. B*, 54(16):11169, 1996.

[61] G. Kresse and D. Joubert. From ultrasoft pseudopotentials to the projector augmented-wave method. *Phys. Rev. B*, 59:1758–1775, 1999.

[62] M. Gajdoš, K. Hummer, G. Kresse, J. Furthmüller, and F. Bechstedt. Linear optical properties in the projector-augmented wave methodology. *Phys. Rev. B*, 73:045112, 2006.

[63] John P. Perdew, Kieron Burke, and Matthias Ernzerhof. Generalized gradient approximation made simple. *Phys. Rev. Lett.*, 77:3865, 1996.

[64] P. E. Blöchl. Projector augmented-wave method. *Phys. Rev. B*, 50:17953, 1994.

[65] Hendrik J. Monkhorst and James D. Pack. Special points for brillouin-zone integrations. *Phys. Rev. B*, 13:5188, 1976.

[66] A Togo and I Tanaka. First principles phonon calculations in materials science. *Scr. Mater.*, 108:1, 2015.

[67] LM Corliss, JM Hastings, W Kunnmann, RJ Begum, MF Collins, E Gurewitz, and David Mukamel. Magnetic phase diagram and critical behavior of fe 2 as. *Physical Review B*, 25(1):245, 1982.

[68] Norio Achiwa, Shuya Yano, Motoyoshi Yuzuri, and Hideo Takaki. Magnetic anisotropy in the c-plane of fe2as. *Journal of the Physical Society of Japan*, 22(1):156–157, 1967.

[69] N. David Mermin. Thermal properties of the inhomogeneous electron gas. *Phys. Rev.*, 137:A1441–A1443, 1965.

[70] Jun Liu, Gyung-Min Choi, and David G Cahill. Measurement of the anisotropic thermal conductivity of molybdenum disulfide by the time-resolved magneto-optic kerr effect. *Journal of Applied Physics*, 116(23):233107, 2014.

[71] Judith Kimling, André Philippi-Kobs, Jonathan Jacobsohn, Hans Peter Oepen, and David G Cahill. Thermal conductance of interfaces with amorphous sio 2 measured by time-resolved magneto-optic kerr-effect thermometry. *Physical Review B*, 95(18):184305, 2017.

[72] Viktor Valentinovich Eremenko, NF Kharchenko, Yu G Litvinenko, and VM Naumenko. *Magneto-optics and spectroscopy of antiferromagnets*. Springer Science & Business Media, 2012.

[73] W Jauch. Structural origin of magnetic birefringence in rutile-type antiferromagnets. *Physical Review B*, 44(13):6864, 1991.

[74] S Borovik-Romanov, NM Kreines, AA Pankov, and MA Talalayev. Magnetic birefringence of light in antiferromagnetic transition-metal fluorides. *JETP*, 37(5):890, 1973.

[75] PA Markovin, RV Pisarev, GA Smolensky, and PP Syrnikov. Observation of isotropic magnetic contribution to the refractive index of abf3-type cubic crystals. *Solid State Communications*, 19(3):185–188, 1976.

[76] NB Weber, C Bethke, and FU Hillebrecht. Imaging of antiferromagnetic domains at the nio (1 0 0) surface by linear dichroism in near uv photoemission microscopy. *Journal of magnetism and magnetic materials*, 226:1573–1576, 2001.

[77] IR Jahn and H Dachs. Change of the optical birefringence associated with the antiferromagnetic ordering of mnf2, fef2, cof2, and nif2. *Solid State Communications*, 9(18):1617–1620, 1971.

[78] JH Liang, X Xiao, JX Li, BC Zhu, J Zhu, H Bao, L Zhou, and YZ Wu. Quantitative study of the quadratic magneto-optical kerr effects in fe films. *Optics express*, 23(9):11357–11366, 2015.

[79] Jana Hamrlová, Dominik Legut, Martin Veis, Jaromír Pištora, and Jaroslav Hamrle. Principal spectra describing magnetooptic permittivity tensor in cubic crystals. *Journal of Magnetism and Magnetic Materials*, 420:143–151, 2016.

[80] RV Pisarev, IG Sinii, NN Kolpakova, and Yu M Yakovlev. Magnetic birefringence of light in iron garnets. *Sov. Phys. JETP*, 33:1175, 1971.

[81] IR Jahn. Linear magnetic birefringence in the antiferromagnetic iron group difluorides. *physica status solidi (b)*, 57(2):681–692, 1973.

[82] Yuxin Wang, Ji Yong Park, Yee Kan Koh, and David G Cahill. Thermoreflectance of metal transducers for time-domain thermoreflectance. *Journal of Applied Physics*, 108(4):043507, 2010.

[83] RB Wilson, Brent A Apgar, Lane W Martin, and David G Cahill. Thermoreflectance of metal transducers for optical pump-probe studies of thermal properties. *Optics express*, 20(27):28829–28838, 2012.

[84] Kamil Olejník, Tom Seifert, Zdeněk Kašpar, Vít Novák, Peter Wadley, Richard P Campion, Manuel Baumgartner, Pietro Gambardella, Petr Němec, Joerg Wunderlich, et al. Terahertz electrical writing speed in an antiferromagnetic memory. *Science advances*, 4(3):eaar3566, 2018.

[85] Markus Meinert, Dominik Graulich, and Tristan Matalla-Wagner. Electrical switching of antiferromagnetic mn 2 au and the role of thermal activation. *Physical Review Applied*, 9(6):064040, 2018.

[86] Hans Jürgen Richter. Recent advances in the recording physics of thin-film media. *Journal of Physics D: Applied Physics*, 32(21):R147, 1999.

[87] Janusz J Nowak, Ray P Robertazzi, Jonathan Z Sun, Guohan Hu, Jeong-Heon Park, JungHyuk Lee, Anthony J Annunziata, Gen P Lauer, Raman Kothandaraman, Eugene J O'Sullivan, et al. Dependence of voltage and size on write error rates in spin-transfer torque magnetic random-access memory. *IEEE Magnetics Letters*, 7:1–4, 2016.

[88] AV Khvalkovskiy, D Apalkov, S Watts, R Chepulskii, RS Beach, A Ong, X Tang, A Driskill-Smith, WH Butler, PB Visscher, et al. Basic principles of stt-mram cell operation in memory arrays. *Journal of Physics D: Applied Physics*, 46(7):074001, 2013.

[89] Mirta Herak, Marko Miljak, Guy Dhalenne, and Alexandre Revcolevschi. Easy plane anisotropy in bi2cuo4. *Journal of Physics: Condensed Matter*, 22(2):026006, 2009.

[90] John MD Coey. *Magnetism and magnetic materials.* Cambridge university press, 2010.

[91] U Gäfvert, L Lundgren, B Westerstrandh, and O Beckman. Crystalline anisotropy energy of uniaxial antiferromagnets evaluated from low field torque data. *Journal of Physics and Chemistry of Solids*, 38(12):1333–1339, 1977.

[92] JC Burgiel and MWP Strandberg. Temperature dependence of the antiferromagnetic anisotropy in mnf2. *Journal of Physics and Chemistry of Solids*, 26(5):877–881, 1965.

[93] P Pincus. Temperature dependence of anisotropy energy in antiferromagnets. *Physical Review*, 113(3):769, 1959.

[94] Hisao Katsuraki and Kazuo Suzuki. Magnetic structure of fe2as. *Journal of Applied Physics*, 36(3):1094–1095, 1965.

[95] David M Ceperley and Berni J Alder. Ground state of the electron gas by a stochastic method. *Physical review letters*, 45(7):566, 1980.

[96] D Hobbs, G Kresse, and J Hafner. Fully unconstrained noncollinear magnetism within the projector augmented-wave method. *Physical Review B*, 62(17):11556, 2000.

[97] A Schrön, Claudia Rödl, and Friedhelm Bechstedt. Crystalline and magnetic anisotropy of the 3 d-transition metal monoxides mno, feo, coo, and nio. *Physical Review B*, 86(11):115134, 2012.

[98] Charles Kittel, Paul McEuen, and Paul McEuen. *Introduction to solid state physics*, volume 8. Wiley New York, 1996.

[99] F Keffer and Ch Kittel. Theory of antiferromagnetic resonance. *Physical Review*, 85(2):329, 1952.

[100] Peter Wadley, Sonka Reimers, Michal J Grzybowski, Carl Andrews, Mu Wang, Jasbinder S Chauhan, Bryan L Gallagher, Richard P Campion, Kevin W Edmonds, Sarnjeet S Dhesi, et al. Current polarity-dependent manipulation of antiferromagnetic domains. *Nature nanotechnology*, 13(5):362–365, 2018.

[101] Tristan Matalla-Wagner, M-F Rath, Dominik Graulich, J-M Schmalhorst, Günter Reiss, and Markus Meinert. Electrical néel-order switching in magnetron-sputtered cu mn as thin films. *Physical Review Applied*, 12(6):064003, 2019.

[102] S Yu Bodnar, Libor Šmejkal, I Turek, T Jungwirth, Olena Gomonay, Jairo Sinova, AA Sapozhnik, H-J Elmers, Mathias Kläui, and Martin Jourdan. Writing and reading antiferromagnetic mn 2 au by néel spin-orbit torques and large anisotropic magnetoresistance. *Nature communications*, 9(1):1–7, 2018.

[103] Yves Acremann, JP Strachan, V Chembrolu, SD Andrews, T Tyliszczak, JA Katine, MJ Carey, BM Clemens, HC Siegmann, and J Stöhr. Time-resolved imaging of spin transfer switching: Beyond the macrospin concept. *Physical review letters*, 96(21):217202, 2006.

[104] Isaiah Gray, Takahiro Moriyama, Nikhil Sivadas, Gregory M Stiehl, John T Heron, Ryan Need, Brian J Kirby, David H Low, Katja C Nowack, Darrell G Schlom, et al. Spin seebeck imaging of spin-torque switching in antiferromagnetic pt/nio heterostructures. *Physical Review X*, 9(4):041016, 2019.

[105] S Borovik-Romanov, NM Kreines, AA Pankov, and MA Talalayev. Magnetic birefringence of light in antiferromagnetic transition-metal fluorides. *JETP*, 37(5):890, 1973.

[106] Katsuaki Sato. Measurement of magneto-optical kerr effect using piezo-birefringent modulator. *Japanese Journal of Applied Physics*, 20(12):2403, 1981.

[107] RN Compton, SM Mahurin, and Richard N Zare. Demonstration of optical rotatory dispersion of sucrose. *Journal of chemical education*, 76(9):1234, 1999.